**University of South Carolina**
# Scholar Commons

Theses and Dissertations

Summer 2020

# Protein Co-Assembly and Its Application in Enzyme Engineering

Libo Zhang

Follow this and additional works at: https://scholarcommons.sc.edu/etd

Part of the Chemistry Commons

www.manaraa.com

PROTEIN CO-ASSEMBLY AND ITS APPLICATION IN ENZYME ENGINEERING

by

Libo Zhang

Bachelor of Science
Henan Normal University, 2007

Master of Science
Jilin University, 2009

Submitted in Partial Fulfillment of the Requirements

For the Degree of Doctor of Philosophy in

Chemistry

College of Arts and Sciences

University of South Carolina

2020

Accepted by:

Qian Wang, Major Professor

Thomas M. Makris, Committee Member

Maksymilian Chruszcz, Committee Member

Guiren Wang, Committee Member

Cheryl L. Addy, Vice Provost and Dean of the Graduate School

ii

# DEDICATION

To my beloved wife Lilian and family

## ACKNOWLEDGEMENTS

First and foremost, I would like to thank my advisor and mentor, Prof. Qian Wang, for giving me the opportunity to work on the multidisciplinary and highly dynamic research projects during my Ph.D. study in his lab. I am grateful for Dr. Wang's tremendous guidance, encouragement, patience as well as the flexibility that he gave me in the last five years, which help me grow as a scientist in the best way. Dr. Wang' enthusiasm and energetics in research & life are very inspiring to me.

I would also like to thank Prof. Tom Makris, who was the 'interviewer' of my Ph.D. application and my committee chair. I had free access to Makris lab/group meeting/their equipment. I thought I was a part-time student of Makris lab. I was fortunate to be able to learn about biochemistry and spectroscopy from Dr. Makris and his group members. I would also like to thank Prof. Guiren Wang, who is such a nice, amiable and approachable professor. Though the microfluidics part of my work was difficult, Dr. Wang's support and teaching made it a 'stress-free' journey for me. The working experience in Prof. Guiren Lab will be invaluable for my professional development. I would also like to thank Prof. Maksymilian Chruszcz, another 'super-nice' member of my committee, for his time and help on my Ph.D. program.

Finally, I would like to thank my lab family Dr. Sheng Feng, Dr. Yuan Lin, Dr. Gift, Dr. Yok, Dr. Lin Lv, Yanmei Xu, Amanda, Foam, Todd, Selina, Jingyu Fan, Dumei Ma, Yihua Ren, Nannie, Yunee and others, who always made the lab feel like a second home. Thank you for your friendship and all the help you have given me.

iv

ABSTRACT

Enzymes, as highly efficient biocatalysts, have been researched extensively in both academia and industry because of their distinct advantages including high substrate specificity, high regio- and stereoselectivity, environmentally benign process, etc. Though enzyme catalysis has been scaled up for commercial processes in the pharmaceutical, food and beverage and detergent industries, technical barriers associated with enzyme implementation persist, i.e., low catalytic efficiency at non-natural environment, exhausting product separations, high cost of certain enzymes, etc. Moreover, currently most industrial enzymes are used in single-step reactions; however, multistep and multienzyme catalysis with optimal efficiency could greatly expand its potential for synthetic applications to achieve complex chemical transformations. In this dissertation, we use a polymer protein co-assembly strategy to construct core-shell nanoparticles to study multistep and multienzyme involved catalysis. An electrokinetics (EK) based microfluidic method has been explored to improve the polymer-protein(s) co-assembly and fabricate homogenous polymer-enzyme hybrid nanoparticles. A group of small molecules have been characterized as efficient P450 OleT$_{SA}$ enzyme activators providing novel strategies to enhance enzyme activity in situ. Finally, a surfactant assisted enzyme involved microemulsion formation via interfacial assembly has been studied.

TABLE OF CONTENTS

LIST OF TABLES

# LIST OF SCHEMES

INTRODUCTION

Multienzyme based complex chemical transformations are common in biological processes ranging from protein synthesis to cellular metabolism. In nature, microorganisms have evolved features to maximize the catalytic efficiency of multienzyme based transformations by spatial organization, co-localization and microcompartmentation, through which proximity of multiple components of enzyme complex, mass transportation in the multistep catalysis can be sufficiently improved. Inspired by those biological systems, different strategies have been explored to improve multienzyme based catalysis including DNA scaffolds, protein scaffolds, polymeric particles assemblies, metal-organic frameworks, hydrogel encapsulation and cross-liked enzyme aggregates. While structurally and mechanistically diverse, the ultimate goal of these multiple enzyme assemblies is to accelerate reaction velocity and increase reaction efficiency. In this dissertation, protein(s) co-assembly strategies including protein-polymer co-assembly, protein-surfactant interfacial assembly have been explored to construct protein complexes in order to increase the enzymes' activity.

In Chapter 1, poly(4-vinylpyridine) polymer-arylamine *N*-oxygenase core shell nanoparticles (P4VP-CmlI) have been generated through co-assembly and studied to explore their potential use in a bio-catalytic platform. P4VP-CmlI shows excellent activity on two arylamine substrates, *p*-aminophenol (*p*AP) and *p*-aminobenzoic acid (*p*ABA), using turnover methods that employed a surrogate redox system or a peroxide shunt. Products at different oxygenation stages can be generated with different substrates. In

1

comparison to the free enzyme, P4VP-CmlI hybrids have a significantly enhanced catalytic efficiency when using pyridine nucleotide (NADH) and appropriately poised redox mediators. The enhanced catalytic efficiency of the P4VP-CmlI assemblies is attributed to a more efficient electron delivery.

In Chapter 2, we report an artificial enzyme cascade composed of glucose oxidase (GOx) and OleT$_{SA}$ from *Staphylococcus aureus* for efficient terminal alkene production. By adjusting the ratio of GOx to OleT$_{SA}$, the GOx-based tandem catalysis shows significantly improved product yield compared to the H$_2$O$_2$ injection method. The co-assembly of the GOx/OleT$_{SA}$ enzymes with a polymer, forming polymer-multienzymes nanoparticles, displays improved activity compared to the free enzyme. This two-fold strategy provides a simple and efficient system to transform a naturally abundant feedstock to industrially important chemicals. We attribute the enhanced effect of the co-assemblies origins from presence of large amount of OleT$_{SA}$ as H$_2$O$_2$ target on the nanoparticles surface as well as the closed proximity of the two enzymes after co-assembly.

In Chapter 3, we explore an electrokinetics (EK) based microfluidic reactor with fast mixing to assemble functional proteins with polymers in an ethanol/water co-solvent system. The resultant NPs show significantly improved size distribution by comparison with the ones prepared using conventional bulk method, while the NPs size can be tuned by adjusting the mass ratio of polymer to protein. The functionalities of the assembled proteins are sustained upon the EK based microfluidic mixing, indicating the application potential of our method in the controlled assembly of different functional proteins. This work sheds light on the application of this EK-based microfluidic method for polymer enzyme(s) co-assembly.

2

In Chapter 4, we report the use of a class of small molecules to enhance $OleT_{SA}$ enzymatic activity *in situ*. Up to 6-fold enhanced activity has been obtained with small molecules synthesized in house. The small molecules and enzyme substrates co-locate at the enzyme active site simultaneously. We propose the origins of the enhancement are from the enzyme oxidation step and an $H_2O_2$ toxicity inhibiting effect.

In Chapter 5, we use cytochrome P450 $OleT_{SA}$ as a model to study the interaction of surfactant and enzyme and its utilization for interfacial assembly. Both negative and positive surfactants can interact with $OleT_{SA}$ and facilitate emulsion formation via interfacial assembly. In particular, sodium dodecyl sulfate (SDS), a negative surfactant, has been identified as the optimal one to interact with $OleT_{SA,}$ which can form stable emulsions via the interfacial assembly. Biphasic enzymatic reactions have been conducted with fatty acids as substrates dissolved in hexane while the enzymes ($GOx/OleT_{SA}$) located at the interface of organic/aqueous layer. With this system, the terminal alkene products can be enriched in organic layer during the catalysis, and the overall turnover rate is comparable to that in conversional single-phase reactions.

Overall, we demonstrate that protein(s) co-assembly could be a viable approach to manipulate and improve the multistep and multienzyme based catalysis via different mechanisms. In Chapter 6, we provide some perspectives on future works to further understand the co-assembly process as well as how the process effects on enzyme catalysis, which will be beneficial to expand such strategies in enzyme engineering.

# CHAPTER 1

# ENHANCED ARYLAMINE N-OXYGENASE ACTIVITY OF POLYMER-ENZYME

# ASSEMBLIES BY FACILITATING ELECTRON-TRANSFERRING EFFICIENCY

## 1.1 INTRODUCTION

Nitro- and nitrosoaromatic compounds[1,2] are two important classes of chemicals which have been widely used as pharmaceuticals, pesticides, dyes, explosives and building blocks for synthesis and materials development.[3–7] Although various synthetic methods have been developed over the decades,[1,2,8] safety concerns, a lack of regioselectivity, and the resulting instability of the nitroso-compounds under the harsh preparatory conditions required often limit their preparation. As with other transformations, bio-catalytic platforms that can be carried out under mild reaction conditions have attracted significant attention for synthetic applications for these compounds.[9–11]

Arylamine *N*-oxygenases catalyze the six-electron oxidation of aryl-amines to aryl-nitro compounds *via* hydroxylamine and nitroso intermediates,[12–16] providing a novel tool for stepwise Ar-NO and Ar-NO$_2$ synthesis. Among these newly-characterized enzymes, CmlI is a representative arylamine *N*-oxygenase that utilizes a dinuclear-iron cofactor to catalyze the formation of the bioactive nitro-group of the antibiotic chloramphenicol (CAM) via oxidation of the arylamine precursor (NH$_2$-CAM).[16] The mechanism and structure of CmlI reveal that the enzyme catalyzes *N*-oxygenation through successive reactions with an atypical (relative to other dinuclear oxygenases) and highly stable peroxo-diferric intermediate that is generated from reaction of the reduced diferrous protein with dioxygen.[17–19] Interestingly, in addition to the final nitro-containing compound, nitroso- products can also accumulate in the enzymatic reaction with native substrate, NH$_2$-CAM.[17] Thus, CmlI may be a promising biocatalyst for leveraging Ar-NO$_2$ and/or Ar-NO synthesis if the oxygenation process can be controlled.

The use of N-oxygenases such as CmlI for synthetic applications is restricted by low catalytic efficiency. A native redox partner system that generates the diferrous form that subsequently reacts with $O_2$ has yet to be identified. It has been reported that the activity of CmlI, and AurF, a closely related ortholog involved in aureothin biosynthesis, can be reconstituted using a surrogate redox system comprised of reduced pyridine nucleotide (NADH) and the redox-mediator phenazine methosulfate (PMS) (**Scheme 1.1**).[16,20] However, the uncoupled consumption of reducing equivalents likely resulting in the generation of damaging reactive oxygen species that may limit activity. An alternative method is to use $H_2O_2$ to bypass the need for reducing equivalents altogether and generate the reactive peroxo species directly (Scheme 1.1). This approach has been used to initiate turnover in various dinuclear-iron enzymes (e.g. AurF, soluble methane monoxygenase (sMMO) and toluene 4-monooxygenase (T4Mo))[21–24] and variable levels of enzyme activity have been reported. For example, recent studies that have explored the shunt pathway in CmlI have shown that the addition of $H_2O_2$ to the diferric enzyme does not readily form the reactive peroxo-adduct that reacts with substrates.[18]
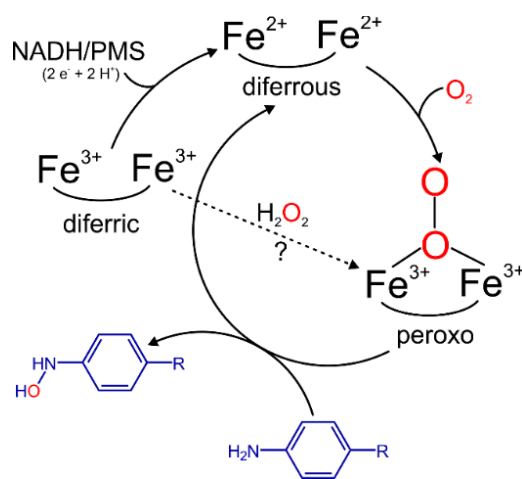


**Scheme 1.1** Illustration of the reconstitution of CmlI activity using NADH/PMS and dioxygen or via a peroxide shunt method. to generate a diferric-peroxide intermediate that reacts with arylamine substrates.

Polymer/enzyme hybrids have served as an alternative method for enzyme engineering. Upon polymer conjugation, many enzymes can exhibit improved stability, pH or temperature tolerance and catalytic efficiency with different mechanisms imparted by specific polymer structures.[25–30] The construction and characterization of pyridine-grafted polymer-protein core shell nanoparticles (PPCS-NPs) has been systematically discussed in previous studies by our laboratory.[31–36] The synthesis of PPCS-NPs is primarily entropically-driven, while the resultant nanoparticles are stabilized by synergistic interactions between polymers and proteins. The finely-balanced microenvironment can help to preserve enzyme conformation and function.[36] With a robust one-step co-assembly protocol, the proteins bound on the surface of the PPCS-NPs was greater than 90% in comparison to the initial amount of the protein used. The PPCS-NPs were found typically stable in solution for about 1−2 weeks at room temperature and 4 weeks at 4 °C. During the process, no protein leaching has been observed.[36] A broad range of functional proteins and protein cages have been co-assembled with specific polymers to form PPCS-NPs.[36–38] Moreover, the pyridine-containing polymers can exhibit a high electron affinity and favorable electron-donation properties from the pyridine unit.[39–41] Collectively, these studies indicate that P4VP polymer assembly may be leveraged with CmlI to improve its performance as a biocatalyst. In the present study, we have generated P4VP-CmlI core-shell nanoparticles through a co-assembly process and tested their catalytic activity with the arylamine substrates $p$AP and $p$ABA. Interestingly, we observed that different intermediate products accumulate with these two substrates. We found that P4VP-CmlI showed significantly higher activity on both substrates than the free enzyme that is attributed to a more efficient electron delivery process due to proximity of enzymes and

7

cofactors. This step is rate-limiting in many classes of oxidoreductases[42,43] and the identification of native redox-delivery systems can be a major bottleneck if the genes that encode them are located outside of the immediate genetic locus. As a result, the P4VP-enzyme assembly method may be generally applicable to leverage oxidoreductase catalysis in a variety of synthetic platforms.

## 1.2 EXPERIMENTAL SECTION

### 1.2.1 MATERIALS

P4VP (Mw 60000), *p*-aminophenol (*p*AP, >99.0%), flavin mononucleotide (FMN) and riboflavin were purchased from Sigma-Aldrich. Phenazine methosulfate (PMS, >98.0%), *p*-aminobenzoate (*p*ABA, >99.0%) were purchased from TCI America. NADH sodium salt was purchased from EMD Millipore. Unless otherwise noted, all chemicals and solvents used were of analytical grade and were used as received from commercial sources. Water (18.2 MΩ) was obtained from Milli-Q system (Millipore). Unless otherwise noted, all buffers are 50 mM 3-(*N*-morpholino) propane sulfonic acid (MOPS), pH 7.4.

### 1.2.2 HETEROLOGOUS EXPRESSION AND PURIFICATION OF CMLI

The *Streptomyces venezuelae* CmlI gene, cloned into the pVP91A expression vector and characterized in previous studies,[19] was used for protein expression. This vector contains an eight-histidine tag at the *N*-terminus to facilitate purification. Expression of CmlI was performed in *E. coli* BL21 (DE3) in LB medium in the presence of 100 µg/mL ampicillin. Cells were grown to an OD ~ 1.0 and induced with 150 µM IPTG and 50 µM FeCl$_3$ at which point the temperature was lowered to 20 °C, and grown for an additional 15 h. Cells were harvested by centrifugation for purification or stored at -80 °C for further use. The protein was purified using nickel-nitriloacetic acid (Ni-NTA) affinity

8

chromatography as described previously [19] and was subsequently dialyzed against 50 mM MOPS pH 7.4 buffer and stored at -80 °C until further use. Enzyme purity was assessed by SDS-PAGE and the iron-to-enzyme ratio was verified by the ferrozine assay (Figure S1).[44]

### 1.2.3 SYNTHESIS OF P4VP-CMLI ASSEMBLIES

A solution of P4VP in ethanol (7.5 mg·mL$^{-1}$, 0.1 mL) was slowly added to a solution containing CmlI in 50 mM MOPS pH 7.4 (1.2 mg·mL$^{-1}$, 0.9 mL) with stirring. After addition, the mixture was stirred for an additional 30 minutes. To study the influence of FMN reduction by NADH, the P4VP-CmlI assemblies were prepared with a similar procedure but with diluted P4VP (0.75 mg·mL$^{-1}$, 0.1 mL) and CmlI enzyme (0.12 mg·mL$^{-1}$, 0.9 mL) in 50 mM MOPS pH 7.4. All the assembled samples were freshly prepared in the characterization and activity test.

### 1.2.4 CHARACTERIZATION OF P4VP-CMLI ASSEMBLIES

The P4VP-CmlI sample (20 μL) was centrifuged to collect the nanoparticles and resuspended with the same volume of water, dropped onto a stub and dried in the hood, then coated with a thin layer of gold film using a Denton Vacuum Desk II. The sputtered samples were fixed onto the sample holder and placed in the vacuum chamber of the microscope under low vacuum (1025 Torr) for imaging by the in-lens detector of Zeiss Ultraplus Thermal Field Emission Scanning Electron Microscope (FESEM). For TEM analysis, the sample was diluted 100 times by water, 20 μL diluted sample was dropped onto 300-mesh carbon-coated copper grids and dried. The grids were then stained with 20 μL of uranyl acetate (2% w/v) for 5 minutes and observed with a Hitachi H-8000 electron microscope. The size distribution of P4VP-CmlI assemblies were measured with dynamic light scattering (DLS, Zetasizer Nano ZS, Malvern Instruments). The mean value for the

9

size based on the intensity, and the polydispersity index (PDI), a dimensionless width parameter based on the cumulant analysis, were detected.

## 1.2.5 ACTIVITY ASSAY OF P4VP-CMLI ASSEMBLIES AND FREE CMLI

The activity assay of both P4VP-CmlI and free CmlI were performed in a reaction volume of 100 μL. The final reaction mixture contained CmlI (20 μM), the substrate *p*AP or *p*ABA (1 mM), PMS or FMN or riboflavin (12.5 - 125 μM), NADH (1 - 10 mM), and 7% ethanol in MOPS buffer. Reactions were performed at room temperature (23 – 25°C) and were initiated by the addition of the substrate to the reaction mixture. The specific activity was calculated during the first 10 minutes. The PMS, FMN and riboflavin reagent were freshly prepared and kept dark until use. NADH and PMS or FMN or riboflavin were added immediately before each reaction to minimize any possible side reactions in the presence of oxygen.[45] P4VP-CmlI and CmlI reactions were prepared and tested side-by-side for an accurate comparison of activity. Reactions with *p*AP were measured by monitoring *p*NOP product formation at an absorbance of 405 nm with a Molecular Device SPECTRAMax plus 384 with a microplate reader using 0.33 cm path length. The activity assay with *p*ABA was performed with the same procedure, the products were quantified by HPLC as described below. The assays were performed in at least triplicates and the averages were reported.

## 1.2.6 PEROXIDE-SHUNT ASSAY

Peroxide-shunt experiments were performed by the addition of $H_2O_2$ to the solution containing enzyme and substrate. Final reactions contained CmlI (20 μM), *p*AP or *p*ABA (1 mM), 1.5% $H_2O_2$ (v/v) and 7% ethanol in MOPS buffer (50 mM, pH 7.4). The activity was quantified by HPLC as described below. To compare the stability and activity of the

assembled enzyme complexes with that of the free enzyme, a pre-treatment time course study was done with pre-incubation of P4VP-CmlI and free enzymes with 1.5% $H_2O_2$ (v/v) for 0 h, 1 h, 2 h, 5 h, then the activity test was followed.

### 1.2.7 HPLC AND MS ANALYSIS

Reactions with *p*AP were quenched by trifluoroacetic acid (final concentration 2.5% v/v). Reactions with *p*ABA were quenched using acetic acid (final concentration 1% v/v).  After quenching, samples were centrifuged at 15,000 g at 4 °C for 15 minutes and the supernatant was collected. Due to the sensitivity of aryl-nitroso compounds towards NADH,[46] both P4VP-CmlI and free CmlI catalyzed reactions were analyzed by HPLC immediately after quenching and centrifugation. The products were identified and quantified using an Agilent 1100 series HPLC equipped with a ZORBAX SB-C18 column. HPLC parameters were as follows: 25°C; solvent A, 1% acetic acid in water; solvent B, methanol; gradient, 10% B for 2 min; then, from 10% B to 100% B over 18 min; flow rate, 0.5 ml/min. Detection of the products resulting from *p*AP metabolism was by UV absorbance at 305 nm. Those from *p*ABA reactions were monitored at 268 nm. Quantification was done based on the peak area of the corresponding compounds. LC-MS with electrospray ionization was carried out in Mass Spectrometry Center, USC to identify the *p*HABA.

### 1.2.8 FMN REDUCTION RATE TEST

MOPS 50 mM pH 7.4 buffer was degassed for 30 minutes before used for P4VP-CmlI assembly, solutions of FMN (500 μM), NADH (50 mM) and P4VP- and free CmlI enzyme were degassed separately for 10 minutes and diluted with MOPS buffer before

11

each test. UV−Vis absorption studies were performed using an Agilent 8453 UV−Vis spectrometer (1 mm path length) with exposure of air.

## 1.3 RESULT AND DISCUSSION

### 1.3.1 P4VP-CMLI SYNTHESIS AND CHARACTERIZATION

CmlI enzyme was purified by using nickel-nitriloacetic acid (Ni-NTA) affinity chromatography. The purity was identified by SDS-PAGE as shown in **Figure 1.1**. A robust one-step protocol for PPCS-NPs generation through co-assembly was described in detail in previous studies.[36] In our work, P4VP polymer was dissolved in ethanol then added into CmlI enzyme solution drop wisely with vigorous stirring. After addition, the mixture was stirred for an additional 30 minutes for equilibration (**Figure 1.2a**). Because of the high loading capacity of the PPCS-NPs,[36] the equilibrated P4VP-CmlI sample was used in the following morphology test and enzymatic assay without a further purification. Based on the FESEM results (**Figure 1.2b**), P4VP-CmlI core shell nanoparticles were successfully generated. Dynamic light scattering (DLS) analysis revealed the average diameter of P4VP-CmlI nanoparticles was around 200 nm and the polydispersity index (PDI) was 0.107, showing considerable homogeneous nanoparticles formed (**Figure 1.2c**). This was consistent with our previous research results.[32,36]
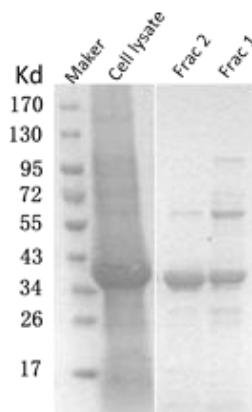


**Figure 1.1** SDS-PAGE of purified CmlI enzyme

12
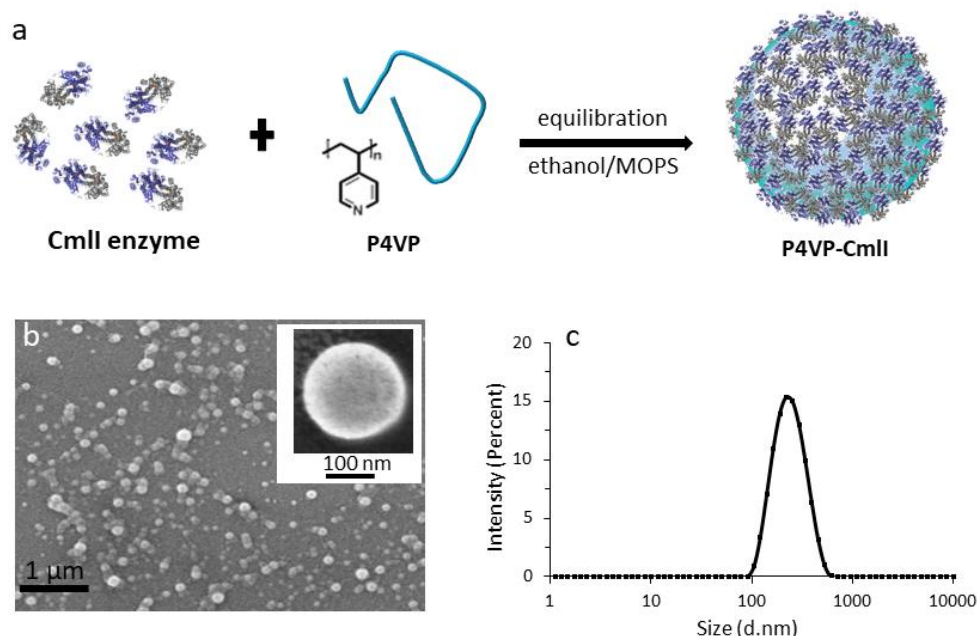
**Figure 1.2** (a) Schematic representation of the preparation of P4VP-CmlI in MOPS buffer at pH 7.4. (b) FESEM image of P4VP-CmlI nanoparticles. Inset shows an enlarged image of a single particle. (c) Size distribution of P4VP-CmlI nanoparticles based on DLS measurement.

### 1.3.2 CATALYTIC ACTIVITY OF P4VP-CMLI

Aside from reactions with the native $NH_2$-CAM substrate, there is only limited data that defines the substrate scope for CmlI reactions.[16] From transient kinetics measurements, it is known that the peroxo-CmlI adduct exhibits enhanced rates of decay in the presence of arylamine compounds with different *para* substituents including *p*AP, *p*ABA and L-*p*APA (L-para-aminophenylalanine).[19] However, the products for these reactions have not been identified. In this study, *p*AP and *p*ABA were chosen as model substrates for characterizing P4VP-CmlI activity. Based on reported catalytic mechanism of CmlI, the nitro substituted compounds (*p*NP and *p*NBA) should be produced as the final six-electron oxidized products, while the analogous hydroxylamino- (*p*HAP and *p*HABA) and nitroso- compounds (*p*NOP and *p*NOBA) may be observed as intermediate products (**Scheme 1.2**).[17] It was reported that an arylamine N-oxygenase isolated from *Pseudomonas syringae*

*pv. Phaseolicola* (PsAAO), a closely-related ortholog of AurF and CmlI, could tolerate and even showed higher activity in the presence of methanol.[21] We found that CmlI had similar characteristics, i.e. the presence of 7% ethanol increased the enzyme activity by approximately 50%. To get consistent results, the P4VP-CmlI NPs were tested in the 7% ethanol/MOPS co-solvent without further purification after the co-assembly.
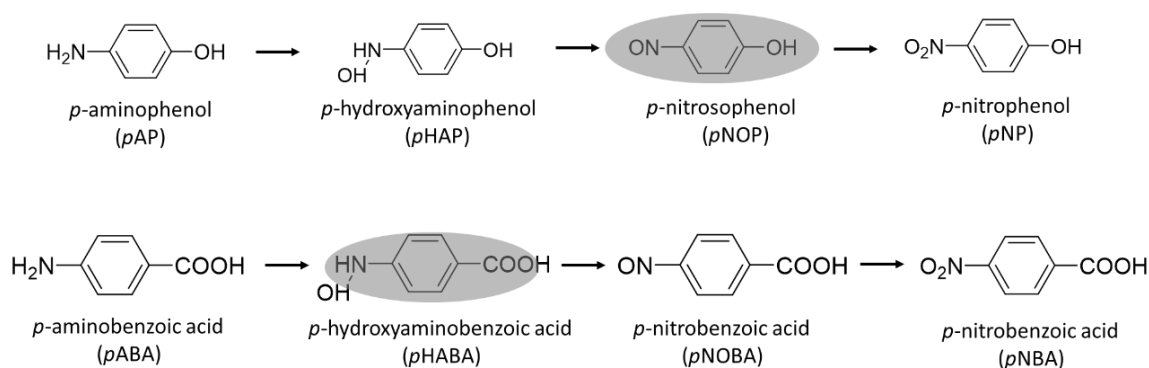


**Scheme 1.2** Schematic representation of CmlI catalyzed reaction with *p*AP and *p*ABA as substrate *The shaded products were observed with NADH/PMS method.

The activity of P4VP-CmlI was reconstituted using a redox system composed of NADH and the mediator phenazine methosulfate (PMS). The activity was alternatively assessed with a peroxide-shunt method using 1.5% $H_2O_2$ (v/v). The *p*AP and *p*ABA substrates tested here have opposing electrophilicities at the *para* substitution (Scheme 1.2). Very interestingly, while both *p*AP and *p*ABA could serve as substrates for CmlI, we observed that for *p*AP, the intermediate product *p*NOP, rather than the fully oxidized *p*NP, was accumulated for both the P4VP-CmlI and free CmlI catalyzed reactions using either method (**Figure 1.3a**, **Figure 1.4**). In contrast, when *p*ABA was used as a substrate, the intermediate product *p*HABA was accumulated with the NADH/PMS method (**Figure 1.3d-f**) and *p*NBA was accumulated with the peroxide-shunt method (**Figure 1.5**). For comparison, the ortholog AurF was reported to have activity with *p*ABA, but no activity was observed with *p*AP.[22] AurF also exhibits product distributions that depend on the

turnover methods utilized which was attributed to different reaction steps being rate-limiting.[22]

The mechanisms why intermediate products can escape from the enzyme active center have not been well understood so far. In this study, smaller size of the two unnatural substrates by comparing their native counterpart could partially explain why they can easily release from the enzyme active center without fully oxidation. The proposed mechanism for CmlI catalysis invokes an amphiphilic nature of the peroxo-CmlI oxidant, which could perform electrophilic (for amine or hydroxylamino) or nucleophilic oxidations (for nitroso) of substrates respectively.[17] Each of these would be expected to be highly sensitive to the nature of the *para* substituent. As a result, product distributions and activity would be expected to alter as we observed here.
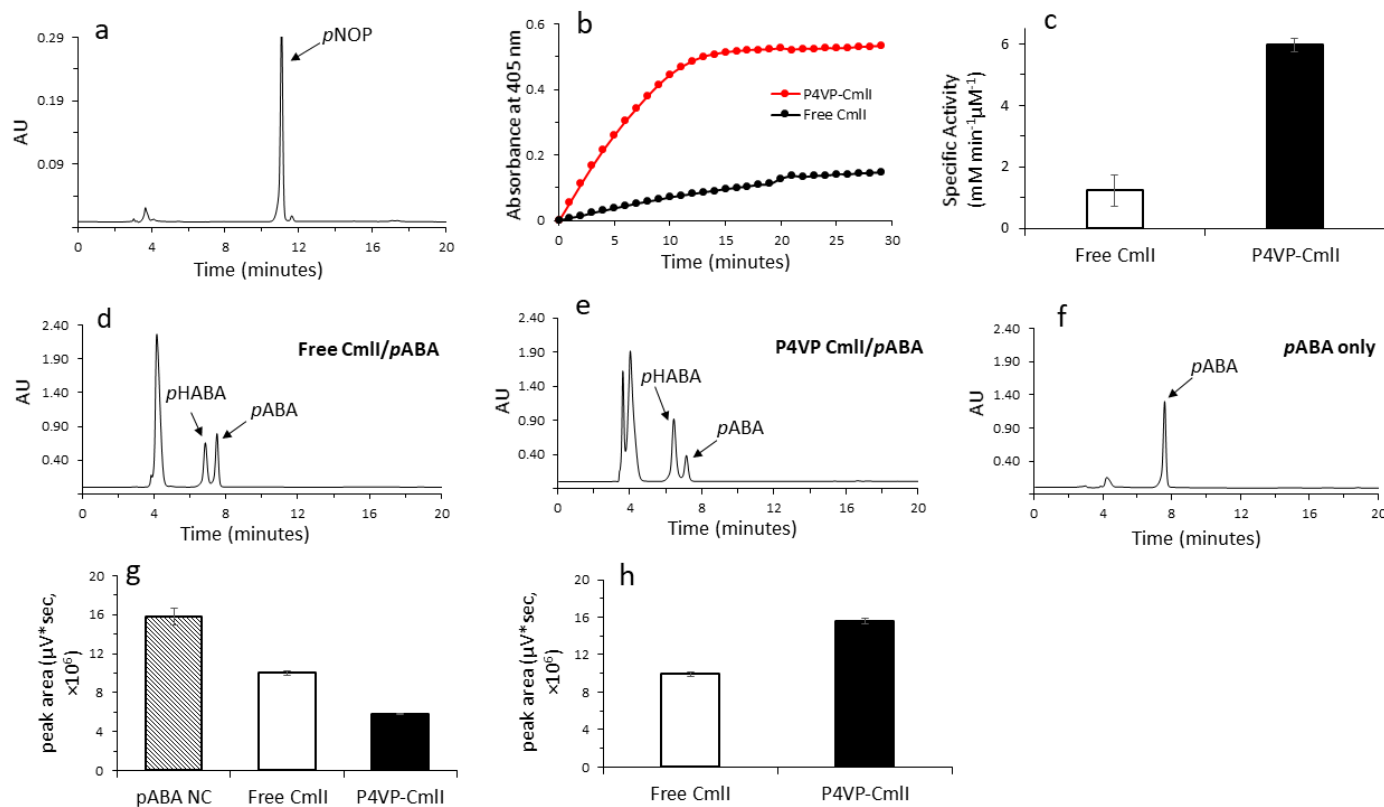
**Figure 1.3** Enzymatic activity analysis of P4VP-CmlI assemblies: 20 μM enzyme, 1 mM *p*AP or 1 mM *p*ABA, 2 mM NADH and 25 μM PMS in MOPS buffer (50 mM, pH 7.4). (a) HPLC analysis of the enzymatic oxidation products of *p*AP catalyzed with P4VP-CmlI. (b-c) Comparison of the activity of P4VP-CmlI and free CmlI using *p*AP based chromogenic assay, the signal at the first read was subtracted as background. (d-f) HPLC analysis of the oxidation products using *p*ABA as the substrate with free CmlI (d) and P4VP-CmlI as the catalyst (e) and the pure *p*ABA (f). (g-h) Activity comparison based on the consumption of starting material *p*ABA (g) and the production of the intermediate *p*HABA (h). Error bars represent the standard deviation of the mean of triplicate sample.

With P4VP assembly, all these enzyme functions were maintained. It is noteworthy that the activity of enzyme assembly with NADH/PMS method showed around 1.6 to 2.3 times increase compared to the activity carried out via the peroxide shunt method. In addition, the highly sensitive of P4VP-CmlI to NADH/PMS concentration, which will be discussed as below, makes the enzyme assemblies potentially used for synthetic applications. The enzyme activity results showed near-ideal enzyme activity behavior especially in the initial region. For longer reaction time, it showed a biphasic behavior. Although we still do not know the precise origins for such phenomenon, a similar observation has been also reported by another group.[16] To the best of our knowledge, this study is the first report that, with different substrates, products at different oxygenation stages can be selectively enriched by CmlI. Continued investigation using a wider substrate-scope may reveal new opportunities for synthetic applications.

### 1.2.3 ACTIVITY COMPARISON OF P4VP-CMLI AND FREE CMLI

In order to compare the catalytic efficiency of P4VP-CmlI and free CmlI, the free enzyme was tested under the same conditions used in the preparation of P4VP-CmlI. For *p*AP with NADH/PMS method, reactions were monitored by absorbance spectroscopy ($\lambda$ = 405 nm) to monitor the production of *p*NOP (**Figure 1.3b**). The specific activity of P4VP-CmlI was as much as 5 times higher than that of the free enzyme (**Figure 1.3c**). For *p*ABA, the activity of P4VP-CmlI was around ~ 1.6 times of that of free enzyme, as calculated by either the consumption of substrate (**Figure 1.3g**) or by *p*HABA production (**Figure 1.3h**) through the HPLC quantification.

17
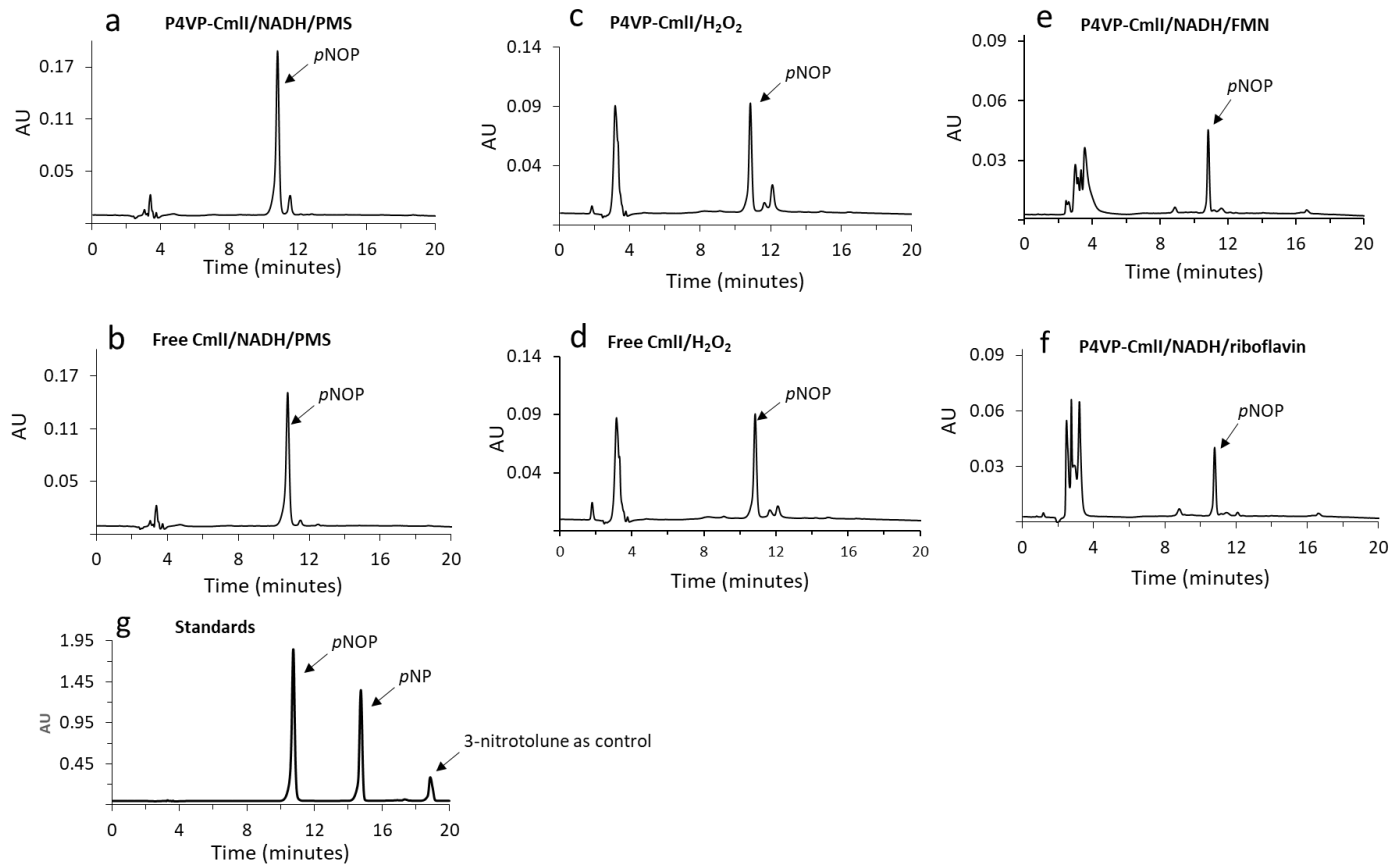
**Figure 1.4** HPLC result of P4VP-CmlI assembly and free CmlI enzyme reaction with *p*AP with different assays (a-b) the reactions with 2 mM NADH, 125 μM PMS (c-d) the reactions with 1.5% H₂O₂ (e) P4VP-CmlI catalyzed reaction with NADH/FMN (f) P4VP-CmlI catalyzed reaction with NADH/riboflavin. All the reactions were done in pH 7.4, 50 mM MOPS buffer at 30 minutes. (g) HPLC traces of *p*NOP and *p*NP standards.
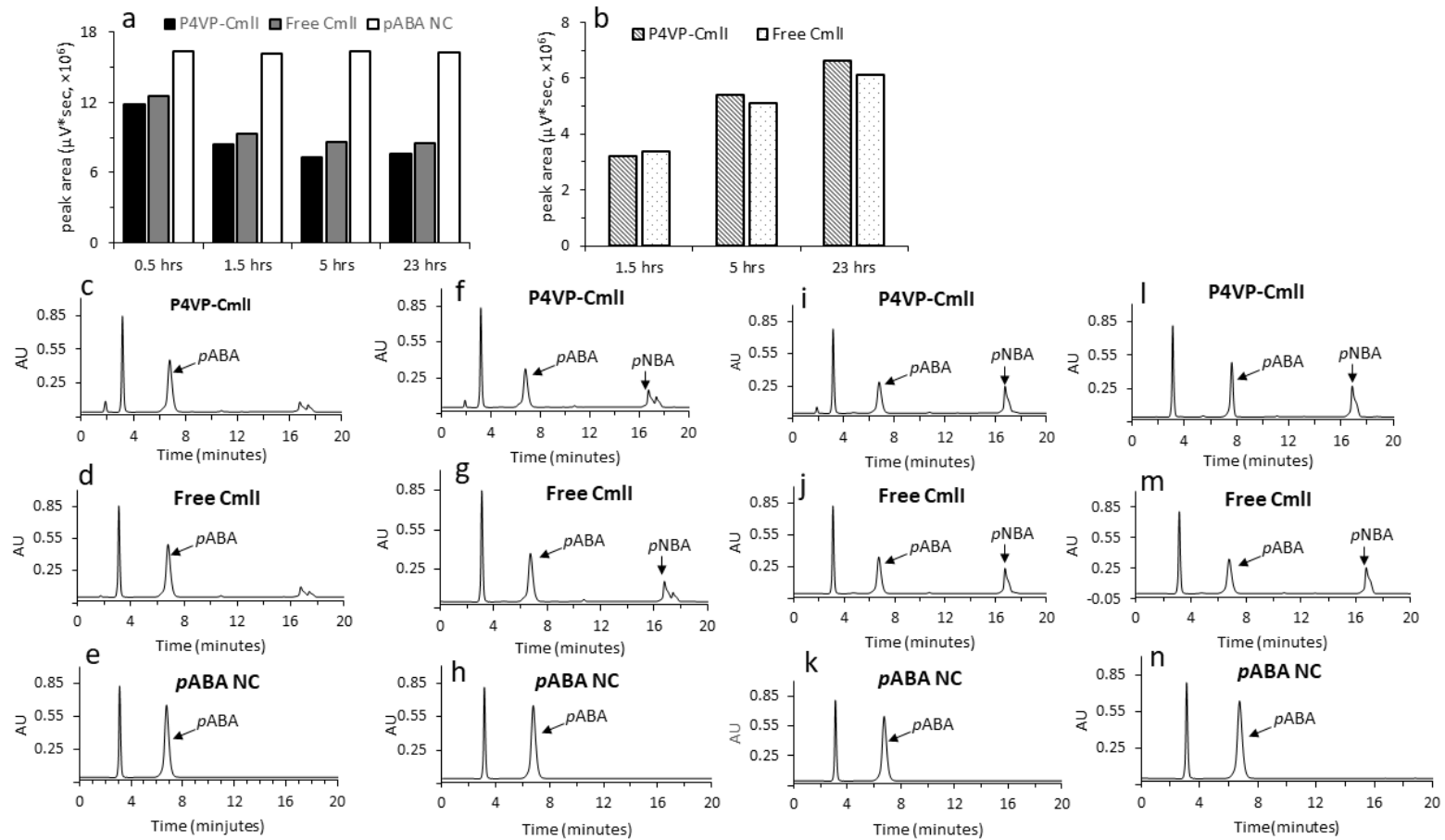
**Figure 1.5** P4VP-CmlI and free CmlI activity test with $H_2O_2$ method using $p$ABA as substrate. (a-b) Comparison based on the $p$ABA consumption (a) and $p$NBA production (b). HPLC results of the reactions at 0.5 hours (c-e), 1.5 hours (f-h), 5 hours (i-k), 23 hours (l-n) were reported.

The reaction of PMS and NADH has been reported to produce hydrogen peroxide,[47] which at high enough levels may contribute to enzyme activity. To test this possibility, 1 μM catalase was included in the CmlI/$p$AP/NADH/PMS reaction. Only minor differences in activity were observed upon the addition of the $H_2O_2$ scavenger (**Figure 1.6a**). This suggests that CmlI catalysis from pyridine nucleotide likely proceeds by a reductive mechanism where the peroxo-adduct is formed from electron transfer and subsequent $O_2$ binding. To further explore why P4VP-CmlI exhibits enhanced turnover rate, the enzymatic activity assay with $p$AP was performed at different NADH/PMS concentrations. As expected, when both NADH and PMS were at higher concentrations (NADH 10 mM, PMS 125 μM), both P4VP-CmlI and free CmlI showed higher activity due to sufficient and fast electron delivery (**Figure 1.6b**). However, when the concentration of PMS was increased to 125 μM but the NADH kept at 2 mM, the difference between the activities of P4VP-CmlI and free CmlI became negligible due to the dramatically increased turnover of the free enzyme (**Figure 1.6b**). This implies that the electron transferring process mediated by PMS could be facilitated in the P4VP-CmlI reaction and this difference was masked by increasing PMS concentration. It is noteworthy that product formation time course by CmlI showed a lag-phase, possibly due to a side reaction between the nitroso intermediate and NADH/PMS.[46] Interestingly, this effect can be rescued in the P4VP-CmlI catalyzed reaction (**Figure 1.6b**). This phenomenon could be attributed to potential interactions between P4VP polymer scaffold and PMS, which is still under investigation.

20
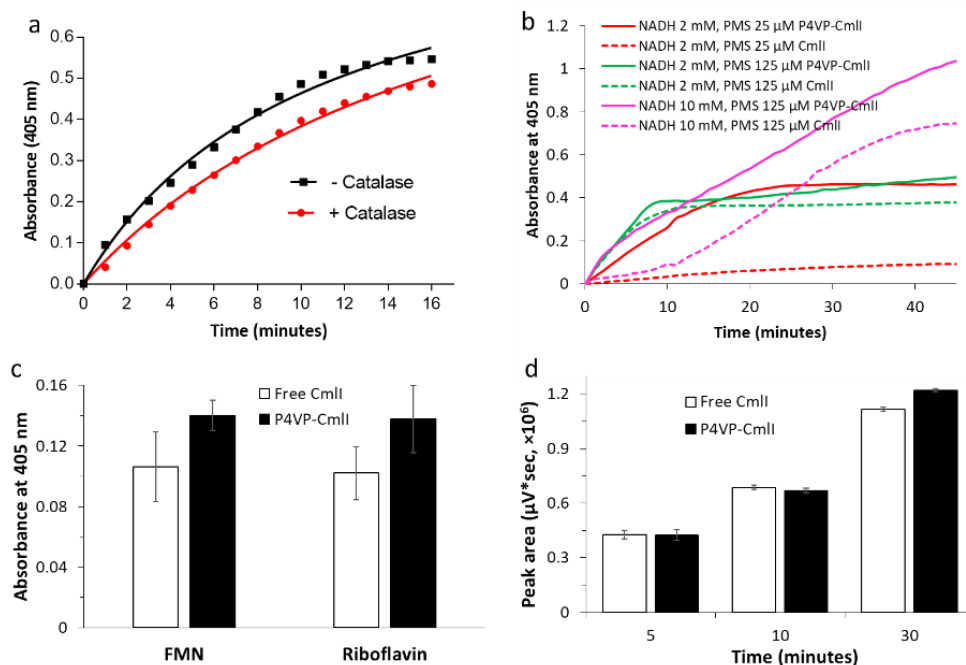
**Figure 1.6** Enzymatic activity comparison of P4VP-CmlI and free CmlI with adding catalase (a), with different PMS/NADH concentration (b), with NADH/FMN or NADH/riboflavin system (c) and by peroxo-shunt method (d). For (a), 25 μM CmlI was used in CmlI/NADH/PMS reaction, 25 μM CmlI and 1 μM catalase were used in CmlI/NADH/PMS + catalase reaction. All the reactions were done with 2.5 mM NADH, 125 μM PMS, 1 mM *p*AP, 7% ethanol in MOPS buffer (50 mM, pH 7.4). For (c), 1 mM NADH and 12.5 μM FMN or Riboflavin were used and the reaction was stopped at 60 minutes. For (d), 1.5% $H_2O_2$ (v/v) was used. From (b) to (d), the reactions were done with 20 μM enzyme, 1 mM *p*AP in MOPS buffer (50 mM, pH 7.4). Error bars represent the standard deviation of the mean of triplicate tests.

Flavin mononucleotide (FMN) and riboflavin, common biological redox partners used in a plethora of redox processes,[48–50] were utilized as alternative reducing systems. As shown in **Figure 1.6c** and consistent with the results from PMS, the activity of P4VP-CmlI was higher (~ 30%) than the free enzyme with *p*AP substrate. However, the overall efficiency was much lower than that of the NADH/PMS couple. Based on above data, we hypothesized that the origin of the enhanced activity for P4VP-CmlI may derive from an enhanced rate of electron delivery to form the diferrous cluster. To test this, the activity of P4VP-CmlI and free CmlI was compared to a peroxide-shunt method in which the reduction process was bypassed (Scheme 1). The result showed no significant activity

21

difference between the P4VP-CmlI and free CmlI (**Figure 1.6d**). This indicated that the enhanced activity of P4VP-CmlI using NADH was most likely from the enzyme reduction step. To further identify the effect of $H_2O_2$ on the stability and activity of peroxo CmlI intermediate in assembled and free conditions, the $H_2O_2$ pre-treatment study was performed. In this test, both P4VP-CmlI and free CmlI were pretreated with 1.5 % $H_2O_2$ (v/v) and aged for different times prior to the addition of *p*AP. There was no significant difference between P4VP-CmlI and CmlI indicating uncompromised stability and activity of both samples (**Figure 1.7**).

## 1.3.4 FMN REDUCTION TEST IN P4VP-CMLI AND FREE CMLI SOLUTIONS

In order to further demonstrate that an enhancement in electron transfer conferred higher activity in P4VP-CmlI, the transfer of electrons from NADH to FMN was tested by optical spectroscopy. NADH, in its reduced form, absorbs at 340 nm and oxidized FMN at 440 nm. The reduction of FMN by NADH can thus be monitored by the loss of absorbance at both wavelengths. The absorbance spectrum of P4VP-CmlI has background contributions due to scattering of the nanoparticles (**Figure 1.8**). As one could expect, oxidation of NADH occurs for both P4VP-CmlI and free CmlI due to the reaction of FMN and NADH. However, P4VP-CmlI shows a much faster rate of NADH oxidation (**Figure 1.9a**), and as a consequence, significantly faster FMN reduction (**Figure 1.9b-c**)

22
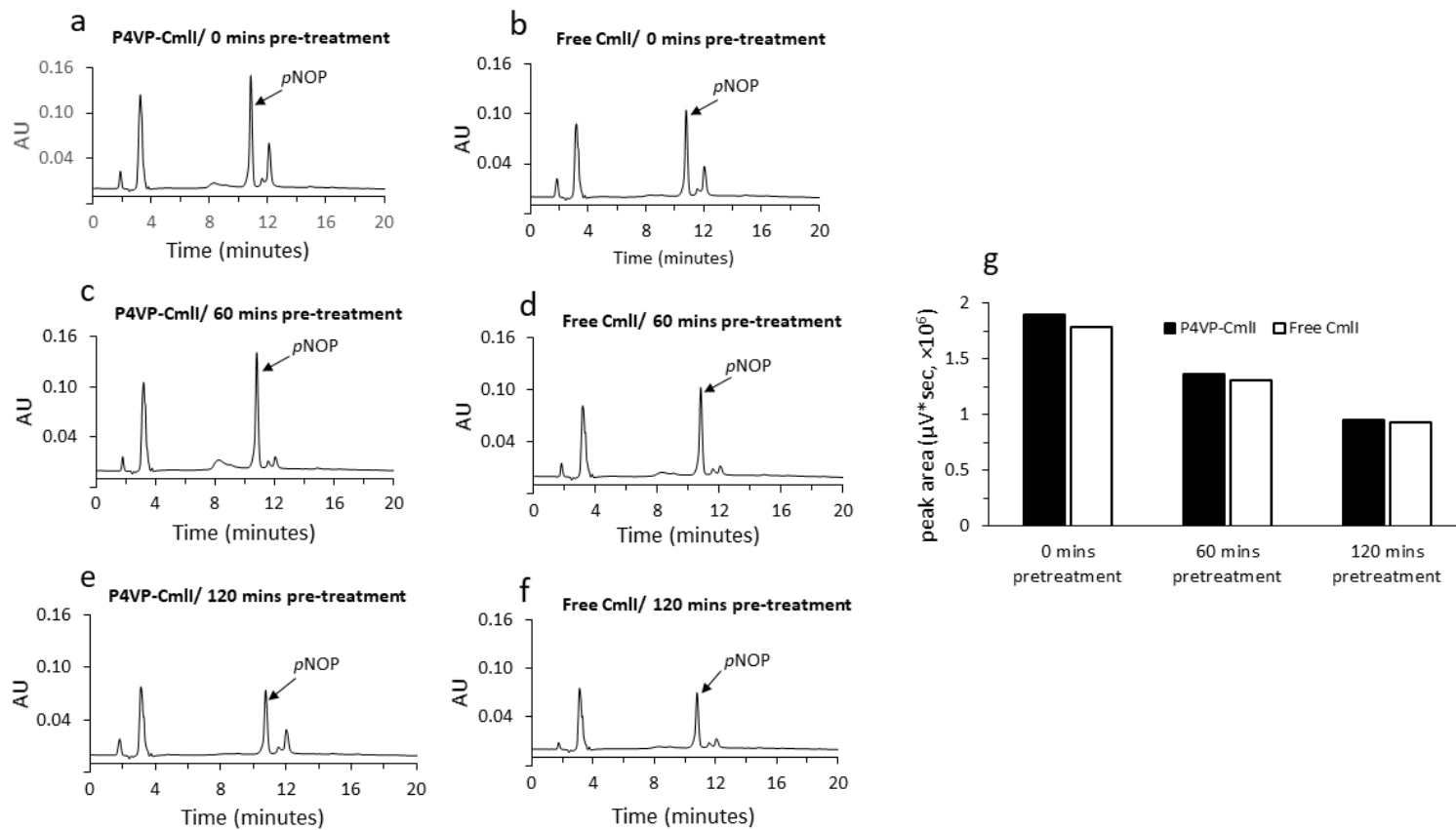
**Figure 1.7** P4VP-CmlI and free CmlI activity test with different time of $H_2O_2$ pretreatment using $p$AP as substrate. (a-f) HPLC result of corresponding reactions. (g) Activity comparison based on the $p$NOP production.
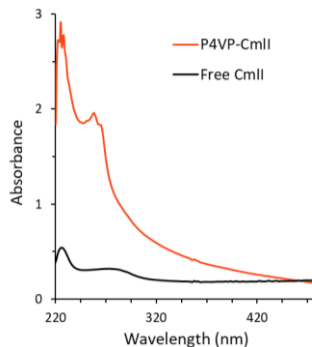
**Figure 1.8**. UV-Vis spectra of P4VP-CmlI solution and free CmlI solution at MOPS buffer.
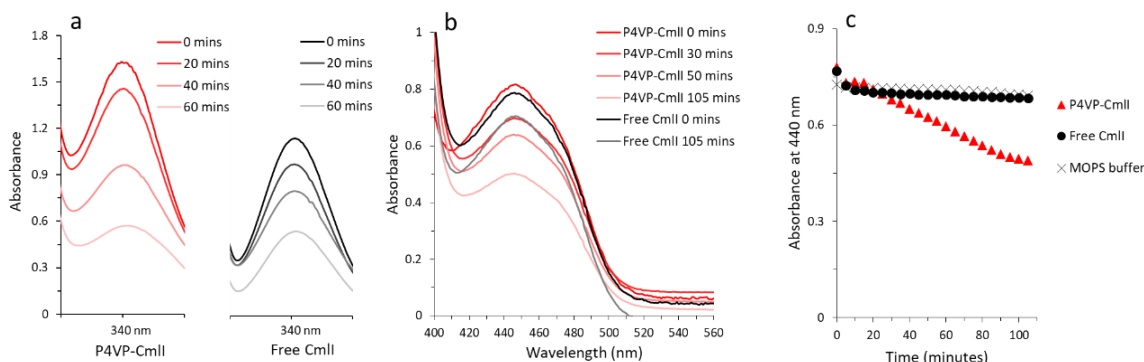


**Figure 1.9.** Reduction test of FMN by NADH in P4VP-CmlI and free CmlI solution. (a) UV-Vis spectra of P4VP-CmlI solution (red) and free CmlI solution (black) at MOPS buffer. (b) Time resolved FMN (30 µM) in presence of NADH signal (200 µM) in P4VP-CmlI and free CmlI solution. (c) Time courses for the reduction of FMN (50 µM) by NADH (5 mM) in P4VP-CmlI solution, free CmlI solution and MOPS buffer.

## 1.4 CONCLUSIONS

In this study, we have generated P4VP-CmlI core-shell nanoparticles via a facile self-assembly process and explored its activity with two substrates *p*AP and *p*ABA using both oxidative and reductive turnover methods. Nitroso- and nitro- products could be selectively produced with different substrates using different co-substrates to initiate the reaction. We found that the P4VP assembly could significantly increase CmlI activity using NADH as an electron source and appropriate electron mediators. As redox partners are required for the efficient turnover of CmlI but have yet to be identified, reconstitution of

24

the enzyme activity *in vitro* is a major challenge. The P4VP polymer assembly system improves the reduction of the enzyme in the absence of protein-based redox partners, and as a result, showed significant enhanced activity. P4VP is an inexpensive polymer available at an industrial scale, and the polymer-enzyme co-assembly process is both robust and facile. The P4VP-CmlI nanoparticles reported here could thus be easily used for synthetic applications.

## 1.5 REFERENCES

(1)     Ju, K.-S.; Parales, R. E. Nitroaromatic Compounds, from Synthesis to Biodegradation. *Microbiol. Mol. Biol. Rev. MMBR* **2010,** *74*, 250–272.

(2)     Gowenlock, B. G.; Richter-Addo, G. B. Preparations of C-Nitroso Compounds. *Chem. Rev.* **2004**, *104*, 3315–3340.

(3)     Strauss, M. J. The Nitroaromatic Group in Drug Design. Pharmacology and Toxicology (for Nonpharmacologists). *Ind. Eng. Chem. Prod. Res. Dev.* **1979**, *18*, 158–166.

(4)     Shanmugaraju, S.; Joshi, S. A.; Mukherjee, P. S. Fluorescence and Visual Sensing of Nitroaromatic Explosives Using Electron Rich Discrete Fluorophores. *J. Mater. Chem.* **2011**, *21*, 9130–9138.

(5)     Fan, F.-R. F.; Yao, Y.; Cai, L.; Cheng, L.; Tour, J. M.; Bard, A. J. Structure-Dependent Charge Transport and Storage in Self-Assembled Monolayers of Compounds of Interest in Molecular Electronics: Effects of Tip Material, Headgroup, and Surface Concentration. *J. Am. Chem. Soc.* **2004**, *126*, 4035–4042.

(6)     Ranganathan, D.; Rao, C. B.; Ranganathan, S.; Mehrotra, A. K.; Iyengar, R. Nitroethylene: A Stable, Clean, and Reactive Agent for Organic Synthesis. *J. Org. Chem.* **1980**, *45*, 1185–1189.

(7)     King, S. B. C-Nitroso Compounds, Oximes, N-Hydroxyguanidines and N-Hydroxyureas. In *Nitric Oxide Donors*; Wang, essor P. G.; Cai, T. B.; Taniguchi, essor N., Eds.; Wiley-VCH Verlag GmbH & Co. KGaA, 2005; pp. 177–199.

(8)     Yan, G.; Yang, M. Recent Advances in the Synthesis of Aromatic Nitro Compounds. *Org. Biomol. Chem.* **2013**, *11*, 2554–2566.

(9)     Schmid, A.; Dordick, J. S.; Hauer, B.; Kiener, A.; Wubbolts, M.; Witholt, B. Industrial Biocatalysis Today and Tomorrow. *Nature* **2001**, *409*, 258–268.

(10)    Choi, J.-M.; Han, S.-S.; Kim, H.-S. Industrial Applications of Enzyme Biocatalysis: Current Status and Future Aspects. *Biotechnol. Adv.* **2015**, *33*, 1443–1454.

(11)    Winkler, R.; Hertweck, C. Biosynthesis of Nitro Compounds. *ChemBioChem* **2007**, *8*, 973–977.

(12)    Lee, J.; Simurdiak, M.; Zhao, H. Reconstitution and Characterization of Aminopyrrolnitrin Oxygenase, a Rieske N-Oxygenase That Catalyzes Unusual Arylamine Oxidation. *J. Biol. Chem.* **2005**, *280*, 36719–36727.

(13)    He, J.; Hertweck, C. Biosynthetic Origin of the Rare Nitroaryl Moiety of the Polyketide Antibiotic Aureothin: Involvement of an Unprecedented N-Oxygenase. *J. Am. Chem. Soc.* **2004**, *126*, 3694–3695.

(14)    Simurdiak, M.; Lee, J.; Zhao, H. A New Class of Arylamine Oxygenases: Evidence That p-Aminobenzoate N-Oxygenase (AurF) Is a Di-Iron Enzyme and Further Mechanistic Studies. *ChemBioChem* **2006**, *7*, 1169–1172.

(15)    Li, N.; Korboukh, V. K.; Krebs, C.; Bollinger, J. M. Four-Electron Oxidation of p-Hydroxylaminobenzoate to p-Nitrobenzoate by a Peroxodiferric Complex in AurF from Streptomyces Thioluteus. *Proc. Natl. Acad. Sci.* **2010**, *107*, 15722–15727.

(16)    Lu, H.; Chanco, E.; Zhao, H. CmlI is an N-Oxygenase in the Biosynthesis of Chloramphenicol. *Tetrahedron* **2012**, *68*. 7651–7654.

(17)    Komor, A. J.; Rivard, B. S.; Fan, R.; Guo, Y.; Que, L.; Lipscomb, J. D. Mechanism for Six-Electron Aryl-N-Oxygenation by the Non-Heme Diiron Enzyme CmlI. *J. Am. Chem. Soc.* **2016**, *138*, 7411–7421.

(18)    Knoot, C. J.; Kovaleva, E. G.; Lipscomb, J. D. Crystal Structure of CmlI, the Arylamine Oxygenase from the Chloramphenicol Biosynthetic Pathway. *J. Biol. Inorg. Chem.* **2016**, *21*, 589–603.

(19)    Makris, T. M.; Vu, V. V.; Meier, K. K.; Komor, A. J.; Rivard, B. S.; Münck, E.; Que, L.; Lipscomb, J. D. An Unusual Peroxo Intermediate of the Arylamine Oxygenase of the Chloramphenicol Biosynthetic Pathway. *J. Am. Chem. Soc.* **2015**, *137*, 1608–1617.

(20)    Choi, Y. S.; Zhang, H.; Brunzelle, J. S.; Nair, S. K.; Zhao, H. In Vitro Reconstitution and Crystal Structure of P-Aminobenzoate N-Oxygenase (AurF) Involved in Aureothin Biosynthesis. *Proc. Natl. Acad. Sci.* **2008**, *105*, 6858–6863.

(21)    Platter, E.; Lawson, M.; Marsh, C.; Sazinsky, M. H. Characterization of a Non-Ribosomal Peptide Synthetase-Associated Diiron Arylamine N-Oxygenase from Pseudomonas Syringae Pv. Phaseolicola. *Arch. Biochem. Biophys.* **2011**, *508*, 39–45.

(22)    Chanco, E.; Choi, Y. S.; Sun, N.; Vu, M.; Zhao, H. Characterization of the N-Oxygenase AurF from Streptomyces Thioletus. *Bioorg. Med. Chem.* **2014**, *22*, 5569–5577.

(23)    Andersson, K. K.; Froland, W. A.; Lee, S.-K.; Lipscomb, J. D. Dioxygen Independent Oxygenation of Hydrocarbons by Methane Monooxygenae Hydroxylase Component. *Nouv. J. Chim.* **1991**, *15*, 411–415.

(24)    Bailey, L. J.; Fox, B. G. Crystallographic and Catalytic Studies of the Peroxide-Shunt Reaction in a Diiron Hydroxylase. *Biochemistry (Mosc.)* **2009**, *48*, 8932–8939.

(25)    Suthiwangcharoen, N.; Nagarajan, R. Enhancing Enzyme Stability by Construction of Polymer–Enzyme Conjugate Micelles for Decontamination of Organophosphate Agents. *Biomacromolecules* **2014**, *15*, 1142–1152.

(26)    Kawamura, A.; Harada, A.; Kono, K.; Kataoka, K. Self-Assembled Nano-Bioreactor from Block Ionomers with Elevated and Stabilized Enzymatic Function. *Bioconjug. Chem.* **2007**, *18*, 1555–1559.

(27)    Cummings, C.; Murata, H.; Koepsel, R.; Russell, A. J. Dramatically Increased PH and Temperature Stability of Chymotrypsin Using Dual Block Polymer-Based Protein Engineering. *Biomacromolecules* **2014**, *15*, 763–771.

(28)    Lee, H.; Park, T. G. Conjugation of Trypsin by Temperature-Sensitive Polymers Containing a Carbohydrate Moiety: Thermal Modulation of Enzyme Activity. *Biotechnol. Prog.* **1998**, *14*, 508–516.

(29)    Lee, E.-H.; Tsujimoto, T.; Uyama, H.; Sung, M.-H.; Kim, K.; Kuramitsu, S. Enhancement of Enzyme Activity and Stability by Poly (γ-Glutamic Acid). *Polym. J.* **2010**, *42*, 818–822.

(30)    Zhang, Y.; Ge, J.; Liu, Z. Enhanced Activity of Immobilized or Chemically Modified Enzymes. *ACS Catal.* **2015**, *5*, 4503–4513.

(31)    Li, T.; Niu, Z.; Emrick, T.; Russell, T. P.; Wang, Q. Core/Shell Biocomposites from the Hierarchical Assembly of Bionanoparticles and Polymer. *Small* **2008**, *4*, 1624–1629.

(32)    Li, T.; Ye, B.; Niu, Z.; Thompson, P.; Seifert, S.; Lee, B.; Wang, Q. Closed-Packed Colloidal Assemblies from Icosahedral Plant Virus and Polymer. *Chem. Mater.* **2009**, *21*, 1046–1050.

(33)     Li, T.; Niu, Z.; Suthiwangcharoen, N.; Li, R.; Prevelige, P. E.; Wang, Q. Polymer-Virus Core-Shell Structures Prepared via Co-Assembly and Template Synthesis Methods. *Sci. China Chem.* **2010**, *53*, 71–77.

(34)     Wu, L.; Li, T.; Blom, D.; Zhao, J.; Ghoshroy, S.; Wang, Q. Synthesis and Electron Microscopic Analysis of the Self-Assembly of Polymer and Ferritin Core-Shell Structures. *Microsc. Res. Tech.* **2011**, *74*, 636–641.

(35)     Li, T.; Wu, L,.; Suthiwangcharoen, N,. Bruckman, A M.; Cash, D.; JoAn, S. Hudson S, J; Ghoshroyc, S.; Wang, Qi. Controlled assembly of rodlike viruses with polymers - *Chem. Commun.* **2009***, 20*, 2869-2871.

(36)     Suthiwangcharoen, N.; Li, T.; Wu, L.; Reno, H. B.; Thompson, P.; Wang, Q. Facile Co-Assembly Process to Generate Core–Shell Nanoparticles with Functional Protein Corona. *Biomacromolecules* **2014**, *15*, 948–956.

(37)     Lu, L.; Yuan, L.; Yan, J.; Tang, C.; Wang, Q. Development of Core–Shell Nanostructures by In Situ Assembly of Pyridine-Grafted Diblock Copolymer and Transferrin for Drug Delivery Applications. *Biomacromolecules* **2016**, *17*, 2321–2328.

(38)     Zhang, X.; Zhao, X.; Luckanagul, J. A.; Yan, J.; Nie, Y.; Lee, L. A.; Wang, Q. Polymer–Protein Core–Shell Nanoparticles for Enhanced Antigen Immunogenicity. *ACS Macro Lett.* **2017**, *6*, 442–446.

(39)     Lu, H.-F.; Chan, H. S. O.; Ng, S.-C. Synthesis, Characterization, and Electronic and Optical Properties of Donor−Acceptor Conjugated Polymers Based on Alternating Bis(3-Alkylthiophene) and Pyridine Moieties. *Macromolecules* **2003**, *36*, 1543–1552.

(40)     Rochat, S.; Swager, T. M. Water-Soluble Cationic Conjugated Polymers: Response to Electron-Rich Bioanalytes. *J. Am. Chem. Soc.* **2013**, *135*, 17703–17706.

(41)     Willner, I.; Riklin, A.; Lapidot, N. Electron-Transfer Communication between a Redox Polymer Matrix and an Immobilized Enzyme: Activity of Nitrate Reductase in a Viologen-Acrylamide Copolymer. *J. Am. Chem. Soc.* **1990**, *112*, 6438–6439.

(42)     McMillan, D. G. G.; Marritt, S. J.; Firer-Sherwood, M. A.; Shi, L.; Richardson, D. J.; Evans, S. D.; Elliott, S. J.; Butt, J. N.; Jeuken, L. J. C. Protein–Protein Interaction Regulates the Direction of Catalysis and Electron Transfer in a Redox Enzyme Complex. *J. Am. Chem. Soc.* **2013**, *135*, 10550–10556.

(43)     Suzuki, R.; Hirakawa, H.; Nagamune, T. Electron Donation to an Archaeal Cytochrome P450 Is Enhanced by PCNA-Mediated Selective Complex Formation with Foreign Redox Proteins. *Biotechnol. J.* **2014**, *9*, 1573–1581.

(44)    Stookey, L. L. Ferrozine - a New Spectrophotometric Reagent for Iron. *Anal. Chem.* **1970**, *42*, 779–781.

(45)    Halaka, F. G.; Babcock, G. T.; Dye, J. L. Properties of 5-Methylphenazinium Methyl Sulfate. Reaction of the Oxidized Form with NADH and of the Reduced Form with Oxygen. *J. Biol. Chem.* **1982**, *257*, 1458–1461.

(46)    Leskovac, V.; Svircević, J.; Trivić, S.; Popović, M.; Radulović, M. Reduction of Aryl-Nitroso Compounds by Pyridine and Flavin Coenzymes. *Int. J. Biochem.* **1989**, *21*, 825–834.

(47)    Halliwell, B. Hydroxylation of Aromatic Compounds by Reduced Nicotinamide-Adenine Dinucleotide and Phenazine Methosulphate Requires Hydrogen Peroxide and Hydroxyl Radicals, but Not Superoxide. *Biochem. J.* **1977**, *167*, 317–320.

(48)    Gutman, M. Electron Flux through the Mitochondrial Ubiquinone. *Biochim. Biophys. Acta BBA - Rev. Bioenerg.* **1980**, *594*, 53–84.

(49)    Iyanagi, T.; Xia, C.; Kim, J.-J. P. NADPH-Cytochrome P450 Oxidoreductase: Prototypic Member of the Diflavin Reductase Family. *Arch. Biochem. Biophys.* **2012**, *528*, 72–89.

(50)    Ellis, H. R. The FMN-Dependent Two-Component Monooxygenase Systems. *Arch. Biochem. Biophys.* **2010**, *497*, 1–12.

CHAPTER 2

ENHANCED P450 OLET$_{SA}$ CATALYSIS PROMOTED BY COUPLING WITH

GLUCOSE OXIDASE AND CO-ASSEMBLY

## 2.1 INTRODUCTION

Driven by shortage of fossil fuel reserves and increasing environmental concerns, tremendous efforts have been undertaken to transform bio-based feedstock into chemicals[1,2] and fuels[3–5]. Among them, the conversion of bioavailable carboxylic acids (e.g., fatty acids) into terminal alkenes attracts attention because of their applications as next-generation fuels and key chemicals for the production of lubricants, surfactants, detergents, plastics, etc.[6–9] To achieve this goal, different methodologies have been developed such as esterification, amidation [10] and chemical reductions[11,12]. Despite of the success of these methods, the requirement of precious transition metal catalysts and the harsh reaction conditions often raise environmental concerns. Therefore, enzyme-catalyzed oxidative decarboxylation reactions that can directly produce terminal alkenes in mild conditions provide viable alternative approaches.[13–15]

A promising enzymatic alternative, cytochrome P450 OleT from *Jeotgalicoccus sp.* 8456, was first identified as an efficient olefin producer by Rude and coworkers.[16] OleT catalyzes the oxidative decarboxylation of fatty acids to yield primarily terminal alkenes and $CO_2$ or minor α- and β-hydroxylated fatty acids side-products.[16–18] Whereas the majority of P450s activate atmospheric $O_2$ using pyridine dinucleotide as a reducing source and an auxiliary redox chain,[19] OleT utilizes $H_2O_2$ as the only electron- and oxygen-source throughout the catalytic cycle (**Figure 2.1a**).[20] Unlike NAD(P)H, $H_2O_2$ is inexpensive and easily scalable, and previous efforts have sought to rewire P450s for efficient peroxide utilization.[21] However, the low turnover rate and low stability in the presence of excess $H_2O_2$ limit the practical use of OleT. Very recently, a functional ortholog from *Staphylococcus aureus,* $OleT_{SA}$,[22,23] was characterized by the Makris group and others that

possesses improved features including enhanced solubility and high stability. These features enable this ortholog to be a promising candidate for production applications.
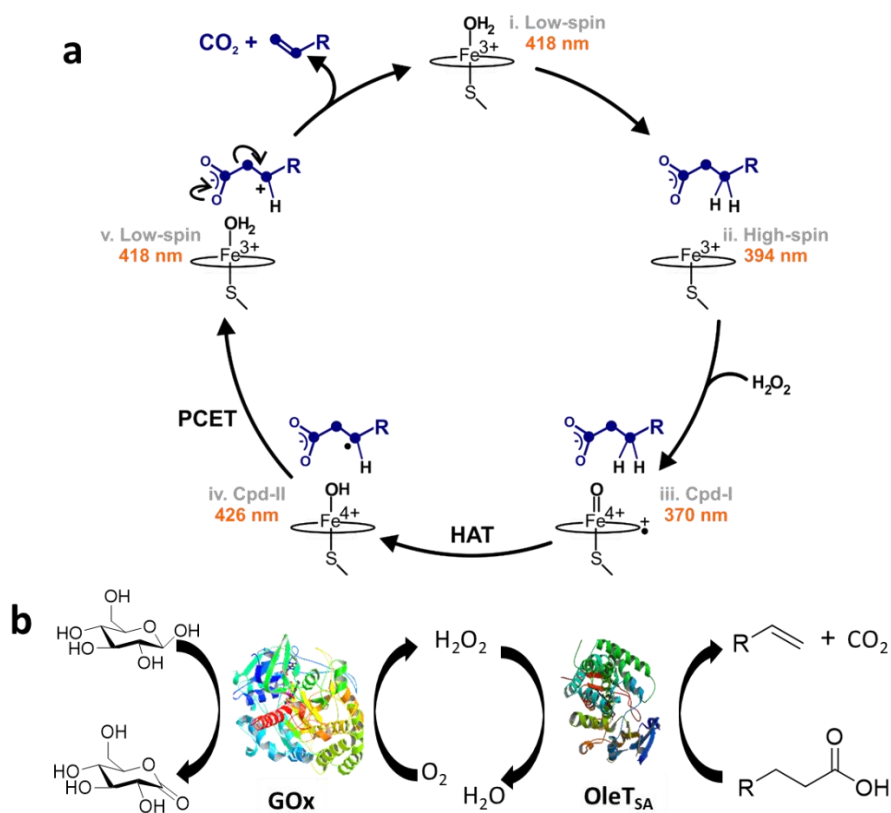


**Figure 2.1** a) Scheme of the cytochrome P450 OleT enzyme catalytic cycle. OleT is in a low-spin ferric resting state with its heme iron axially coordinated by cysteine thiolate and a $H_2O$ molecule, which shows a maximum Soret band at 418 nm.[24] Substrate binding displaces the axial water and converts the heme iron from low-spin to a high-spin state with a maximum Soret band at 394 nm.[24] Subsequent $H_2O_2$ activation forms Compound I,[18] which abstracts a hydrogen atom from the $C_\beta$ position (HAT step), resulting in formation of a substrate radical and the $Fe^{4+}$-hydroxo species (compound II).[25] Further substrate oxidation, and recruitment of a proton results in the elimination of $CO_2$ (PCET step) and terminal alkene formation. b) Schematic representation of GOx/OleTSA cascade using glucose as a substrate to produce $H_2O_2$ in situ.

One major issue of the $H_2O_2$-dependent biocatalysts towards their industrial applications is enzyme inactivation.[26] High concentrations of peroxide will generally oxidize key amino acids (e.g. methionine, tryptophan) in the vicinity of enzyme active site[27–29] or directly destroy the porphyrin cofactor, resulting in bleaching of the heme.[30,31] To alleviate this issue, different strategies have been explored such as enzyme

www.manaraa.com

engineering,[28,32–34] immobilization,[35–37] or the development of *in situ* $H_2O_2$ production methods,[38,39] Among them, controlling the concentration of peroxide during the catalytic reactions by employing *in situ* generation techniques provides a facile way to reduce the peroxide-related enzyme inactivation.[26,40,41] To date, photochemical and biological approaches that generate $H_2O_2$ in a controlled manner have been reported to leverage OleT enzyme catalysis. Zachos and colleagues described an *in situ* $H_2O_2$-generation system that uses light to excite flavin cofactors with ethylenediaminetetraacetic acid (EDTA) as an electron donor, which converts dioxygen to $H_2O_2$ to active the OleT$_{JE}$ enzyme for terminal alkene production.[42,43] Matthews *et al.* reported an enzyme genetic fusion system in which OleT$_{JE}$ was linked to alditol oxidase (AldO). With this system, polyol substrates were fed as AldO substrates to generate $H_2O_2$.[44]

In this work, we report the use of glucose oxidase (GOx) and sugars as substrates to efficiently drive OleT$_{SA}$ catalysis in an adjustable manner (**Figure 2.1b**). GOx is a flavoenzyme that metabolizes D-glucose by using molecular oxygen as an electron acceptor with simultaneous production of $H_2O_2$.[45] GOx is widely used in food, textile, and glucose-sensing industries because of its high stability and catalytic efficiency.[46] Other substrates of GOx include D-mannose, D-galactose and D-xylose,[47] which are all abundant and renewable feedstocks. Moreover, GOx has significantly varied kinetics with different substrates,[47,48] which enables one to regulate the $H_2O_2$-generating process. The data presented in this manuscript demonstrates improved catalytic efficiency of OleT enzyme when coupled with the GOx enzyme (the GOx method) compared to a single injection of $H_2O_2$ (the $H_2O_2$ method). We rationalize that the GOx-based *in situ* $H_2O_2$-generation method poises $H_2O_2$ concentrations at a level compatible with OleT catalysis while

minimizing the heme destruction during the catalysis. Finally, we use a poly(4-vinylpyridine) (P4VP) polymer to co-assemble GOx and OleT$_{SA}$ enzymes to generate nanoparticles (NPs) in order to further optimize enzyme cascade catalytic efficiency. The combination of the GOx-based method and the dual enzyme co-assembly with polymers provides a novel way to leverage OleT enzyme catalysis, which can be potentially used for synthetic applications.

## 2.2 EXPERIMENTAL SECTION

### 2.2.1 MATERIALS

GOx from *Aspergillus niger* and H$_2$O$_2$ were purchased from Sigma. Eicosanoic acid (C20:0), stearic acid (C18:0), palmitic acid (C16:0), myristic acid (C14:0), lauric acid (C12:0), and capric acid (C10:0) were purchased from BDH Chemicals. The alkene standard 1-hexadecene was purchased from TCI chemicals. D-Glucose, D-mannose, D-galactose were purchased from Fisher. Hydrocinnamic acid, 3-(4-bromophenyl) propionic acid, indole-3-butyric acid, 3-(4-methoxyyphennyl) propionic acid and P4VP (Mw 60000) were purchased from Sigma-Aldrich. *N,O*-Bis(trimethylsilyl)trifluoroacetamide (BSTFA)/trimethylchlorosilane (TMCS) (99:1) were purchased from Supelco (Bellefonte, PA, USA). Unless otherwise noted, all chemicals and solvents used were of analytical grade and were used as received from commercial sources. Unless otherwise noted, 200 mM K$_2$HPO$_4$, 100 mM NaCl, pH 7.4 was used as buffer.

### 2.2.2. HETEROLOGOUS EXPRESSION AND PURIFICATION OF OLET$_{SA}$

The original OleT$_{SA}$ gene was synthesized and codon optimized for *E. coli* expression by Bio Basic Inc. (Markham, Ontario). The gene was subcloned onto a kanamycin-resistant T5 plasmid pJ401containing a C-terminal HisTag. The construct was

34

transformed into BL21(DE3) containing the pTF2 plasmid encoding for GroEL/GroES/Tig onto a kanamycin (50 μg/mL)/chloramphenicol (30 μg/mL) LB plate. Modified Terrific Broth (TB) (24 g/L yeast extract, 12 g/L tryptone, 4 g/L peptone) supplemented with 50 μg/mL kanamycin and 20 μg/mL chloramphenicol was used to grow a cell culture from a single colony overnight at 37 °C. For protein expression, 10 mL of this starter culture was used to inoculate 500 mL of TB containing 50 μg/mL kanamycin, 30 μg/mL chloramphenicol, 125 mg/L thiamine, and trace metals.[22] The cultures were grown to an $OD_{600 \, nm}$ of 1.0, at which point protein expression was induced with 100 μM IPTG, 10 ng/mL tetracycline and 10 mg/L of 5-aminolevulinic acid. The culture was incubated at 18 °C for an additional 16-18 h and harvested by centrifugation for purification or for storage at -80 °C until further use. The protein was purified using nickel-nitriloacetic acid (Ni-NTA) affinity chromatography followed by Butyl-S-Sepharose column purification as described previously.[22] Fractions with an $R_z$ value ($Abs_{418 \, nm}/Abs_{280 \, nm}$) above 1.2 were pooled and dialyzed against 200 mM KPi pH 8. Proteins were stored at -80 °C until further use. Enzyme purity was assessed by SDS-PAGE.

### 2.2.3. OLET$_{SA}$ ENZYME ACTIVITY ASSAYS

Eicosanoic acid and stearic acid stock (10 mM) were dissolved in 70% ethanol/30% Triton X-100 (unless otherwise noted) as stocks. Other fatty acids including palmitic acid, myristic acid and lauric acid were dissolved in DMSO to make 10 mM stocks. Hydrocinnamic acid was dissolved in DMSO to make a 400 mM stock. To set up enzymatic reactions, 5 μM OleT$_{SA}$, 500 μM or 1 mM fatty acids or 1 mM hydrocinnamic acid (unless otherwise noted) from above stocks were used for multiple-turnover reactions in a 150 μL volume. $H_2O_2$ was added at a concentration of 2 mM to initiate the reactions in $H_2O_2$

method, while 10 nM to 5 μM GOx was added to initiate the reactions in GOx method. D-glucose, D-mannose, or D-galactose (6.6 mM) were used in the GOx method unless otherwise noted. The steady-state reactions were quenched with 0.4 mM HCl or 1% acetic acid for GC/GC-MS or LC/LC-MS analysis, respectively.

### 2.2.4. HEME DECAY MONITORING

Heme decay was monitored with UV-Visible spectroscopy on an HP 8453 spectrophotometer. A quartz cuvette with 1 cm path length was used. For the heme decay monitoring during GOx- or $H_2O_2$-driven reactions, 5 μM $OleT_{SA}$, 0.5 mM eicosanoic acid in the presence of 2 mM $H_2O_2$ or 10 nM GOx and 6.6 mM glucose were used. $OleT_{SA}$ spectra were recorded over time for 1 h at room temperature. Active enzyme concentration was determined from the total thiolate-ligated heme in the sample, based on the extinction coefficients of the Soret peaks: at 418 nm, 112.8 $mM^{-1}cm^{-1}$ for low-spin fraction, 56.6 $mM^{-1}cm^{-1}$ for high-spin fraction; 86.8 $mM^{-1}cm^{-1}$ at 406 nm; at 394 nm, 50 $mM^{-1}cm^{-1}$ for low-spin fraction, 106.5 $mM^{-1}cm^{-1}$ for high-spin fraction.[22]

### 2.2.5. GAS CHROMATOGRAPHY (GC) ANALYSIS

For gas chromatographic quantification of fatty acid metabolism by $OleT_{SA}$, internal standards including 1-hexadecene and a $C_{n-2}$ fatty acid (relative to substrate of chain-length $C_n$) were added after the reactions were quenched with 300 mM HCl. The reactions were extracted with 300 μL chloroform. The organic phases of each reaction were tested on GC directly or derivatized before GC analysis. For derivatization, samples were concentrated under a stream of $N_2$ gas to less than 50 μL, then derivatized with 250 molar equivalents of BSTFA: TMCS (99:1). Samples were incubated at 60 °C for 20 minutes for trimethylsilylation. Following the derivatization, samples were analyzed by GC. The

following oven conditions were used to detect products of C20 through C16 fatty acids: 170 °C for 3 min, 10 °C/min to 220 °C, 5 °C/min to 320 °C, and 320 °C for 3 min. The following oven conditions were used to detect products of C14 and C12 fatty acids metabolism: 100 °C for 3 min, 5 °C/min to 250 °C and 250 °C for 3 min. The response factors between fatty acids, hydroxyl fatty acids and alkenes were determined by analyzing known authentic fatty acids (C18-C10) and 1-hexadecene standards.

### 2.2.6. HPLC AND MS ANALYSIS

Reactions (total volume = 150 μL) with hydrocinnamic acid were quenched by acetic acid (final concentration 1% v/v). After quenching, 1,2,3,4-tetramethyl benzene was added as internal control and the mixture was extracted with ethyl acetate (300 μL). For each sample, 20 μL of organic layer was were injected in an Agilent 1100 HPLC equipped with a ZORBAX SB-C18 column. HPLC parameters were as follows: 25 °C; solvent A, 1% acetic acid in water; solvent B, methanol; gradient, 10% B for 2 min; then, from 10% B to 100% B over 32 min; then, from 100% B to 10% B over 10 min, flow rate, 0.5 mL/min. Detection of the products was by UV absorbance at 250 nm. Quantification of product was calculated from a calibration curve of styrene with the same extraction method. The identity of the styrene product was confirmed by LC-MS at the Mass Spectrometry Center, University of South Carolina.

### 2.2.7. SYNTHESIS OF P4VP-GOX-OLET$_{SA}$ ASSEMBLIES AND CHARACTERIZATION

A solution of P4VP in ethanol (2.5 mg·mL$^{-1}$, 0.1 mL) was slowly added to a solution containing 1 μM OleT$_{SA}$ and 1 μM GOx in buffer A (0.9 mL) with stirring. After addition, the mixture was stirred for an additional 10 min for equilibration. Because of the

37

high loading capacity,[49] the co-assemblies was not purified before characterization and activity test. The size distribution of P4VP-GOx-OleT assemblies were measured with dynamic light scattering (DLS, Zetasizer Nano ZS, Malvern Instruments). For TEM analysis, P4VP-GOx-OleT samples prepared above were diluted 10 times with water, and 20 µL of diluted samples were dropped onto 250-mesh carbon-coated copper grids and dried. The grids were observed with a Hitachi H-8000 electron microscope at the Electron Microscopy Center, University of South Carolina.

## 2.2.8. ACTIVITY COMPARISON OF P4VP-GOX-OLET$_{SA}$ ASSEMBLIES AND FREE GOX/OLET ENZYME CASCADE

The activities of both P4VP-GOx-OleT$_{SA}$ and free enzyme cascade were assessed in a reaction volume of 250 µL containing GOx and OleT$_{SA}$ (1 µM/each), hydrocinnamic acid (2 mM) or myristic acid (1 mM). Reactions were initiated by the addition of mannose (6.6 mM) to the reaction mixture and incubated at room temperature (23 – 25°C). In the control reactions, GOx and mannose were omitted from the reaction sample and instead, 2 mM $H_2O_2$ was used to initiate the reactions. A stock solution of 400 mM hydrocinnamic acid was prepared in DMSO. The final organic solvent concentration in the reaction is 4.1% ethanol and 1% DMSO for each sample. The reaction was quenched by the addition of 1% acetic acid, and an internal standard of 1,2,3,4-tetramethyl benzene was added. The products were exected with 300 µL ethyl acetate and analyzed by LC or GC as described above.

## 2.2.9. CATALASE COMPETITION ASSAY

Catalase, as a scavenger for $H_2O_2$, was added to the enzymatic reactions catalyzed by assembled enzyme cascade (P4VP-GOx-OleT$_{SA}$) and free GOx/OleT$_{SA}$ to measure the

38

differences. A serial concentration of catalase from 15.6 nM to 250 nM was added into the reaction mixtures containing GOx and OleT$_{SA}$ (1 µM/each), hydrocinnamic acid (2 mM), and mannose (6.6 mM). As above, the reactions were initiated by the addition of mannose and quenched by the addition of 1% acetic acid, and 1,2,3,4-tetramethyl benzene was added as internal standard. The reactions were exacted by 300 µL ethyl acetate and analyzed by LC.

## 2.3 RESULTS AND DISCUSSION

### 2.3.1 H$_2$O$_2$ CONCENTRATION DEPENDENCE OF OLET$_{SA}$ ACTIVITY AND HEME BLEACHING

OleT$_{SA}$ enzyme was purified using Ni column affinity chromatography followed by hydrophobic interaction chromatography (Butyl-Sepharose) (**Figure 2.2**). As shown in **Figure 2.3a**, a certain level of H$_2$O$_2$ is necessary to drive OleT$_{SA}$ enzymatic catalysis to form oxidizing species known as Compound I. However, with excess H$_2$O$_2$, the enzyme displays low substrate conversion,[41,50] suggesting peroxide-mediated enzyme inactivation. To characterize the H$_2$O$_2$ concentration dependence of OleT$_{SA}$ enzymatic activity, varying concentrations of H$_2$O$_2$ were added in the enzyme reaction with eicosanoic acid as the substrate. Nonadecene production (which is the sole product of eicosanoic acid reaction)[22] was used to calculate the product conversion rate. As shown in **Figure 2.3a**, with increasing H$_2$O$_2$ concentration from 0.05 mM to 2 mM, increased conversions from 4% to 12% were obtained. On the other hand, increasing the H$_2$O$_2$ concentration further from 2 mM to 40 mM led to a decreased conversion. A similar trend was also observed for OleT$_{SA}$-catalyzed styrene production using hydrocinnamic acid as substrate (**Figure 2.4**). These results demonstrate that the H$_2$O$_2$ concentration has a dramatic effect on OleT$_{SA}$ catalytic efficiency.

39
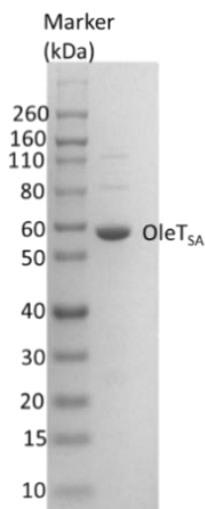
**Figure 2.2** SDS-PAGE gel of the purified OleT$_{SA}$
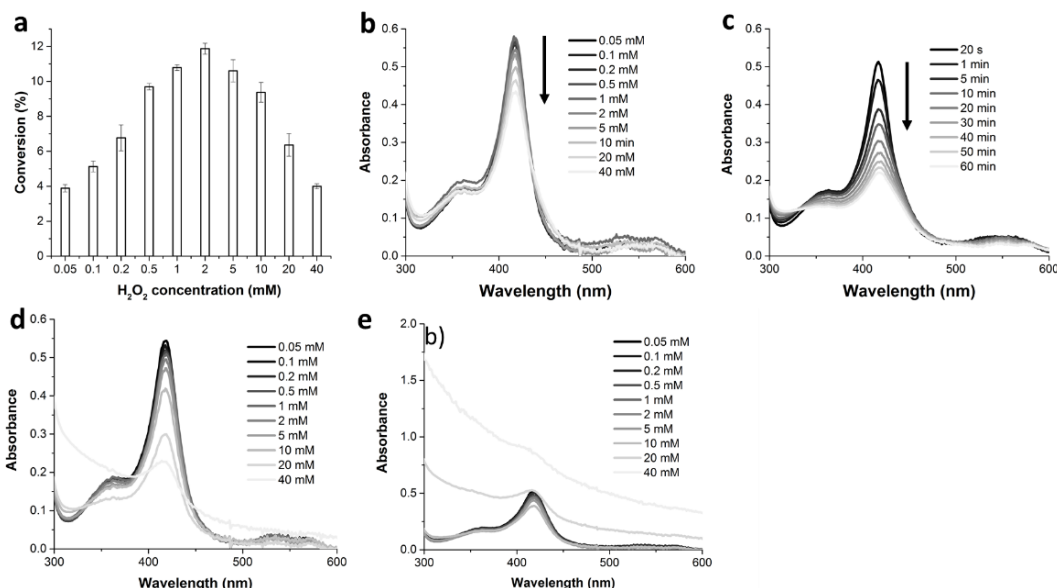


**Figure 2.3** The H$_2$O$_2$ concentration dependence of OleT$_{SA}$ enzyme activity (a) and the Soret band intensity (b-c). (a) Comparison of the reaction rate of the conversion of eicosanoic acid to nonadecene by OleT$_{SA}$ with various H$_2$O$_2$ concentrations. The reaction conditions are as follows: OleT$_{SA}$ 5 μM, eicosanoic acid 1 mM, H$_2$O$_2$ 0.05 mM - 40 mM, room temperature for 30 min. Error bars indicate the standard deviation of two independent experiments (n = 2). (b) The UV-Vis spectra of 5 μM OleT$_{SA}$ was recorded immediately after adding varying concentrations of H$_2$O$_2$. The arrow indicates the increase of H$_2$O$_2$ concentration. (c) Absorbance monitoring of 5 μM OleT$_{SA}$ treated with 2 mM H$_2$O$_2$ from 20 s to 60 min. The arrow indicates the increase of incubation time. (d) The UV-Vis spectra of 5 μM OleT$_{SA}$ was recorded after treating with varying concentrations of H$_2$O$_2$ for 15 min. (f) The UV-Vis spectra of 5 μM OleT$_{SA}$ was recorded after treating with varying concentrations of H$_2$O$_2$ for 30 min. Protein aggregation was observed with high concentration of H$_2$O$_2$ treatment and longer time incubation, which causes high scattering.
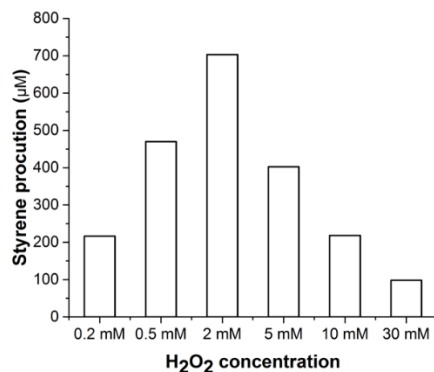
**Figure 2.4** $H_2O_2$ concentration dependence test for OleT$_{SA}$ catalysis with hydrocinnamic acid. Reaction condition: OleT$_{SA}$ 5 μM, hydrocinnamic acid 4 mM, reaction at room temperature for 60 minutes.

The destruction of the heme group of P450s and unspecific peroxygenases by $H_2O_2$ or other reactive intermediates such as superoxide anion ($O_2^-$) and hydroxyl radical ($^{\bullet}OH$) has been widely reported.[29,51,31] Because the intact heme has prominent optical features, heme degradation can be easily monitored by the loss of these features.[31] In the low-spin ferric resting state, the most intense optical peak of P450s is the Soret band, which is centered at 418 nm for substrate-free low-spin OleT$_{SA}$.[22,24] As shown in **Figure 2.3b**, upon the injection of increasing concentrations of $H_2O_2$ from 0.05 mM to 40 mM, the Soret band absorption of OleT$_{SA}$ decreases, implying heme destruction with $H_2O_2$ treatment. More serious heme bleaching and protein precipitation occurs upon longer incubation with high concentration of $H_2O_2$ (**Figure 2.3d** and **2.3e**). Even with 2 mM $H_2O_2$, a condition in which the enzyme shows maximized conversion rate (**Figure 2.2a**), significant heme bleaching can be observed over time in **Figure 2.3c**. These results suggest that heme destruction is a key factor that limits OleT$_{SA}$ catalysis, and thus maintaining a compatible $H_2O_2$ concentration during the reaction could potentially improve OleT$_{SA}$ catalytic efficiency. Slow $H_2O_2$ perfusion or fed-batch method have been used to circumvent the heme issue.[41,23]

41

In this contribution, we propose to use a GOx enzyme-based *in situ* $H_2O_2$-generating method to leverage $OleT_{SA}$ catalysis.

## 2.3.2 EFFECT OF DIFFERENT GOX SUBSTRATES ON THE ENZYME CASCADE CATALYSIS

It has been reported that GOx not only efficiently oxidizes D-glucose but also consumes different sugars including D-mannose, D-galactose and D-xylose among others with slower reaction rates,[47,48,52] which provides a useful method to tune the rate of $H_2O_2$-generation to better optimize OleT catalysis. To maximize the potential of a multi-enzyme system, kinetic matching of each enzymatic reaction is important.[53–55] In order to optimize the stoichiometry of GOx and $OleT_{SA}$ in the tandem catalysis reaction, different concentrations of GOx were tested with fixed concentrations of $OleT_{SA}$ and varying sugar substrates. As shown in **Figure 2.5a**, with glucose as a substrate, 10 nM GOx (0.002 molar equivalents to $OleT_{SA}$) leads to maximized substrate conversion. Upon further increasing the GOx concentration, the product yield decreased, which could be caused by enzyme inactivation due to excess $H_2O_2$ produced from the GOx/glucose reaction. When mannose or galactose was used, at least one molar equivalent of GOx to $OleT_{SA}$ was needed to maximize the conversion rate. A similar phenomenon was observed in the assay where hydrocinnamic acid was metabolized by $OleT_{SA}$ to produce styrene (**Figure 2.6**). However, it is noteworthy that upon increasing the mannose concentration up to 13 mM, styrene production continued to rise (a ~30-50% increase, depending on the different GOx concentration) (**Figure 2.6 inset**).

42
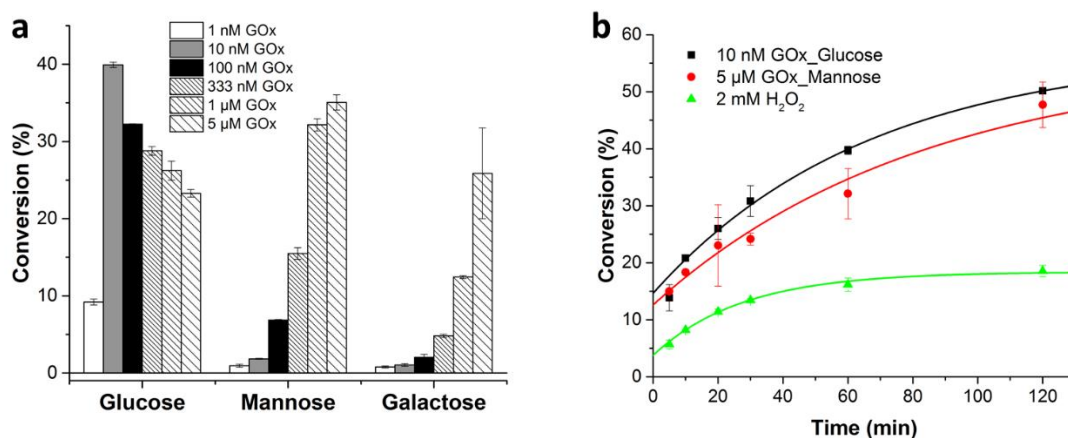
**Figure 2.5** OleT$_{SA}$ catalysis can be driven by different sugars with optimized GOx enzyme concentration. (a) Comparison of the conversion of eicosanoic acid with the OleT$_{SA}$/GOx catalysis in a 60 min reaction time. (b) A time course comparison with GOx_Glucose and GOx_Mannose as H$_2$O$_2$ source vs. direct addition of H$_2$O$_2$ (2 mM). An exponential model was used to fit the data in (b). Reaction conditions were as follows: OleT$_{SA}$ 5 μM, sugars 6.6 mM, eicosanoic acid 1 mM, GOx (concentrations as indicated) at room temperature. Error bars indicate the standard deviation of duplicate experiments (n = 2).

A typical time course of product formation with the optimized GOx/OleT ratio is shown in **Figure 2.3b**. Decarboxylation continues to proceed until the end of the test (2 hours) in the GOx method, demonstrating clear advantages of enzyme utility by comparing with that in the H$_2$O$_2$ method. As a control, a glucose titration test with GOx method shows increasing OleT$_{SA}$ activity with increasing glucose concentration, while with H$_2$O$_2$ method, glucose had no such effect, indicating that the enhancement of activity by glucose only occurs when paired with GOx (**Figure 2.7**). It is apparent that controlling the *in situ* H$_2$O$_2$-generation rate to maintain an appropriate H$_2$O$_2$ level during OleT$_{SA}$ catalysis is important to maximize its enzymatic conversion. In summary, the GOx method shows significantly improved OleT$_{SA}$ catalytic efficiency than the H$_2$O$_2$ method, while GOx enzyme pairing with different sugars makes the method flexible to leverage OleT enzyme catalysis. Based on this, we demonstrated the kinetic matching of the tandem catalysis may be an important parameter to optimize the enzyme cascade efficiency.

### 2.3.3. GOX/OLET$_{SA}$ ENZYME CASCADE CATALYSIS TEST WITH DIFFERENT FATTY ACIDS

Abundant and bioavailable fatty acids provide a renewable source for the sustainable production of terminal alkenes. To improve conversion yield has been a major pursuit for the OleT enzyme's application.[14,44] Here, we tested the GOx/OleT$_{SA}$ enzyme cascade activity with a selection of fatty acids including eicosanoic acid, stearic acid, palmitic acid, myristic acid and lauric acid using glucose as a GOx substrate at the optimized condition (molar ratio of GOx:OleT$_{SA}$ = 1:500) as described above. By comparison to the one-time $H_2O_2$ injection method, GOx method exhibits 25% to 300% higher conversion of substrate to product depending on the fatty acid substrate used (**Table 2.1**). The chemo-specificity of enzymatic catalysis was similar in both two methods of peroxide addition (**Table 2.2**). In addition, with long-term reactions, the GOx method showed further increased substrates conversion, while there was no improvement with time in the $H_2O_2$ method (**Table 2.3**), which supports our hypothesis the function of OleT$_{SA}$ is irreversibly hampered by a high-volume addition of $H_2O_2$. By comparing different methods used for the OleT enzymatic reaction reported in literature so far, our method provides a simple and efficient way to improve the enzyme catalysis (**Table 2.4**).
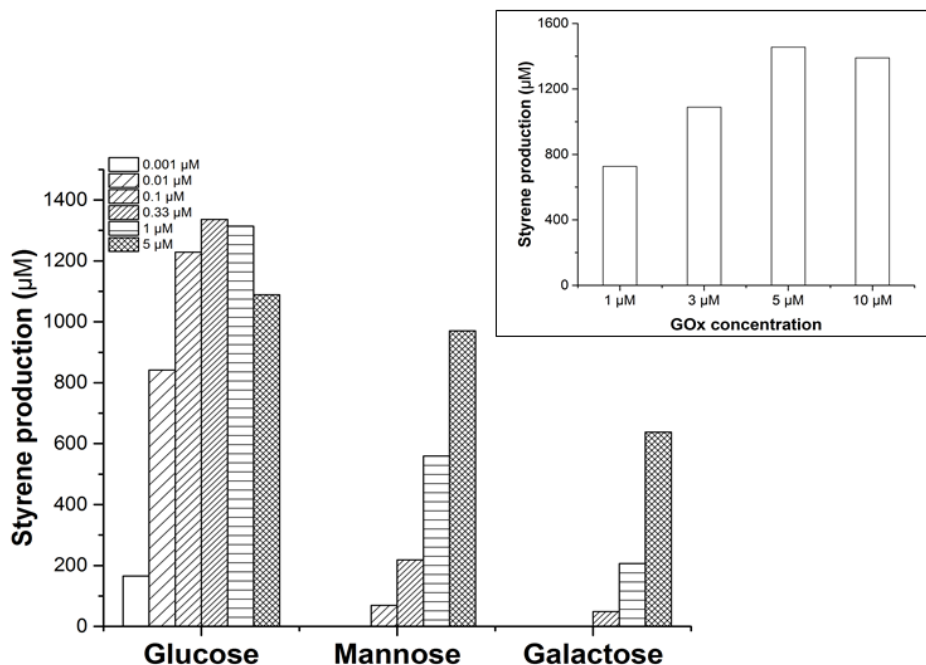
**Figure 2.6** OleT$_{SA}$ catalysis can be driven by different sugars in presence of different concentration of GOx enzyme. Reaction condition: OleT$_{SA}$ 5 μM, sugars 6.6 mM, hydrocinnamic acid 4 mM, room temperature for 60 minutes. 2 mM $H_2O_2$ was used in the $H_2O_2$ method as control. Inset: GOx titration test with 13 mM mannose and 4 mM hydrocinnamic acid at room temperature for 60 minutes.
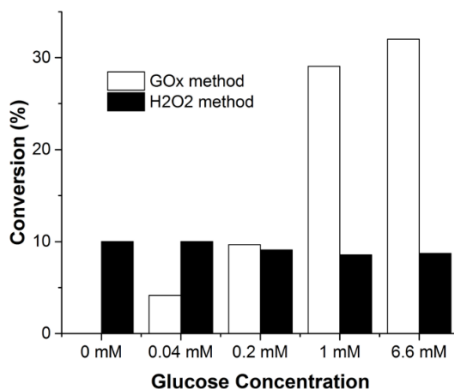


**Figure 2.7** Glucose titration with GOx method. Reaction condition: OleT$_{SA}$ 5 μM, eicosanoic acid 1mM at room temperature, 30 minutes. Same operation was done with $H_2O_2$ method to exclude the glucose effect on the enzyme activity.

45

**Table 2.1** OleT$_{SA}$ metabolic profile with different FAs with either the GOx or H$_2$O$_2$ method.

| Substrate | Method | Alkene (%) | Alcohol (%) | Conv. (%) |
|---|---|---|---|---|
| eicosanoic acid* | GOx | >99 | NA | 50 ± 5 |
| | H$_2$O$_2$ | >99 | NA | 12 ± 2 |
| stearic acid* | GOx | >99 | <1 | 71 ± 3 |
| | H$_2$O$_2$ | >99 | <1 | 57 ± 1 |
| palmitic acid | GOx | 62 | 38 | 93 ± 7 |
| | H$_2$O$_2$ | 49 | 51 | 23 ± 4 |
| myristic acid | GOx | 63 | 37 | 99 ± 3 |
| | H$_2$O$_2$ | 60 | 40 | 75 ± 5 |
| lauric acid | GOx | 59 | 41 | 92 ± 7 |
| | H$_2$O$_2$ | 50 | 50 | 71 ± 5 |

Reaction conditions are as follows: 5 μM OleT$_{SA}$, 0.5 mM fatty acid substrate, and either 0.01 μM GOx with 6.6 mM glucose or 2 mM H$_2$O$_2$. The reaction was in a total volume of 300 μL and carried out at room temperature for 60 min. *The C20 and C18 fatty acid was dissolved in 70% ethanol/30% triton-100 as stock. All other fatty acids were dissolved in DMSO as stock.

**Table 2.2** OleT$_{SA}$ metabolized alcohol products profile comparison with the GOx method[a] and H$_2$O$_2$ method[b] [22]

| Substrate | Method | Alcohol (%) |
|---|---|---|
| eicosanoic acid | GOx | NA |
| | H$_2$O$_2$ | NA |
| stearic acid | GOx | <1% |
| | H$_2$O$_2$ | <1% |
| palmitic acid | GOx | 8% α, 63% β, 29% γ |
| | H$_2$O$_2$ | 3% α, 97% β, NA γ |
| myristic acid | GOx | 26% α, 75% β, γ NA |
| | H$_2$O$_2$ | 19% α, 81% β, γ NA |
| lauric acid | GOx | 11% α, 73% β, 16% γ |
| | H$_2$O$_2$ | 4% α, 96% β, γ NA |

[a] **Reaction condition:** OleT$_{SA}$ 5 μM, FAs 500 μM, 10 nM GOx, 6.6 mM glucose for 1 hour. Alcohol products distribution was calculated based on the according peak areas.
[b] **Reaction condition:** OleT$_{SA}$ 5 μM, FAs 500 μM. 5 mM H$_2$O$_2$ was perfused with pump within 2 hours. The Cβ regiospecificity is defined as the fractional percentage of alkenes and Cβ-alcohols over total products formed by the enzyme.

**Table 2.3** OleT$_{SA}$ metabolism profile with different FAs with GOx and H$_2$O$_2$ method for overnight reactions

| Substrate | Method | Alkene (%) | Alcohol (%) | Conv. (%) |
|---|---|---|---|---|
| eicosanoic acid[*] | GOx | >99% | NA | >99% |
| | H$_2$O$_2$ | >99% | NA | 13 ± 4 |
| stearic acid | GOx | >99% | <1% | 35 ± 2 |
| | H$_2$O$_2$ | >99% | <1% | 3 ± 1[*] |
| palmitic acid | GOx | 63 | 37 | 94 ± 3 |
| | H$_2$O$_2$ | 41 | 59 | 35 ± 1 |
| myristic acid | GOx | 79 | 21 | >99% |
| | H$_2$O$_2$ | 60 | 40 | 81 ± 3 |
| lauric acid | GOx | 74 | 26 | >99% |
| | H$_2$O$_2$ | 47 | 53 | 75 ± 13 |

Condition: OleT$_{SA}$ 5 µM, substrate 0.5 mM, GOx 0.01 µM, glucose 6.6 mM or H$_2$O$_2$ 2 mM, 300 µL reaction at room temperature for overnight. * The C20 fatty acid was dissolved in 70% ethanol/30% triton-100 as stock. All other fatty acids were dissolved in DMSO as stock.

48

**Table 2.4** Comparison of the catalytic efficiency GOx/OleT$_{SA}$ enzyme cascade and other reported systems

| Entry | Enzyme | Enzyme [μM]/ Substrate [mM] | Method/ Electron source | Reaction conditions | Turnover number (TON) | Ref. |
|---|---|---|---|---|---|---|
| 1 | OleT$_{JE}$ | 5/0.5 (C14:0) | OleT-AldO fusion/glycerol | RT, 20 min | 95 | 38 |
| 2 | OleT$_{JE}$ | 2/0.5 (C20:0) | light-driven | 25 °C, 2 h | 25 | 39 |
| 3 | OleT$_{JE}$ | 3/1 (C20:0) | OleT-BM3R/NADPH | RT, 12 h | 233 | 14 |
| 4 | OleT$_{JE}$ | 1.5/5 (C18:0) | OleT/FDH-CamAB/ NADPH | RT, 170 rpm, 24 h | 2096 | 15 |
| 5 | OleT$_{JE}$ | 1/0.5 (C20:0) | H$_2$O$_2$ perfusion | RT, 1 h | 280 | 18 |
| 6 | OleT$_{SA}$ | 5/0.5 (C14:0) | H$_2$O$_2$ fed-batch | 30 °C, 12 h | 94 | 20 |
| 7 | OleT$_{SA}$ | 5/1 (C20:0) | OleT/GOx cascade/glucose | RT, 2 h | 96 | This study |
| 8 | OleT$_{SA}$ | 1/1 (C20:0) | OleT/GOx cascade/glucose | RT, 12 h | 410 | This study |

In entry 3 and 4, a dehydrogenase-based NADPH regeneration system was coupled. In entry 8, the molar ratio of OleT to GOx was kept as 500:1.

### 2.3.4. HEME DESTRUCTION IS PREVENTED USING THE GOX METHOD OF H$_2$O$_2$ ADDITION

The improved OleT$_{SA}$ enzyme catalytic activity with GOx method was attributed to a gradual and robust production of H$_2$O$_2$ that prevents heme degradation during the tandem catalysis. To confirm this hypothesis, OleT$_{SA}$ spectra were monitored during the enzymatic reactions with either one-time H$_2$O$_2$ addition or the gradual introduction using GOx (**Figure 2.8a and 2.8b**). The Soret peak was used as a handle for monitoring heme

integrity. As expected, OleT$_{SA}$ enzyme shifts from the high-spin (substrate-bound) state to the low-spin (substrate-free/product-bound) state spontaneously upon treatment with 2 mM H$_2$O$_2$, and stays predominantly in this state for the remainder of the time course test. We have previously determined in OleT$_{JE}$ that product release is significantly slower than the chemical steps (e.g. H$_2$O$_2$ activation, C-H abstraction) that lead to alkene generation,[56] consistent with the spectra obtained here. Within minutes, the heme chromophore bleaches during the H$_2$O$_2$ treatment. On the other hand, with the GOx method, the low-spin Soret maximum at 418 nm appears after 5 min of reaction, indicating most of the proteins are substrate-free/product-bound like that of the H$_2$O$_2$ method, which suggests there is a burst of H$_2$O$_2$ during this period. Then, the enzyme returns to predominantly high-spin state for the remainder of the assay. This indicates that the majority of the OleT$_{SA}$ is in the substrate-bound state and that H$_2$O$_2$ production by GOx is now rate-limiting. And the sluggishness of peroxide generation protects the heme from H$_2$O$_2$-mediated degradation to afford the higher overall turnover numbers shown above. As quantitative confirmation, the Soret peak intensity (as the sum of high-spin and low-spin) was used to determine the fraction of active enzyme throughout the time course study. As shown in **Figure 2.8c**, more than half of enzyme was inactivated within 1 h in the H$_2$O$_2$ method, whereas with the GOx method, the amount of active OleT$_{SA}$ enzyme remained unchanged after 1 hour, which is consistent with the observation that OleT$_{SA}$ is continually active during this time period (Figure 2.5b).
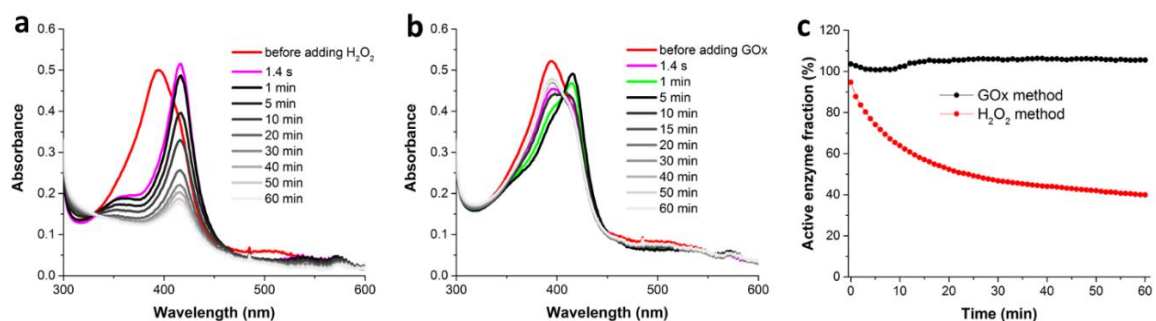
**Figure 2.8** Soret band monitoring during OleT$_{SA}$ catalytic reactions with H$_2$O$_2$ method (a) and GOx method (b). In all reactions, 5 μM OleT$_{SA}$, 0.5 mM eicosanoic acid, 2 mM H$_2$O$_2$ or 10 nM GOx, 6.6 mM glucose were used. (c) Active OleT$_{SA}$ enzyme fraction comparison during the catalytic reactions with GOx and H$_2$O$_2$ methods.

## 2.3.5. POLYMER-GOX-OLET$_{SA}$ ASSEMBLY TO IMPROVE ENZYME CASCADE CATALYTIC EFFICIENCY

Inspired by natural multienzyme complexes that exhibit extraordinary efficiency,[57,58] a variety of enzyme cascades have recently been developed via co-localization of enzymes on nanostructured scaffolds[59–67] to enable cooperative catalytic mechanisms such as facilitating intermediate transportation,[59,60] kinetic modification via enzyme or intermediate substrate scaffold interactions,[59,63] stoichiometry optimization,[61] and encapsulation,[65,66] etc. We therefore attempted to co-assemble GOx/OleT$_{SA}$ enzyme pairs on a polymeric support to further promote enzymatic catalysis. In our previous studies, we used P4VP and other polymers to co-assemble different proteins to generate core-shell nanoparticles (NPs) [48,64,65,66] and demonstrated a high protein loading capacity and a close proximity of proteins on the surface of the NPs.[49,71] Both the fine balance between hydrophobicity and hydrophilicity as well as the hydrogen bonding between proteins and polymers provide a benign environment for proteins to maintain their functions. Herein, we use this strategy to co-assemble GOx and OleT$_{SA}$ enzymes (**Figure 2.9a**) in order to improve the enzyme cascade catalytic efficiency. With the assumption that the two enzymes have equal chance to attach to the NPs surface, equal molar

51

concentration of GOx and OleT$_{SA}$ (1 μM/each enzyme) was used for the co-assembly. TEM and DLS analysis shows successfully assembled polymer-dual-enzymes NP$_S$ with an average size of ~385 nm (**Figure 2.9c**). For tandem catalytic reactions, mannose was fed, hydrocinnamic acid or myristic acid was used as an OleT$_{SA}$ substrate to compare the activity of the assemblies to enzymes in solution. As shown in **Figure 2.9d** and **Figure 2.10**, P4VP-GOx-OleT$_{SA}$ assemblies exhibit around 35-40% higher activity than the free GOx/OleT$_{SA}$ in a 60-min reaction at room temperature with different OleT$_{SA}$ substrates.

As a control, the mixture of P4VP-GOx and P4VP-OleT$_{SA}$ assemblies showed comparable activity with the free enzymes (**Figure 2.9d**). Moreover, with dilutions, the co-assembled samples showed further enhanced activity compared to the free enzymes (~ 60% enhanced activity was observed with 5 × times dilution of each sample, **Figure 2.11**). These results suggest that improved activity of the co-assemblies is related to the closed space of enzymes because of the co-localization on the NPs. In addition, if H$_2$O$_2$ instead of mannose was used to drive the catalysis, P4VP-GOx-OleT$_{SA}$ did not exhibit any enhanced activity comparing to the free enzymes (**Figure 2.12**).
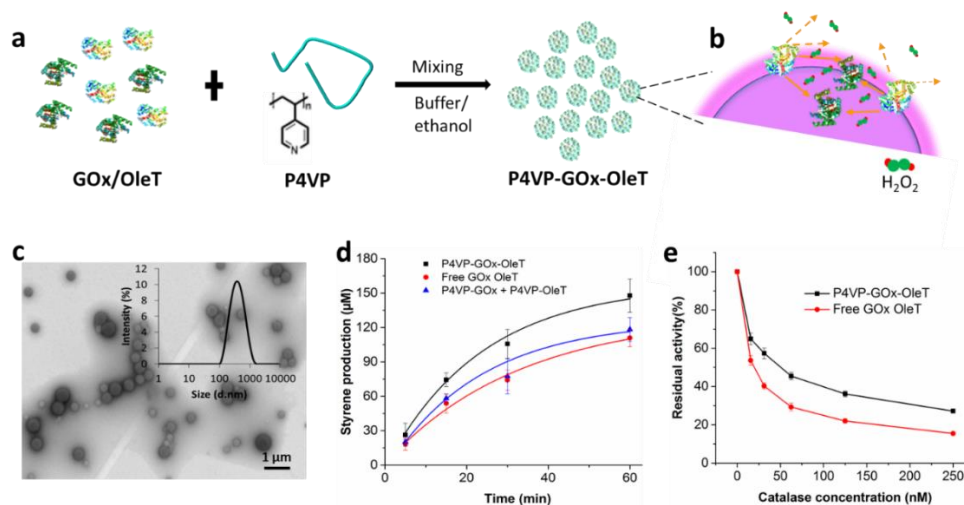
**Figure 2.9** (a) Schematic illustration of the preparation of P4VP-GOx-OleT$_{SA}$ in buffer/ethanol co-solvent. (b) Model of H$_2$O$_2$ diffusion on the surface of P4VP-GOx-OleT$_{SA}$ assemblies. The pink color represents hydration layer on the NPs surface. (c) TEM image of P4VP-GOx-OleT$_{SA}$ assemblies; inset: DLS analysis shows the size distribution of P4VP-GOx-OleT$_{SA}$ assemblies. (d) P4VP-GOx-OleT$_{SA}$ assemblies show enhanced activity than free enzyme cascade for styrene production with 6.6 mM mannose as sugar source, and 2 mM hydrocinnamic acid as the substrate. An exponential model was used to fit the data. (e) Inhibition effect of catalase on the reactions catalyzed by P4VP-GOx-OleT$_{SA}$ and free GOx/OleT$_{SA}$ mixtures. The reaction condition was the same as in (d) and were quenched after 60 minutes' incubation. Error bars indicate the standard deviation of duplicate experiments (n = 2).
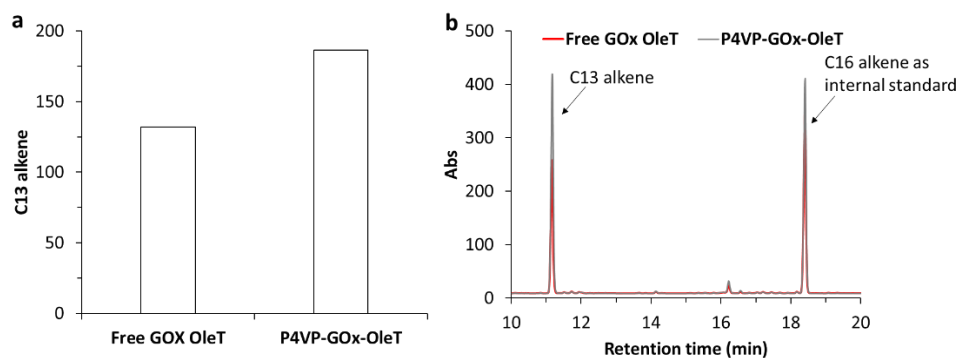


**Figure 2.10** (a) P4VP-GOx-OleT$_{SA}$ assemblies show enhanced activity than free enzyme cascade for C13 alkene production. Myristic acid (1 mM) was used as the substrate and mannose (6.6 mM) was fed in the reaction. (b) GC spectrum of the activity comparison. C16 alkene (150 μM) was used as internal standard at 18.4 min.

53
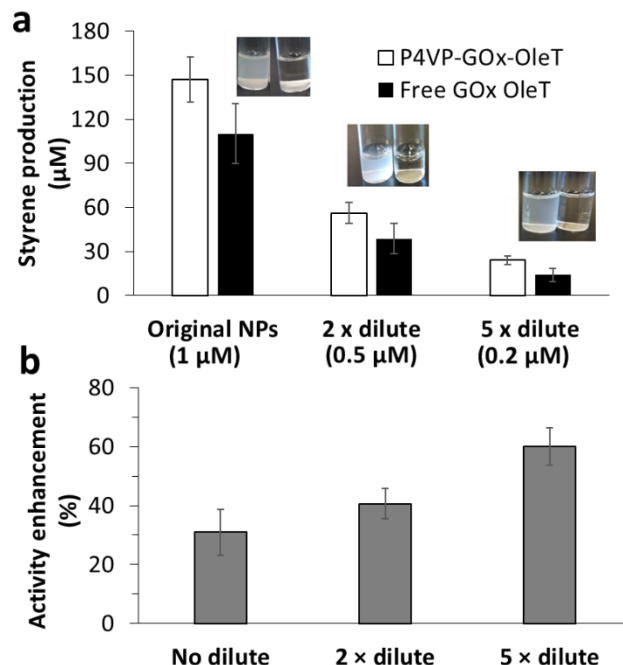
**Figure 2.11** Activity enhancement was enlarged with dilution of P4VP-GOx-OleT$_{SA}$ NPs and free GOx/OleT$_{SA}$ solution. (a) Styrene production test of the samples with different dilutions. Condition: GOx and OleT$_{SA}$ (1 μM/each), hydrocinnamic acid (2 mM), Mannose (6.6 mM) in 500 μL reactions were used for all samples. 0.2 mg/mL P4VP was used for the co-assembly. Inset: the pictures of P4VP-GOx-OleT$_{SA}$ samples with different dilutions. The clean tubes contain free enzymes reactions. The cloudy tubes contain P4VP-GOx-OleT$_{SA}$ assemblies catalyzed reactions. The pictures were taken after the 2 hours' reaction at RT. (b) Activity comparison of P4VP-GOx-OleT$_{SA}$ samples and free GOx/OleT$_{SA}$ samples with different dilutions.
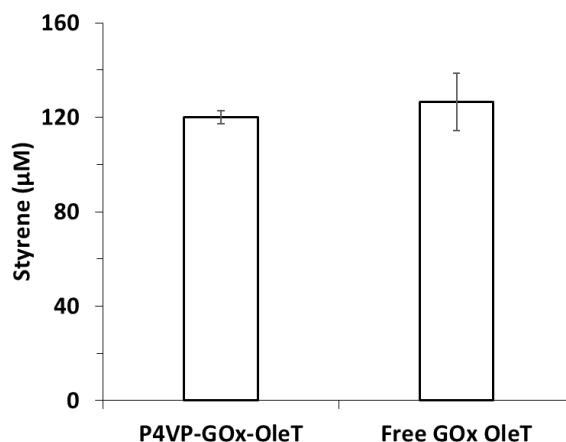


**Figure 2.12** Activity comparison of P4VP-GOx-OleT$_{SA}$ assemblies and free enzyme cascade with H$_2$O$_2$ method. hydrocinnamic acid (4 mM) was used as substrate. H$_2$O$_2$ (2 mM) was used with 30 minutes' reaction. Error bars indicate the standard deviation of duplicate experiments (n =2).

54

To further confirm whether the activity enhancement is due to proximity effects, catalase, a scavenger of $H_2O_2$, was added to challenge the tandem catalysis. As shown in **Figure 2.9e**, the reactions catalyzed by P4VP-GOx-OleT$_{SA}$ was much less inhibited by catalase than that of free enzymes. For example, when 250 nM of catalase was included in the reactions, P4VP-GOx-OleT$_{SA}$ still showed ~30% activity, while only 15% activity was observed for free enzymes. This result suggests that on the surface of NP assemblies, some $H_2O_2$ produced by GOx is transferred to OleT$_{SA}$ directly and is not freely defused into the bulk solution due to the closed proximity of the enzymes. We rationalize that in this system, large amount of enzyme pairs assembled on the nanoparticles surface may provide multiple local targets for $H_2O_2$.[72,73] Moreover, the very closed distance of the enzymes may create a hydration layer[74] on the surface of NPs, which facilitates $H_2O_2$ transportation among enzymes,[59] making a high local concentration of $H_2O_2$ around the OleT$_{SA}$ enzymes. All these factors may contribute to the enhanced GOx/OleT$_{SA}$ enzymatic activity when adhered to NP surfaces. However, the modest activity improvement and the slight sensitivity to catalase suggest the assembly is unable to directly tunnel $H_2O_2$ (Figure 2.9b), which could be the reason why only a relatively weak enhancement compared to other encapsulation systems.[65,75] Nevertheless, the combination of the GOx-driven OleT$_{SA}$ catalysis and the co-localization of the enzyme pairs on polymeric NPs through co-assembly demonstrated an efficient way to improve the cascade enzymatic catalysis.

## 2.4. CONCLUSION

In this study, we report the use of a GOx enzyme-based *in situ* $H_2O_2$-generating method to drive OleT$_{SA}$ catalysis to produce terminal alkenes with significantly improved substrate conversion than the one-time addition of peroxide. By monitoring the heme using

UV-visible spectroscopy during the reaction, we confirmed that the enhancement was due to the minimized heme degradation in the GOx method. By adjusting the GOx/OleT$_{SA}$ molar ratio and using different sugars, our system provides a flexible method to tune the H$_2$O$_2$-generating process and thus to leverage the catalysis of OleT$_{SA}$. In particular, when glucose is used, only 0.002 molar equivalents of GOx are required to efficiently drive OleT$_{SA}$ catalysis. This not only demonstrates a simple approach to improve the isolated OleT enzyme catalysis *in vitro* but also provides new perspective for alkene production *in vivo*.[76–78] With this enzyme cascade model, a facile P4VP polymer-dual enzyme co-assembly was developed to further optimize the enzyme cascade catalytic efficiency through enzyme co-localization. Overall, the GOx-based *in situ* H$_2$O$_2$-generation method with OleT$_{SA}$ represents a simple and efficient strategy to transform bioavailable feed stocks such as fatty acids to industrially important chemicals.

## 2.5 REFERENCES

(1)     Corma, A.; Iborra, S.; Velty, A. Chemical Routes for the Transformation of Biomass into Chemicals. *Chem. Rev.* **2007**, *107* (6), 2411–2502.

(2)     Sheldon, R. A. Green and Sustainable Manufacture of Chemicals from Biomass: State of the Art. *Green Chem.* **2014**, *16* (3), 950–963.

(3)     Potocnik, J. Renewable Energy Sources and the Realities of Setting an Energy Agenda. *Science* **2007**, *315* (5813), 810–811.

(4)     Demirbas, A. Political, Economic and Environmental Impacts of Biofuels: A Review. *Appl. Energy* **2009**, *86*, S108–S117.

(5)     Bulushev, D. A.; Ross, J. R. H. Catalysis for Conversion of Biomass to Fuels via Pyrolysis and Gasification: A Review. *Catal. Today* **2011**, *171* (1), 1–13.

(6)     Peralta-Yahya, P. P.; Zhang, F.; del Cardayre, S. B.; Keasling, J. D. Microbial Engineering for the Production of Advanced Biofuels. *Nature* **2012**, *488* (7411), 320–328.

(7)     Ray, S.; Rao, P. V. C.; Choudary, N. V. Poly-α-Olefin-Based Synthetic Lubricants: A Short Review on Various Synthetic Routes. *Lubr. Sci.* **2012**, *24* (1), 23–44.

(8)     Lane, B. S.; Burgess, K. A Cheap, Catalytic, Scalable, and Environmentally Benign Method for Alkene Epoxidations. *J. Am. Chem. Soc.* **2001**, *123* (12), 2933–2934.

(9)     Skupinska, Jadwiga. Oligomerization of Alpha-Olefins to Higher Oligomers. *Chem. Rev.* **1991**, *91* (4), 613–648.

(10)     Aransiola, E. F.; Ojumu, T. V.; Oyekola, O. O.; Madzimbamuto, T. F.; Ikhu-Omoregbe, D. I. O. A Review of Current Technology for Biodiesel Production: State of the Art. *Biomass Bioenergy* **2014**, *61*, 276–297.

(11)     Das, S.; Join, B.; Junge, K.; Beller, M. A General and Selective Copper-Catalyzed Reduction of Secondary Amides. *Chem. Commun.* **2012**, *48* (21), 2683–2685.

(12)     Das, S.; Möller, K.; Junge, K.; Beller, M. Zinc-Catalyzed Chemoselective Reduction of Esters to Alcohols. *Chem. – Eur. J.* **2011**, *17* (27), 7414–7417.

(13)     Dennig, A.; Kurakin, S.; Kuhn, M.; Dordic, A.; Hall, M.; Faber, K. Enzymatic Oxidative Tandem Decarboxylation of Dioic Acids to Terminal Dienes. *Eur. J. Org. Chem.* **2016**, *2016* (21), 3473–3477.

(14)     Lu, C.; Shen, F.; Wang, S.; Wang, Y.; Liu, J.; Bai, W.-J.; Wang, X. An Engineered Self-Sufficient Biocatalyst Enables Scalable Production of Linear α-Olefins from Carboxylic Acids. *ACS Catal.* **2018**, *8* (7), 5794–5798.

(15)     Dennig, A.; Kuhn, M.; Tassoti, S.; Thiessenhusen, A.; Gilch, S.; Bülter, T.; Haas, T.; Hall, M.; Faber, K. Oxidative Decarboxylation of Short-Chain Fatty Acids to 1-Alkenes. *Angew. Chem. Int. Ed.* **2015**, *54* (30), 8819–8822.

(16)     Rude, M. A.; Baron, T. S.; Brubaker, S.; Alibhai, M.; Cardayre, S. B. D.; Schirmer, A. Terminal Olefin (1-Alkene) Biosynthesis by a Novel P450 Fatty Acid Decarboxylase from Jeotgalicoccus Species. *Appl Env. Microbiol* **2011**, *77* (5), 1718–1727.

(17)     Belcher, J.; McLean, K. J.; Matthews, S.; Woodward, L. S.; Fisher, K.; Rigby, S. E. J.; Nelson, D. R.; Potts, D.; Baynham, M. T.; Parker, D. A.; et al. Structure and Biochemical Properties of the Alkene Producing Cytochrome P450 OleTJE (CYP152L1) from the *Jeotgalicoccus Sp.* 8456 Bacterium. *J. Biol. Chem.* **2014**, *289* (10), 6535–6550.

(18)     Grant, J. L.; Hsieh, C. H.; Makris, T. M. Decarboxylation of Fatty Acids to Terminal Alkenes by Cytochrome P450 Compound I. *J. Am. Chem. Soc.* **2015**, *137* (15), 4940–4943.

(19)     Bakkes, P. J.; Riehm, J. L.; Sagadin, T.; Rühlmann, A.; Schubert, P.; Biemann, S.; Girhard, M.; Hutter, C. M.; Bernhardt, R.; Urlacher, B.V.; Engineering of versatile redox partner fusions that support monooxygenase activity of functionally diverse cytochrome P450s. *Sci. Rep.* **2017**; *7,* 9570–9583.

(20)     Wise, C. E.; Hsieh, C. H.; Poplin, N. L.; Makris, T. M. Dioxygen Activation by the Biofuel-Generating Cytochrome P450 OleT. *ACS Catal.* **2018**, *8* (10), 9342–9352.

(21)     Joo, H.; Lin, Z.; Arnold, F. H. Laboratory Evolution of Peroxide-Mediated Cytochrome P450 Hydroxylation. *Nature* **1999**, *399* (6737), 670–673.

(22)     Amaya, J. Mechanisms of Decarboxylation In The CYP152 Family Of Cytochrome P450S. *Theses Diss.* **2018**.

(23)     Jiang, Y.; Li, Z.; Wang, C.; Zhou, Y. J.; Xu, H.; Li, S. Biochemical Characterization of Three New α-Olefin-Producing P450 Fatty Acid Decarboxylases with a Halophilic Property. *Biotechnol. Biofuels* **2019**, *12* (1), 79–93.

(24)     Munro, A. W.; McLean, K. J.; Grant, J. L.; Makris, T. M. Structure and Function of the Cytochrome P450 Peroxygenase Enzymes. *Biochem. Soc. Trans.* **2018**, *46* (1), 183–196.

(25)     Grant, J. L.; Mitchell, M. E.; Makris, T. M. Catalytic Strategy for Carbon−carbon Bond Scission by the Cytochrome P450 OleT. *Proc. Natl. Acad. Sci.* **2016**, *113* (36), 10049–10054.

(26)     Burek, B. O.; Bormann, S.; Hollmann, F.; Bloh, J. Z.; Holtmann, D. Hydrogen Peroxide Driven Biocatalysis. *Green Chem.* **2019**, *21* (12), 3232–3249.

(27)     Stadtman, E. R.; Levine, R. L. Free Radical-Mediated Oxidation of Free Amino Acids and Amino Acid Residues in Proteins. *Amino Acids* **2003**, *25* (3–4), 207–218.

(28)     Ogola, H. J. O.; Hashimoto, N.; Miyabe, S.; Ashida, H.; Ishikawa, T.; Shibata, H.; Sawa, Y. Enhancement of Hydrogen Peroxide Stability of a Novel Anabaena Sp. DyP-Type Peroxidase by Site-Directed Mutagenesis of Methionine Residues. *Appl. Microbiol. Biotechnol.* **2010**, *87* (5), 1727–1736.

(29)     Vidal-Limón, A.; Águila, S.; Ayala, M.; Batista, C. V.; Vazquez-Duhalt, R. Peroxidase Activity Stabilization of Cytochrome P450BM3 by Rational Analysis of Intramolecular Electron Transfer. *J. Inorg. Biochem.* **2013**, *122*, 18–26.

(30)     Ayala, M.; Batista, C. V.; Vazquez-Duhalt, R. Heme Destruction, the Main Molecular Event during the Peroxide-Mediated Inactivation of Chloroperoxidase from Caldariomyces Fumago. *J. Biol. Inorg. Chem. JBIC Publ. Soc. Biol. Inorg. Chem.* **2011**, *16* (1), 63–68.

(31)    Karich, A.; Scheibner, K.; Ullrich, R.; Hofrichter, M. Exploring the Catalase Activity of Unspecific Peroxygenases and the Mechanism of Peroxide-Dependent Heme Destruction. *J. Mol. Catal. B Enzym.* **2016**, *134*, 238–246.

(32)    Zhou, P.; Lan, D.; Popowicz, G. M.; Wang, X.; Yang, B.; Wang, Y. Enhancing H2O2 Resistance of an Esterase from Pyrobaculum Calidifontis by Structure-Guided Engineering of the Substrate Binding Site. *Appl. Microbiol. Biotechnol.* **2017**, *101* (14), 5689–5697.

(33)    Opperman, D. J.; Reetz, M. T. Towards Practical Baeyer–Villiger-Monooxygenases: Design of Cyclohexanone Monooxygenase Mutants with Enhanced Oxidative Stability. *ChemBioChem* **2010**, *11* (18), 2589–2596.

(34)    Omura, K.; Aiba, Y.; Onoda, H.; Stanfield, J. K.; Ariyasu, S.; Sugimoto, H.; Shiro, Y.; Shoji, O.; Watanabe, Y. Reconstitution of Full-Length P450BM3 with an Artificial Metal Complex by Utilising the Transpeptidase Sortase A. *Chem. Commun.* **2018**, *54* (57), 7892–7895.

(35)    Markiton, M.; Boncel, S.; Janas, D.; Chrobok, A. Highly Active Nanobiocatalyst from Lipase Noncovalently Immobilized on Multiwalled Carbon Nanotubes for Baeyer–Villiger Synthesis of Lactones. *ACS Sustain. Chem. Eng.* **2017**, *5* (2), 1685–1691.

(36)    Hernandez, K.; Fernandez-Lafuente, R. Lipase B from Candida Antarctica Immobilized on Octadecyl Sepabeads: A Very Stable Biocatalyst in the Presence of Hydrogen Peroxide. *Process Biochem.* **2011**, *46* (4), 873–878.

(37)    Gao, F.; Jiang, Y.; Hu, M.; Li, S.; Zhai, Q. Bienzymatic Nanoreactors Composed of Chloroperoxidase–Glucose Oxidase on Au@Fe3O4 Nanoparticles: Dependence of Catalytic Performance on the Bioarchitecture. *Mater. Des.* **2016**, *111*, 414–420.

(38)    Deurzen, M. P. J. V.; Seelbach, K.; Rantwijk, F. van; Kragl, U.; Sheldon, R. A. Chloroperoxidase: Use of a Hydrogen Peroxide-Stat for Controlling Reactions and Improving Enzyme Performance. *Biocatal. Biotransformation* **1997**, *15* (1), 1–16.

(39)    Hagström, A. E. V.; Törnvall, U.; Nordblad, M.; Hatti-Kaul, R.; Woodley, J. M. Chemo-Enzymatic Epoxidation–Process Options for Improving Biocatalytic Productivity. *Biotechnol. Prog.* **2011**, *27* (1), 67–76.

(40)    Hernandez, K.; Berenguer-Murcia, A.; Rodrigues, R.; Fernandez-Lafuente. Hydrogen Peroxide in Biocatalysis. A Dangerous Liaison. *Curr. Org. Chem.* **2012**, *16*, 2652–2672.

59

(41)     Amaya, J. A.; Rutland, C. D.; Makris, T. M. Mixed Regiospecificity Compromises Alkene Synthesis by a Cytochrome P450 Peroxygenase from Methylobacterium Populi. *J. Inorg. Biochem.* **2016**, *158*, 11–16.

(42)     Zachos, I.; Gaßmeyer, S. K.; Bauer, D.; Sieber, V.; Hollmann, F.; Kourist, R. Photobiocatalytic Decarboxylation for Olefin Synthesis. *Chem. Commun.* **2015**, *51* (10), 1918–1921.

(43)     Köninger, K.; Grote, M.; Zachos, I.; Hollmann, F.; Kourist, R. Light-Driven Enzymatic Decarboxylation. *J. Vis. Exp.* **2016**, (111), e53439.

(44)     Matthews, S.; Tee, K. L.; Rattray, N. J.; McLean, K. J.; Leys, D.; Parker, D. A.; Blankley, R. T.; Munro, A. W. Production of Alkenes and Novel Secondary Products by P450 OleTJE Using Novel H2 O2 -Generating Fusion Protein Systems. *FEBS Lett.* **2017**, *591* (5), 737–750.

(45)     Wilson, R.; Turner, A. P. F. Glucose Oxidase: An Ideal Enzyme. *Biosens. Bioelectron.* **1992**, *7* (3), 165–185.

(46)     Bankar, S. B.; Bule, M. V.; Singhal, R. S.; Ananthanarayan, L. Glucose Oxidase — An Overview. *Biotechnol. Adv.* **2009**, *27* (4), 489–501.

(47)     Adams, E. C.; Mast, R. L.; Free, A. H. Specificity of Glucose Oxidase. *Arch. Biochem. Biophys.* **1960**, *91* (2), 230–234.

(48)     Gibson, Q. H.; Swoboda, B. E.; Massey, V. KINETICS AND MECHANISM OF ACTION OF GLUCOSE OXIDASE. *J. Biol. Chem.* **1964**, *239*, 3927–3934.

(49)     Suthiwangcharoen, N.; Li, T.; Wu, L.; Reno, H. B.; Thompson, P.; Wang, Q. Facile Co-Assembly Process to Generate Core–Shell Nanoparticles with Functional Protein Corona. *Biomacromolecules* **2014**, *15* (3), 948–956.

(50)     Rude, M. A.; Baron, T. S.; Brubaker, S.; Alibhai, M.; Cardayre, S. B. D.; Schirmer, A. Terminal Olefin (1-Alkene) Biosynthesis by a Novel P450 Fatty Acid Decarboxylase from Jeotgalicoccus Species. *Appl Env. Microbiol* **2011**, *77* (5), 1718–1727.

(51)     Karuzina, I. I.; Archakov, A. I. Hydrogen Peroxide-Mediated Inactivation of Microsomal Cytochrome P450 during Monooxygenase Reactions. *Free Radic. Biol. Med.* **1994**, *17* (6), 557–567.

(52)     Singh, J.; Verma, N. S. Glucose Oxidase from Aspergillus Niger: Production, Characterization and Immobilization for Glucose Oxidation; *Adv Appl Sci Res* **2013**, *4* (3), 250–257.

(53)    Dvorak, P.; Kurumbang, N. P.; Bendl, J.; Brezovsky, J.; Prokop, Z.; Damborsky, J. Maximizing the Efficiency of Multienzyme Process by Stoichiometry Optimization. *ChemBioChem* **2014**, *15* (13), 1891–1895.

(54)    Zhang, Y.; Lyu, F.; Ge, J.; Liu, Z. Ink-Jet Printing an Optimal Multi-Enzyme System. *Chem. Commun.* **2014**, *50* (85), 12919–12922.

(55)    Zhang, Y.; Ge, J.; Liu, Z. Enhanced Activity of Immobilized or Chemically Modified Enzymes. *ACS Catal.* **2015**, *5* (8), 4503–4513.

(56)    Amaya, J. A.; Rutland, C. D.; Leschinsky, N.; Makris, T. M. A Distal Loop Controls Product Release and Chemo- and Regioselectivity in Cytochrome P450 Decarboxylases. *Biochemistry* **2018**, *57* (3), 344–353.

(57)    Rhee, S.; Parris, K. D.; Ahmed, S. A.; Miles, E. W.; Davies, D. R. Exchange of K+ or Cs+ for Na+ Induces Local and Long-Range Changes in the Three-Dimensional Structure of the Tryptophan Synthase A2β2 Complex. *Biochemistry* **1996**, *35* (13), 4211–4221.

(58)    Liang, P.-H.; Anderson, K. S. Substrate Channeling and Domain−Domain Interactions in Bifunctional Thymidylate Synthase−Dihydrofolate Reductase. *Biochemistry* **1998**, *37* (35), 12195–12205.

(59)    Fu, J.; Liu, M.; Liu, Y.; Woodbury, N. W.; Yan, H. Interenzyme Substrate Diffusion for an Enzyme Cascade Organized on Spatially Addressable DNA Nanostructures. *J. Am. Chem. Soc.* **2012**, *134* (12), 5516–5519.

(60)    Haga, T.; Hirakawa, H.; Nagamune, T. Artificial Self-Sufficient Cytochrome P450 Containing Multiple Auxiliary Proteins Demonstrates Improved Monooxygenase Activity. *Biotechnol. J.* **2018**, *13* (12), 1800088.

(61)    Dueber, J. E.; Wu, G. C.; Malmirchegini, G. R.; Moon, T. S.; Petzold, C. J.; Ullal, A. V.; Prather, K. L. J.; Keasling, J. D. Synthetic Protein Scaffolds Provide Modular Control over Metabolic Flux. *Nat. Biotechnol.* **2009**, *27* (8), 753–759.

(62)    Chen, R.; Chen, Q.; Kim, H.; Siu, K.-H.; Sun, Q.; Tsai, S.-L.; Chen, W. Biomolecular Scaffolds for Enhanced Signaling and Catalytic Efficiency. *Curr. Opin. Biotechnol.* **2014**, *28*, 59–68.

(63)    Sandanaraj, B. S.; Vutukuri, D. R.; Simard, J. M.; Klaikherd, A.; Hong, R.; Rotello, V. M.; Thayumanavan, S. Noncovalent Modification of Chymotrypsin Surface Using an Amphiphilic Polymer Scaffold: Implications in Modulating Protein Function. *J. Am. Chem. Soc.* **2005**, *127* (30), 10693–10698.

(64)     Delebecque, C. J.; Lindner, A. B.; Silver, P. A.; Aldaye, F. A. Organization of Intracellular Reactions with Rationally Designed RNA Assemblies. *Science* **2011**, *333* (6041), 470–474.

(65)     Chen, W.-H.; Vázquez-González, M.; Zoabi, A.; Abu-Reziq, R.; Willner, I. Biocatalytic Cascades Driven by Enzymes Encapsulated in Metal–Organic Framework Nanoparticles. *Nat. Catal.* **2018**, *1* (9), 689–695

(66)     Zhang, X.; Hou, Y.; Ettelaie, R.; Guan, R.; Zhang, M.; Zhang, Y.; Yang, H. Pickering Emulsion-Derived Liquid–Solid Hybrid Catalyst for Bridging Homogeneous and Heterogeneous Catalysis. *J. Am. Chem. Soc.* **2019**, *141* (13), 5220–5230.

(67)     Xu, Y.; Fei, J.; Li, G.; Yuan, T.; Xu, X.; Li, J. Nanozyme-Catalyzed Cascade Reactions for Mitochondria-Mimicking Oxidative Phosphorylation. *Angew. Chem. Int. Ed.* **2019**, *58* (17), 5572–5576.

(68)     Li, T.; Wu, L.; Suthiwangcharoen, N.; Bruckman, M. A.; Cash, D.; Hudson, J. S.; Ghoshroy, S.; Wang, Q. Controlled Assembly of Rodlike Viruses with Polymers. *Chem. Commun.* **2009**, *0* (20), 2869–2871.

(69)     Li, T.; Niu, Z.; Emrick, T.; Russell, T. P.; Wang, Q. Core/Shell Biocomposites from the Hierarchical Assembly of Bionanoparticles and Polymer. *Small* **2008**, *4* (10), 1624–1629.

(70)     Zhang, L.; Xu, Y.; Makris, T. M.; Wang, Q. Enhanced Arylamine N-Oxygenase Activity of Polymer–Enzyme Assemblies by Facilitating Electron-Transferring Efficiency. *Biomacromolecules* **2018**, *19* (3), 918–925.

(71)     Lu, L.; Zhang, L.; Yuan, L.; Zhu, T.; Chen, W.; Wang, G.; Wang, Q. Artificial Cellulosome Complex from the Self-Assembly of Ni-NTA-Functionalized Polymeric Micelles and Cellulases. *ChemBioChem* **2019**, *20* (11), 1394–1399.

(72)     Idan, O.; Hess, H. Diffusive Transport Phenomena in Artificial Enzyme Cascades on Scaffolds. *Nat. Nanotechnol.* **2012**, *7* (12), 769–770.

(73)     Idan, O.; Hess, H. Origins of Activity Enhancement in Enzyme Cascades on Scaffolds. *ACS Nano* **2013**, *7* (10), 8658–8665.

(74)     Bagchi, B. Water Dynamics in the Hydration Layer around Proteins and Micelles. *Chem. Rev.* **2005**, *105* (9), 3197–3219.

(75)     Tan, H.; Guo, S.; Dinh, N.-D.; Luo, R.; Jin, L.; Chen, C.-H. Heterogeneous Multi-Compartmental Hydrogel Particles as Synthetic Cells for Incompatible Tandem Reactions. *Nat. Commun.* **2017**, *8* (1), 1–10.

(76)    Dueber, J. E.; Wu, G. C.; Malmirchegini, G. R.; Moon, T. S.; Petzold, C. J.; Ullal, A. V.; Prather, K. L. J.; Keasling, J. D. Synthetic Protein Scaffolds Provide Modular Control over Metabolic Flux. *Nat. Biotechnol.* **2009**, *27* (8), 753–759.

(77)    Castellana, M.; Wilson, M. Z.; Xu, Y.; Joshi, P.; Cristea, I. M.; Rabinowitz, J. D.; Gitai, Z.; Wingreen, N. S. Enzyme Clustering Accelerates Processing of Intermediates through Metabolic Channeling. *Nat. Biotechnol.* **2014**, *32* (10), 1011–1018.

(78)    Wu, S.; Zhou, Y.; Gerngross, D.; Jeschek, M.; Ward, T. R. Chemo-Enzymatic Cascades to Produce Cycloalkenes from Bio-Based Resources. *Nat. Commun.* **2019**, *10* (1), 1–10.

CHAPTER 3

MICROFLUIDIC-ASSISTED POLYMER-PROTEIN ASSEMBLY TO FABRICATE

HOMOGENEOUS FUNCTIONAL NANOPARTICLES

## 3.1. INTRODUCTION

Polymeric nanoparticles (PNPs), because of their small size, high surface-area-to-volume ratio, and easy tunable physical and chemical properties, have gained great attentions in materials science.[1,2] Through chemical modification of polymer chains[3] or conjugation with distinct functional molecules ( e.g. inorganic or organic molecules, lipids, peptides, and proteins),[4–8] PNPs could be tailored with customized properties, and were found numerous applications in the fields of medicine,[9] bioimaging,[10] sensing[11,12] and catalysis.[13,14] Among them, the controlled assembly of polymers and/or proteins via supramolecular interactions offers unique opportunity in understanding the spontaneously self-organization process and fabrication of bioactive PNPs.[15–21] Currently PNPs are usually prepared using standard bulk reaction conditions,[22–26] which generally lead to large variability in their size distribution. In fact, it remains difficult to reproducibly synthesize batches of homogenous PNPs in bulk reactors, primarily due to the uncontrolled and insufficient mixing in addition to the uncontrolled residence time during the PNPs formation.[27] Therefore, methods that provide precise control of PNPs size distribution (for example, through microfluidics by optimizing mass transfer kinetics and diffusion rates, etc.) are of high interests.[28–30]

In our previous work, we systematically studied the co-assembly of poly(4-vinylpuridine) (P4VP) or other pyridine group grafted polymers with functional proteins to form core-shell PNPs.[21,31–34] The synthesis involved the mixing of polymer with protein in bulk reactors to form NPs intermediates, followed by dialysis or organic solvent evaporation for NPs maturation (**Figure 3.1a**). The assembly is primarily controlled by a kinetic process driven by the reduction of interfacial tension, i.e., the polymer forms

65

aggregates when experiencing non-solvents. After this nucleation step, proteins, acting as a surfactant-like role, are absorbed on the surface to stabilize the NPs. We hypothesize the protein is a relative slower step compared to the fast nucleation during the co-assembly. Both the fine balance between hydrophobicity and hydrophilicity as well as the hydrogen bonding between proteins and polymers are necessary for a successful co-assembly.[21] Nevertheless, because of the insufficient and less controllable mixing in bulk reactors, the polymer and polymer-protein particles experienced heterogeneous solvent environment during co-assembly, resulting in a broad size distribution of the NPs.[21,31,33]
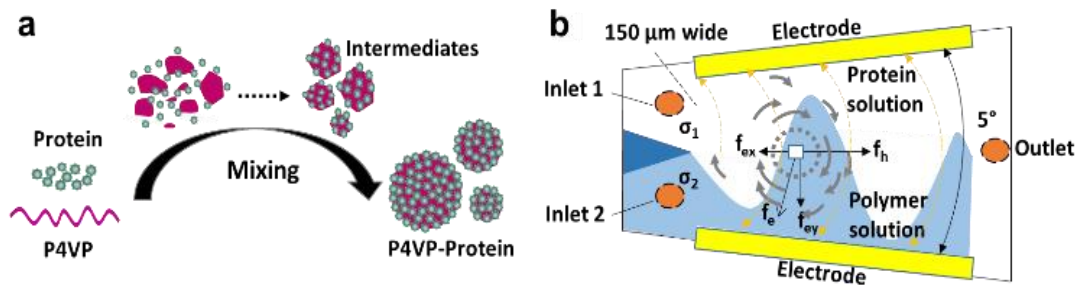


**Figure 3.1** (a) Schematic illustration of proposed polymer-protein co-assembly process. (b) Schematic illustration of the entrance of microchannel which is used for polymer protein co-assembly. The fluids with different electrical conductivity ($\sigma 1$ & $\sigma 2$) in the non-parallel microchannel are driven by the hydrodynamic force $f_h$ and the flow is excited by the electrical body force $f_e$ which can be divided into x-components $f_{ex}$ and y-component $f_{ey}$. $f_{ex}$ at different points along the electric line can be either negative or positive related to $f_h$. The large force in x-direction ($f_h + f_{ex}$) and y-direction $f_{ey}$ can generate a shear stress and produce a micro vertex,[38] resulting in ultrafast mixing.

Using microfluidics based microreactor to synthesize various functional nanoparticles has attracted attentions because of its unique advantages, such as controllable transportation at microscale, significantly reduced diffusion distance, etc.[35] With improved diffusion process *via* geometrical design, microfluidics based mixers have been used for synthetic purposes.[29,36,37] However, because normally Reynolds number is low in microfluidic devices, the flow is laminar and the corresponding mixing is conducted only through a molecular diffusion process, and thus is relatively slow and poor. For this reason,

66

Dr. Guiren Wang's group has developed a method to generate turbulent-like flows to create ultrafast mixing in microfluidic system under electrokinetics (EK) forcing,[38,39] which provides new opportunities for flow control and manipulation in microfluidics. In particular, it was found that rapid mixing could be achieved on both large and small scales in the majority of the microchannel under AC electric field.[38] For example, with a 20 $V_{p-p}$ voltage and 2 μL/min flow rate, 77% mixing can be reached within 5 milliseconds (ms),[40] which is much faster than other reported EK based micromixers.[41,42] Moreover, the mixing process could be easily controlled and fine-tuned by adjusting the AC electric fields (e.g. voltage, frequency, signal phase shift) and flow rates,[43] which makes it a superior technique than conventional geometry based micro mixers regarding to controllable mixing manipulation.

Herein, for the first time, we report the usage of this EK based microfluidic method (**Figure 3.1b**) to achieve polymer-protein co-assembly in order to fabricate homogeneous polymer-protein nanoparticles. Nanoparticle size is the result of two competing processes: drop breakage and coalescence after nucleation.[44] In our system, when protein stream and polymer dissolved ethanol stream meet in the microchannel, polymer droplets between the two phases of fluids will form at the initial stage and can then coalesce. The EK flow induced shear stress may breakup larger drops to generate smaller ones to increase interfacial area, and thus to enhance molecular mixing. The particle size distribution depends not only on the dispersive and continuous phase properties, the presence of surface-active agents, the type of surfactants, and the presence of electrolytes, but also on the overall flow velocity and concentration fields. Therefore, in this contribution, different proteins, flow rates and protein/polymer mass ratios were tested for the co-assembly *via*

67

fast mixing of micro fluids. We demonstrate that the polymer-protein NPs fabricated using our microfluidic method are highly uniform, the NPs size is tunable, and proteins' function is well retained. Because it is much easier to scale up by parallelization of multiple channels compared to the bulk method, this EK-based microfluidic method has unique advantages in its application for polymer protein co-assembly.

## 3.2. THEORY

The principle of generating chaotic EK flow and mixing is given below to illustrate qualitatively how the mixing is enhanced. There is an initial large electrical force that can overcome viscous force to generate strong chaotic flows. The Navier-Stokes equation with EK force can be described as

$$\rho(\partial u/\partial t + u \cdot \nabla u) = \nabla p + \mu \nabla^2 u + F_e \tag{1}$$

$$F_e = \rho_f E - \frac{1}{2}(E \cdot E)\nabla\varepsilon + \frac{1}{2}\nabla\left[\rho E \cdot E\left(\frac{\partial\varepsilon}{\partial\rho}\right)T\right] \tag{2}$$

$$\rho_f = \nabla \cdot (\varepsilon E) = \nabla\varepsilon \cdot E + \varepsilon\nabla \cdot E \tag{3}$$

where $\rho, u, p, \mu$ are the fluid density, flow velocity, pressure and dynamic viscosity respectively; $F_e$ is electrical body force, which consists of the Coulomb force (1st term), dielectric force (2nd term) and thermal expansion (3rd term) respectively in Eq. (2); $E$ is electric field, $\rho_f$ is the free volume charge density; $\varepsilon$ and $\sigma$ are the electric permittivity and conductivity of the electrolyte respectively, and $T$ indicates temperature. For incompressible fluids, the third term can generally be ignored.[45] In addition, for a given fluid, $\varepsilon$ mainly depends on $T$. On the one hand, as the two initial streams with different conductivity $\sigma$ meet together, the interface between the two streams can be assumed to be frozen within a very short distance before the electrokinetic flow starts to develop. On the

68

other hand, the bulk flow and the generated strong mixing will also transfer potential heat caused by Joule heating to downstream and to the good heat conductive metal walls. Therefore, $T$ variation due to electrothermal effects could be insignificant. Thus $\varepsilon$ is assumed to be uniform in the flow, $\partial \varepsilon / \partial t \approx 0$ and $\nabla \varepsilon \approx 0$. So the second term force in Eq. (2) is also negligible. Then we have

$$F_e = \rho_f E \qquad (4)$$

The transport equation of $\rho_f$ for a bipolar system is: [45]

$$\frac{\partial \rho_f}{\partial t} + u \cdot \nabla \rho_f + \nabla \cdot (\sigma E) = \left(\frac{D_+ - D_-}{m_+ + m_-}\right) \nabla^2 \sigma + \left(\frac{D_+ m_+ + D_- m_-}{m_+ + m_-}\right) \nabla^2 \rho_f \qquad (5)$$

where $\sigma$ is the conductivity of the fluid, $m_+$ and $m_-$ and $D_+$ and $D_-$ are the mobility and diffusivity of positive and negative charges respectively. Since in liquid, Schmidt number is usually very large, to simplify the process to illustrate the major physics, the diffusion term can be negligible. Because of the large conductivity different between the two streams, $E$ will generate $\rho_f$ near the interface, and the transport of $\rho_f$ is primarily dominated by $E$, and thus, the convection $u$ is relatively negligible. Then Eq. (5) can be simplified as:

$$\partial \rho_f / \partial t + \nabla \cdot (\sigma E) = 0 \qquad (6)$$

Note although based on electro neutrality assumption, which is often adopted for transport phenomena in electrolyte, $\nabla \cdot (\sigma E) = 0$, such an approximation is not applicable here, not only because the well-known reasons described by Probstein,[46] but also because of the $\rho_f$ created at the interface with a large difference in the conductivity between the two streams

69

as shown in Fig 3.1b. Near the interface, $\rho_f$ should not be zero, as $E$ has also a large difference at the interface between the initial two streams. The large difference in $E$ is due to the difference in $\sigma$, which in turn generates $\rho_f$ under local $E$. Substitution of Eq. (3) into (6), yields:

$$\nabla \cdot E \approx -\left(\nabla\sigma \cdot E + \varepsilon\nabla \cdot \frac{\partial E}{\partial t}\right)/\sigma \qquad (7)$$

Substituting Eq. (7) back into Eq. (4) and (3), we find that the initial $F_e$ can be approximately determined by:

$$F_e = -\varepsilon\frac{\boldsymbol{\nabla\sigma \cdot E}}{\sigma}E - \frac{\varepsilon^2}{\sigma}\left(\nabla \cdot \frac{\partial E}{\partial t}\right)E \qquad (8)$$

Here the first term of Eq. (8) is consistent with the result in DC case,[47] the second term is related to the initial $F_e$ due to AC $E$. However, in practice, to satisfy quasi-electrostatic condition, normally

$$\varepsilon_{ref}\omega < \sigma_1 < \sigma_2 - \sigma_1 \qquad (9)$$

where σ1 and σ2 are σ of the stream 1 and 2 respectively. Then the 2nd term of Eq. (8) should be much smaller than the 1st term and can be neglected. We have

$$F_e = -\varepsilon\frac{\boldsymbol{\nabla\sigma \cdot E}}{\sigma}E \qquad (10)$$

Eq. (10) indicates that $F_e$ increases with increasing $\nabla\sigma$ and $E$, and parallelizing them. Initially, at a large scale where the influence of fluid viscosity is small, $F_e$ directly drives and causes strong chaotic EK flow. The order of the corresponding velocity can be reached by balancing the inertial term and $F_e$ in Eq. (1) as

$$U_e = \sqrt{\varepsilon_{ref}(\sigma_2 - \sigma_1)\,E_0^2/\,\rho\sigma_1} \qquad (11)$$

70

At a specific length scale $l$, where the time scale of convection under forcing ($\tau_e = l/U_e$) is equal to the corresponding viscous diffusion time scale ($\tau_d = \rho l^2/\mu$), a nominal length scale in the EK flow can be qualitatively concluded:

$$l_{ed} = \sqrt{\mu^2\sigma_1/\rho\varepsilon_{ref}E_0^2(\sigma_2 - \sigma_1)} = \sqrt{w^2/Gr_e} \qquad (12)$$

$$Gr_e = (U_c l/v)^2 = \rho\varepsilon_{ref}w^2E_0^2(\sigma_2 - \sigma_1)/\sigma_1\mu^2 \qquad (13)$$

where $Gr_e$ is the nominal electric Grashof number. To describe the electrical conductivity field in Eq (10), we need transport equation for conductivity. For a bipolar system uniform $\varepsilon$, if there are neither production nor consumption of charges, the transport equation for conductivity is: (Melcher 1981, page 5.33) [48]

$$\frac{\partial\sigma}{\partial t} + u \cdot \nabla\sigma = -E \cdot \nabla\left[(m_+ - m_-)\sigma + m_+m_-\rho_f\right] - \left[(m - m_-)\sigma + m_+m_-\rho_f\right]\frac{\rho_f}{\varepsilon} +$$

$$D_e\nabla^2\sigma + \frac{m_+m_-}{m_++m_-}(D_+ - D_-)\nabla^2\rho_f \qquad (14)$$

$$D_e = \frac{D_+m_+ + D_-m_-}{m_++m_-} \qquad (15)$$

where $D_e$ is an effective diffusivity. The concentration of the protein and polymer is important for the nanoparticle synthesis. The protein in the solution is charged, but the polymer is not. Ignoring the chemical reaction, the transport equation of their concentration can be described as (Truskey et al. page 362):[49]

$$\frac{\partial c_i}{\partial t} + u \cdot \nabla c_i = D_{mi}\nabla^2 c_i \qquad (16)$$

$$D_{mi} = \frac{(z_+ - z_-)D_+D_-}{(z_+D_+ - z_-D_-)} \qquad (17)$$

71

where $c_i$ is concentration of each component i, i.e. either polymer or protein, $z_-$ and $z_+$ are the charge valance of protein and ions. For polymer $D_{mi}$ is its own diffusivity, but for protein, $D_{mi}$ is given in Eq. (17), where ions in buffer balance the charge of the protein. Let $u = U_c\hat{u}, t = \tau\hat{t},\ x = U_c\tau\hat{x},\ \nabla = \hat{\nabla}/U_c\tau,\ \sigma = \sigma_0\hat{\sigma},\ E = E_0\hat{E},\ p = \rho U_c^2,\ \varepsilon = \varepsilon_{ref}\hat{\varepsilon},$ $c = c_0\hat{c}, \rho_f = \varepsilon E_0\widehat{\rho}_f/U_c\tau$, we get the dimensionless form of Eqs (1), (15) and (16) as

$$\left(\frac{\partial\hat{u}}{\partial\hat{t}} + \hat{u}\cdot\hat{\nabla}\hat{u}\right) + \hat{\nabla}\hat{p} + \frac{(\hat{\nabla}\hat{\sigma}\cdot\hat{E})}{\hat{\sigma}}\hat{E} = \frac{1}{\sqrt{Gr_e}}\hat{\nabla}^2\hat{u} \qquad (18)$$

$$\frac{\partial\hat{\sigma}}{\partial\hat{t}} + \hat{u}\cdot\hat{\nabla}\hat{\sigma} = \frac{R_{e,mig}}{\sqrt{Gr_e}}\left(\frac{m_+ - m_-}{m_+ + m_-}\right)\left(\hat{E}\cdot\hat{\nabla}\hat{\sigma} + \hat{\sigma}\widehat{\rho}_f\right) + \frac{\tau_r R_{e,mig}^2}{\tau_d\sqrt{Gr_e}}\left(\frac{m_+ m_-}{(m_+ + m_-)^2}\right)\left(\hat{E}\cdot\hat{\nabla}\widehat{\rho}_f + \widehat{\rho}_f^2\right) +$$

$$\frac{1}{Sc_e\sqrt{Gr_e}}\hat{\nabla}^2\hat{\sigma} + \frac{\tau_r R_{e,mig}}{\tau_D\sqrt{Gr_e}}\left(\frac{m_+ m_-}{(m_+ + m_-)^2}\right)\hat{\nabla}^2\widehat{\rho}_f \qquad (19)$$

$$\frac{\partial\widehat{c_i}}{\partial\hat{t}} + \hat{u}\cdot\hat{\nabla}\widehat{c_i} = \frac{1}{Sc_{mi}\sqrt{Gr_e}}\hat{\nabla}^2\widehat{c_i} \qquad (20)$$

where $\hat{u}$, $\hat{x}$, $\hat{\nabla}$ and $\hat{E}$, $\hat{\sigma}$, and $\widehat{\rho}_f$ are dimensionless functions of $u$, $x$, $\nabla$, $E$, $\sigma$ and $\rho_f$ respectively; $\sigma_0 = \sigma_2 - \sigma_1$ is the initial characteristic $\sigma$ of the flow; $E_0 = V_f/\sqrt{2}w$ represents the nominal $E$ across the channel width $w$ (where $V_f$ is the applied peak-to-peak voltage between two electrodes. $w$ is the width of the channel at the entrance.). $\varepsilon_{ref}$ is the $\varepsilon$ of water at a reference T; $Sc_e = \mu/\rho D_e$ and $Sc_{mi} = \mu/\rho D_{mi}$ are Schmidt number of effective ions and component i respectively; $\tau_r = \varepsilon/\sigma_0$ is charge relaxation time, $R_{e,mig} = lE_0(m_+ + m_-)/v$ is charge migration Reynolds number, and $\tau_D = l^2/(D_+ - D_-)$ is a charge diffusion time respectively.

If $Gr_e$ is sufficiently high, e.g. by increasing initial$(\sigma_2 - \sigma_1)$, the diffusion terms of the right side in Eq. (18), (19) and (20) become approximately negligible. Both conductivity and concentration will be dispersed by $U_e$ and chaotic EK flow without smearing in the entire transverse direction. This can even enhance $F_e$ and thus, mixing at small scale to generate homogeneous $c_i$. By increasing the initial $\sigma_2/\sigma_1$, $E_0$ and parallelizing $\nabla\sigma$ and $E$, $Gr_e$ can be enhanced.

## 3.3. EXPERIMENTAL DETAILS

### 3.3.1. MICROCHANNEL FABRICATION

The design and fabrication of the microchannel is shown in **Figure 3.2** in supporting information. A quasi T-shaped microchannel was made of acrylic plates, gold chips, Teflon™ PFA membrane, Teflon™ PTFE sheets and gasket by lamination-based microfabrication.[38] Gold chips were used as electrodes to make the two electrically conductive channel sidewalls. Teflon™ PFA membranes were used to avoid the channel clogging problems caused by the high stickiness of polymer, which has been one of the major obstacles in microfluidic nanomaterials synthesis.[50] A Teflon™ PTFE splitter plate was used to separate the two steams initially till they meet in the microchannel and lead to a sharp interface with high conductivity gradient between the two streams, which can further enhance the mixing efficiency. The microchannel has a rectangular cross-section of 150 μm in width at the entrance and 230 μm in height, with the length of 5 mm. A small divergent angle of 5° was designed to maximize the mixing efficiency (**Figure 3.1b**, **3.2b**).[38] Rubbers were used to seal the channel. Because of the rapid polymer protein co-

73

assembly process under the ultrafast mixing, no significant polymer aggregates or other clotting issues were observed during the NPs fabrication with our microfluidic channel.
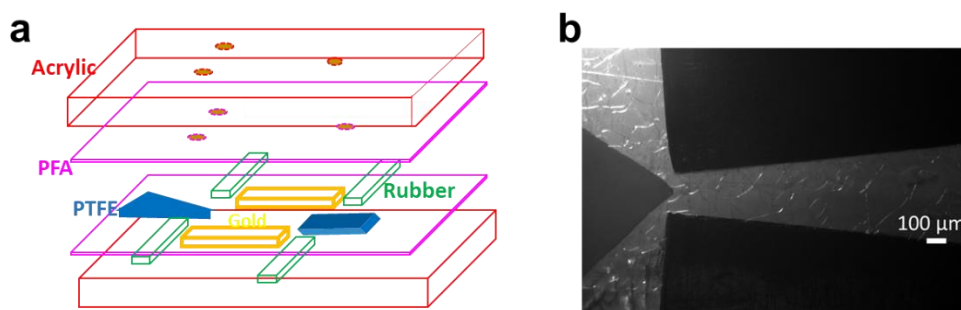


**Figure 3.2** Schematic of the microchannel design and fabrication (a) and the image of microchannel near the entrance (b).

3.3.2. MATERIALS

Teflon™ PFA membrane, Teflon™ PTFE sheets were purchased from Cshyde. Gold chips were purchased from Surepure Chemetals. Fluorescein sodium salt, P4VP (Mw 60000), *p*-aminophenol (*p*AP, >99.0%) were purchased from Sigma-Aldrich. Phenazine methosulfate (PMS, >98.0%) was purchased from TCI America. NADH sodium salt was purchased from EMD Millipore. Unless otherwise noted, all chemicals and solvents used were of analytical grade and were used as received from commercial sources. Water (18.2 MΩ) was obtained from Milli-Q system (Millipore). The proteins used in this work include bovine serum albumin (BSA) (MW: 66 kDa, pI: 4.7), fluorescent protein EGFP (MW: 27 kDa, pI:5.6) fluorescent protein mCherry (Mw: 29 kDa, pI: 5.6), N-oxygenase CmlI (Mw: 38 kDa, pI: 5.0). BSA was purchased from Sigma-Aldrich. All other proteins were expressed in E. coli BL21 (DE3) in LB medium, and purified by nickel-nitriloacetic acid (Ni-NTA) affinity chromatography as described previously.[51,52]. PBS buffer

74

(NaCl 137 mM, KCl 2.7 mM, Na$_2$HPO$_4$ 10 mM, KH$_2$PO$_4$ 1.8 mM, pH 7.4) was used unless otherwise noted.

### 3.3.3. FLOW VISUALIZATION

The microchannel was placed on an inverted fluorescent microscope (Olympus-IX70). Solutions injection was done by a syringe pump (Harvard, Model PHD2000 Programmable) with different flow rates. AC electric power was supplied by a function generator (Tektronix, Model AFG3102). The visualization of the mixing process was conducted by Epi-fluorescence imaging technique.

### 3.3.4. POLYMER-PROTEIN CO-ASSEMBLY

For P4VP protein(s) co-assembly with microfluidic method, P4VP dissolved in ethanol and protein(s) dissolved in PBS were injected by two different size of syringes (1 mL vs 10 mL). The syringe pump was used to control flow rates. AC electric power was supplied by the function generator to provide electric field. 20 V$_{p-p}$ voltage, 20 kHz frequency, 180° phase shift were used unless otherwise noted. For P4VP-protein(s) co-assembly with conventional bulk method, 100 μL of P4VP dissolved in ethanol was added into a glass vial containing 1mL protein(s) dissolved in PBS buffer drop wisely during vigorous magnetic stirring. The concentration of P4VP and proteins solution was adjusted as the same among different methods. More than three batches of assembled samples were collected under each condition for characterization unless otherwise noted.

### 3.3.5. POLYMER-PROTEIN NPS CHARACTERIZATION

The hydrodynamic size distribution of nanoparticles was measured by Zetasizer (Nano ZS, Malvern Instruments). The mean value for the size based on the intensity, and the PDI, a dimensionless width parameter based on the cumulants analysis, were reported. For TEM analysis, the NPs samples were diluted 5 times by DI water, 20 µL diluted sample was dropped onto 250-mesh carbon-coated copper grids. The grids were dried, washed once by DI water and observed with a Hitachi H-8000 electron microscope. NPs size and size distribution based on TEM images were analyzed by ImageJ software.

For protein (BSA as the model protein) loading efficiency characterization, the NPs samples were centrifuged at 9 K rcf for 10 min at room temperature, the supernatants were collected for a standard Bradford assay. The loading efficiency on the NPs was calculated from the unbound proteins in the supernatant by subtracting the amount of the unbound proteins from the initial amount of proteins used.

For fluorescence imaging of polymer fluorescent protein(s) NPs, glass coverslips and plates were first soaked in a 10:1 (v:v) mixture of concentrated $H_2SO_4$ and 30% $H_2O_2$ overnight, extensively rinsed with water, sonicated in absolute ethanol for 10 mins and dried with air stream. The NPs samples after centrifuge were dispersed on the cleaned plates covered by a coverslip and sealed by nail polish oil. A self-assembled confocal microscope with an oil immersion, 60× NA1.4 and PlanApo objective lens (Olympus). A continuous wave laser (477 nm, 100 µW),

filter cubes/sets and a photomultiplier tube (PMT, HAMAMATSU, R-928) were used.

CmlI catalyzed reactions with *p*AP were measured by monitoring *p*-nitroso phenol (*p*NOP) product formation at an absorbance of 405 nm with a Molecular Device SPECTRAMax plus 384 with a microplate reader using 0.33 cm path length. Since CmlI enzyme is tolerant to ethanol,[51] no ethanol evaporation or dialysis was done for P4VP-CmlI NPs sample. Instead, the assembled samples were used for activity test directly without purification. For different samples, the same amount of free enzyme and the same percentage of ethanol (9.1%) were used.

### 3.3.6. CONDUCTIVITY AND VISCOSITY TEST

A conductivity meter (EXTECH ISTRUMENTS, ExStik II) was used for conductivity test. Viscosity was tested by Cannon-Ubbelohde Viscosity meter, #25.

### 3.4. RESULT AND DISCUSSION

### 3.4.1. MIXING VISUALIZATION

To demonstrate the EK-based fast mixing process, a modified quasi T-shaped microchannel was fabricated as shown in **Figure. 3.2**. Teflon materials were used to coat the inner faces of the microchannel in order to avoid the clotting problems. Firstly, fluorescein in PBS was mixed with deionized (DI) water using our microfluidic system. The conductivity ratio of these two streams was 5000:1. Different flow rates from 1 to 10 µL/min were tested (**Figure 3.3**). In the absence of electric field, laminar flows were formed in the microchannel, and only some diffusion could be observed with slower flow rate (**Figure 3.3a**). The boundary of the fluorescein solution and PBS solution was blurred with 1 µL/min flow rate and became much

clearer with higher flow rates ($\geq$2 $\mu$L/min, **Figure 3.3c**, **3.3e**, **3.3g**). While under electric field, chaotic flows were formed, which demonstrated dramatically enhanced mixing (**Figure 3.3b**, **3.3d**, **3.3f**, **3.3h**). Thus, significant increased diffusion is expected. A similar phenomenon was also observed with EGFP solution and polymer solution as injected as the two streams with ratio of ~ 6400: 1 (17260 $\mu$S/cm vs2.7 $\mu$S/cm) (**Figure 3.4**). Since the flow rate of EGFP solution was much larger than that of the polymer solution, EGFP solution occupied the most space of the channel and the boundary moved to the polymer side significantly. The boundary was still visible, although it was less clear. In the absence of electric field, the laminar flow pattern depends on the Peclet number (Pe), which is determined by the flow rate for certain micro flows, and the ratio of the flow rate of the two streams.[51,52] The larger the Pe, the clearer the boundary of the two streams. For flow rates of 1 $\mu$L/min (in **Figure. 3.4a**) or lower, the molecular diffusion in transverse direction becomes more important, and a less clear interface was seen. A clearer boundary was observed when higher flow rates ($\geq$2 $\mu$L/min) were used as shown in **Figure4c**, **4e**, **4g.** Considering the much higher viscosity of P4VP polymer solution than that of DI water (2.1 $mm^2$/s vs. 1.0 $mm^2$/s), we can conclude that the mixing under electric field is highly robust in this microfluidic channel. It is worthy to note that, with a 10 $\mu$L/min flow rate, highly homogeneous mixture of EGFP solution and P4VP solution can also be achieved at around 150 $\mu$m downstream of the entrance under electric field (**Figure 4.4h**), which implies a complete mixing starting from this position.
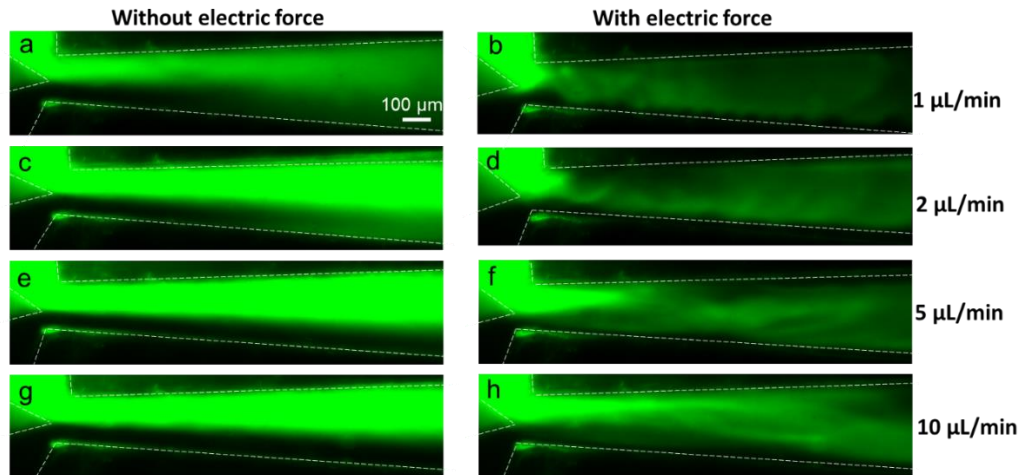
**Figure 3.3** Visualization of mixing process with fluorescein in PBS and DI water with different flow rate. **a**, **c**, **e**, **g**: laminar flow without electric field. **b**, **d**, **f**, **h**: chaotic flow with electric field. The top stream is dye solution; the bottom stream is DI water. Two 1 mL syringes were used for injection. 7 Vp-p is used. 20 Vp-p 20 kHz frequency, 180° phase shift are used. 0.015 s exposure is used during the imaging.
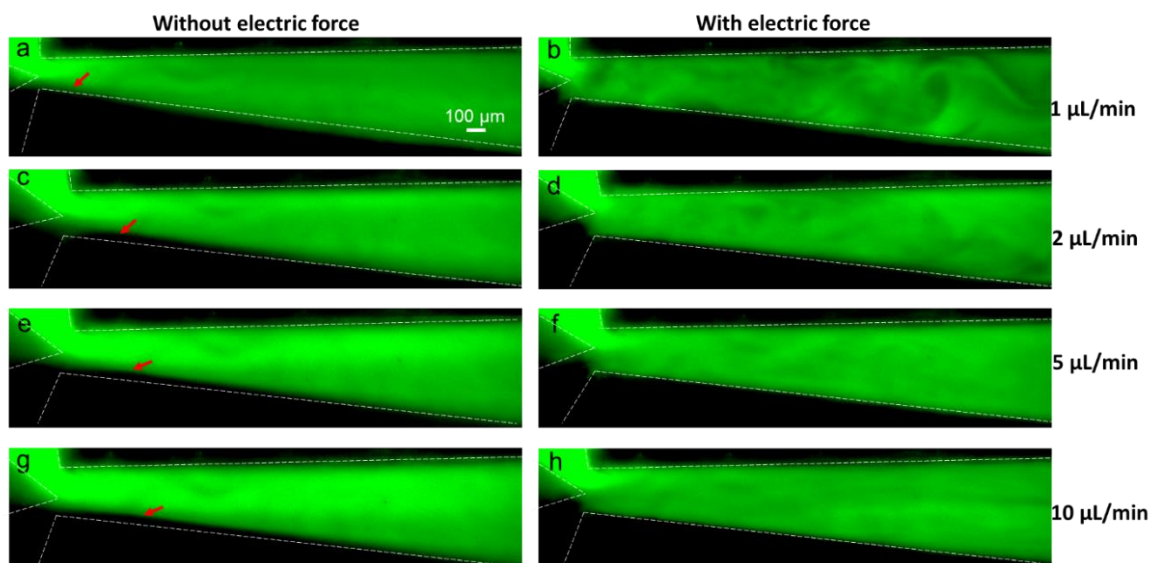


**Figure 3.4** Visualization of mixing process with EGFP protein in PBS and P4VP in ethanol with different flow rates. **a**, **c**, **e**, **g**: laminar flow without electric field. **b**, **d**, **f**, **h**: chaotic flow with electric field The top stream is EGFP solution, which is injected by 1 mL syringe. The bottom stream is P4VP solution, which is injected by 10 mL syringe. 20 Vp-p 20 kHz frequency, 180° phase shift are used. 0.015 s exposure is used during the imaging. The red arrows show the small fractions of polymer solution in the channel.

### 3.4.2. IMPROVED SIZE DISTRIBUTION OF POLYMER-PROTEIN NPS VIA MICROFLUIDIC METHOD

Firstly, BSA was used as a model protein to fabricate P4VP-protein NPs in this microfluidic method. Proteins were dissolved in PBS buffer (0.05 μg/μL), and P4VP was dissolved in ethanol (0.5 μg/μL). Flow rates 2 μL/min, 5 μL/min and 10 μL/min were tested while the electric field condition was kept the same. Mass ratio of P4VP to BSA was fixed as 1:1 (the volume ratio $V_{P4VP}:V_{BSA} = 10:1$). Transmission electron microscopy (TEM) and Dynamic light scattering (DLS) analysis shows that the size distribution of NPs produced by microfluidics is significantly improved by comparing with the samples from conventional bulk method (**Figure 3.5**). More TEM) images of NPs demonstrate further that highly homogeneous NPs can be fabricated by microfluidic method compared to the conventional bulk method ((**Figure 3.6**). Size distribution of NPs at different areas of TEM grids was analyzed (**Figure 3.6e**, **3.6j**, **3.6o**). With higher flow rates, the polydispersity index (PDI) of NPs is slightly increased, likely due to the reduced mixing in the channel. On the other hand, if there was no electric field applied, much larger and inhomogeneous NPs (average size as 680 to 770 nm depending on flow rates) were produced, and large amount of polymer aggregates could be observed under TEM (**Figure 3.7**). Within the enhanced chaotic flows, proteins and polymer precursors can be well mixed in a very short time by increased shear stress. We postulate that during the co-assembly in micro flows under an AC electric field, the size of NPs and local concentration of the starting materials in the mixture can be balanced. Thus, continuous aggregation of unassembled polymers is suppressed.

80

Additionally, the residence time distribution (RTD) of the assemblies is narrowed, which is ultimately responsible for the improved NPs' homogeneity.
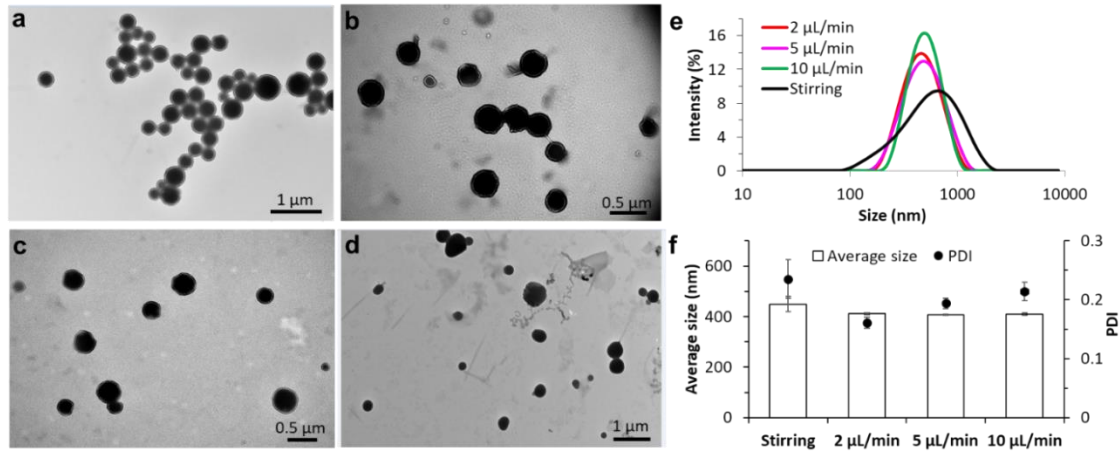


**Figure 3.5** Size and size distribution of P4VP-BSA NPs fabricated by microfluidics at different flow rates and conventional stirring method. (A-D): TEM image of nanoparticles by microfluidics with 2 μL/min (a), 5 μL/min (b), 10 μL/min (c) and stirring method (d). (e), (f): DLS analysis of nanoparticles by different methods. Final concertation of P4VP 0.05 mg/mL, BSA 0.05 mg/mL for all samples. Error bar stands for standard deviation of three replicates.
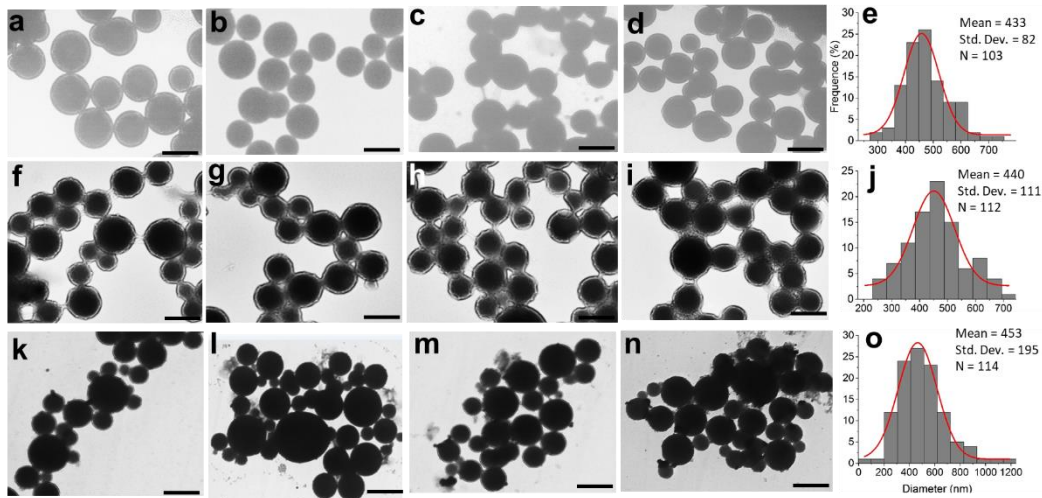


**Figure 3.6** Representative TEM images of P4VP-BSA nanoparticles fabricated by microfluidics with 2 μL/min (a-d), 10 μL/min (f-i) flow rates, and bulk method (k-n). Scale bars: 0.5 μm. (e, j, o) Statistical analysis of the NPs size and distribution. The red curves are Gaussian fits to the corresponding histograms. For all samples, 0.05 mg/mL P4VP and 0.05 mg/mL BSA were used as final concentration.

### 3.4.3 THE SIZE OF POLYMER-PROTEIN NPS IS TUNABLE

Our previous works showed that, driven by the interfacial energy, the surface composition and materials' concentration could influence the size of the P4VP-protein NPs.[21,32] When the mass ratios of polymer to protein were adjusted as 1:8, 1:0.8 and 1:0.08 for the two streams in the microchannel, different size of NPs were fabricated with 2 µL/min flow rate. TEM images and DLS analysis show that the size of fabricated NPs increases with the increase of the polymer/protein mass ratio (**Figure 3.8a-d**). The average hydrodynamic sizes are 284 nm, 523 nm and 925 nm with polymer/protein ratio as 1:0.8, 1:0.08 and 1:0.008, respectively. Again, by comparing with the NPs produced by conventional bulk method, the size distributions of NPs fabricated through microfluidics were significantly improved (**Figure 3.8e** and **Figure 3.9a-d**). While the NPs fabricated by microfluidic method are stable at room temperature (**Figure 3.8f**), the size of NPs prepared by conventional bulk method shows growth within 3 days' incubation at room temperature, especially when high polymer/protein ratio was used (**Figure 3.8e**), we rationalize that it was caused by the agglomeration of polymers and NPs due to scattered protein coating on the surface of NPs.[31,33] The sustained size and morphology of NPs during the ethanol evaporation as well as long-term storage at 4 °C indicate that mature and stable polymer protein NPs have been formed via microfluidic co-assembly (**Figure 3.10**). The interactions between polymer and proteins and the benign microenvironment provided by polymers likely contribute to the stability of the enzyme and the resultant assemblies. The protein loading efficiencies of NPs fabricated with the microfluidic method under different conditions (with 2 µL/min to 10 µL/min flow rates and 1:1 to 1:10 polymer/protein

mass ratios) were measured (**Figure 3.11**). They were around 70%, demonstrating a good protein loading capacity using this microfluidic method. Interestingly, if the entrance width of the channel is decreased into 90 μm, much smaller NPs can be fabricated, nevertheless the NPs size cannot be well-controlled by adjusting polymer/protein mass ratio anymore (**Figure 3.12**). We believe that the matching of mixing time and co-assembly time is critical to control the size of final NPs. With further increasing mixing intensity, the NPs size could be insensitive to the starting materials ratio. Similar phenomenon has been reported for self-assembly of copolymeric NPs.[53]
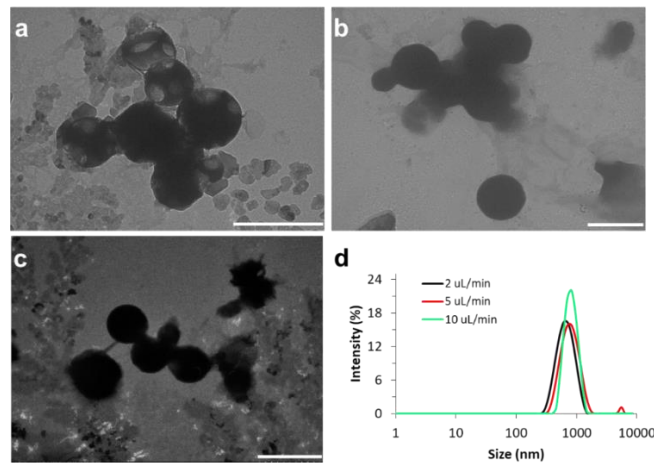


**Figure 3.7** TEM images of P4VP-BSA nanoparticles prepared by microfluidic method without electric field with 2 μL/min (a), 5 μL/min (b), 10 μL/min (c) flow rate, and the DLS test (d). Final concentration as P4VP 0.05 mg/mL, BSA 0.05 mg/mL. The result is consistent with DLS test, which confirm the role of EK based mixing contribute to the NPs' size and size distribution. Scale bar: 1 μm.
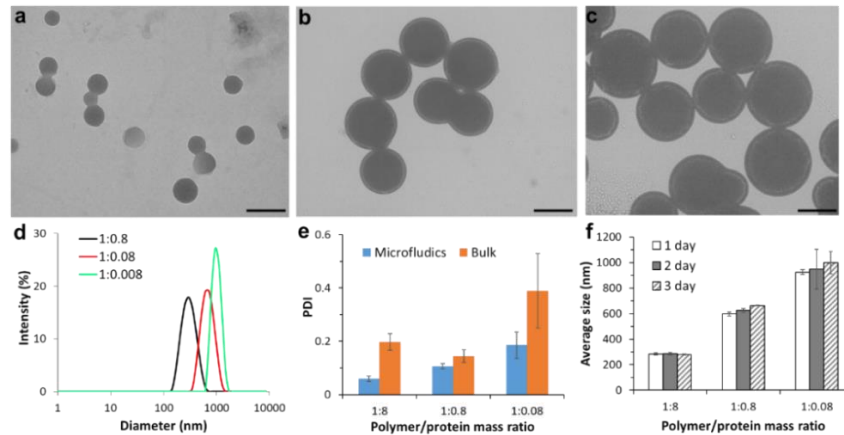
**Figure 3.8** Different size of P4VP-BSA NPs fabricated by adjusting polymer/protein ratio and the stability test. (a-c) Representative TEM images of P4VP-BSA with different size fabricated by microfluidics. Scale bars represent 0.5 μm. (d) DLS analysis of different size of NPs fabricated by microfluidics. (e) PDI comparison of the NPs fabricated by microfluidics and conventional bulk method. **P-value < 0.01, *P-value < 0.05 by Student's t-test. (f) Average hydrodynamic size of NPs fabricated by microfluidics with different aging time at room temperature as detected by DLS. A fixed concentration of 0.05 mg/mL was used for P4VP, while BSA was adjusted from 0.4 mg/mL to 0.04 mg/mL to 0.004 mg/mL for the fabrication of small, medium, and large size NPs. Error bar stands for standard deviation of triplicate samples.
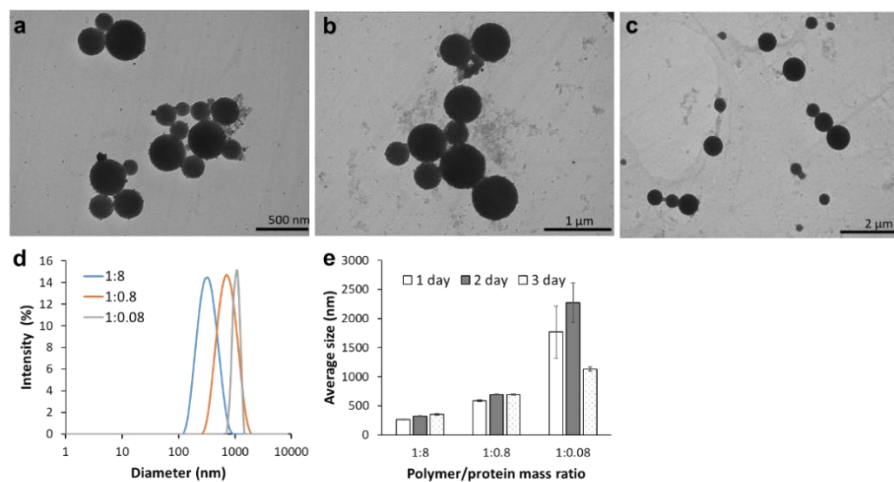


**Figure 3.9** P4VP-BSA NPs prepared by conversional dropwise and stirring method and thermostability test. The average size of NPs can be adjusted by protein/polymer ratio. (a-c) Representative TEM images of P4VP-BSA with different average size. (d) DLS measurement of the NPs with the polydispersity index as 0.20, 0.14, and 0.39, respectively. 0.05 mg/mL P4VP was used for all sample, BSA was used as 0.4 mg/mL, 0.04 mg/mL and 0.004 mg/mL for different size of nanoparticles. (e) Average hydrodynamic size of NPs with time going at room temperature, which was detected by DLS.
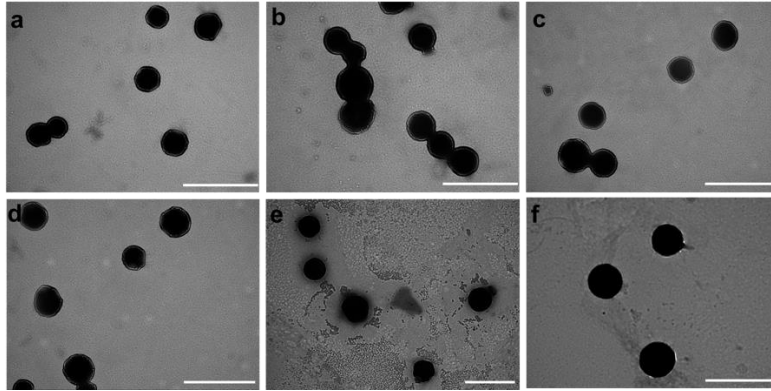
**Figure 3.10** TEM images of P4VP-BSA nanoparticles prepared by microfluidics with storing at 4 °C for 30 days (a-c) and during ethanol evaporation. Flow rate was with 2 μL/min (a), 5 μL/min (b), 10 μL/min (c-f). Final concertation of P4VP 0.05 mg/mL, BSA 0.05 mg/mL for all samples. (d) Samples without evaporation (with 10% ethanol), (e) samples with 50% volume evaporation (with <5% ethanol left), and (f) samples with 90% volume evaporation (with <1% ethanol left). No much difference was observed among the samples during ethanol evaporation, which implies a stable nanostructure. Evaporation was done at 45 °C heating block. Scale bars: 1 μm.
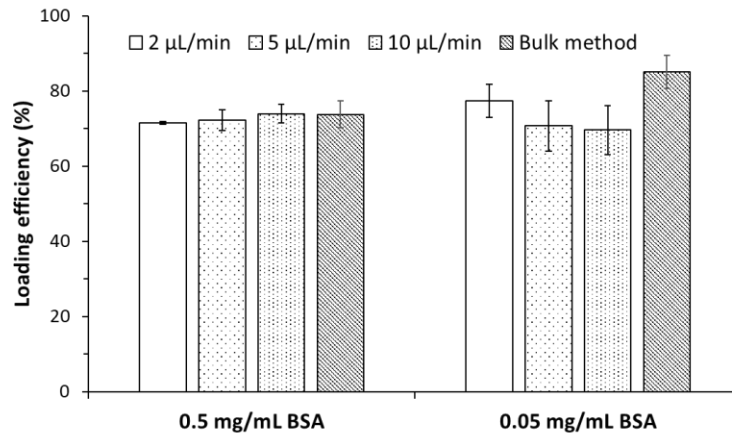


**Figure 3.11** Loading efficiency test with P4VP-BSA NPs fabricated with different methods: Different flow rates (2 μL/min, 5 μL/min and 10 μL/min) were tested for microfluidic method. Final concentration of P4VP was 0.05 mg/mL for all samples. Error bar stands for standard deviation of three replicates.
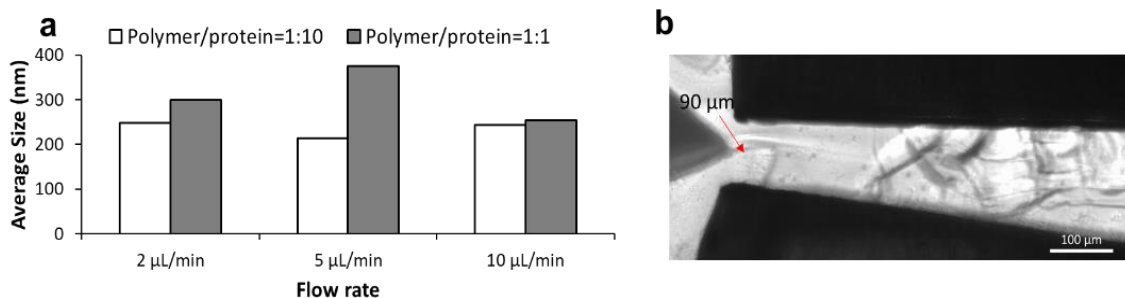
**Figure 3.12** DLS analysis of P4VP-BSA nanoparticles (a) prepared by a different microchannel with 90 μm width at the channel entrance, and other dimensions were kept the same (b). For all samples, 0.05 mg/mL P4VP was used, and 0.5 mg/mL and 0.05 mg/mL BSA were used, respectively. For EK-based microfluidics control, 20 Vp-p, 20 kHz frequency, 180° phase shift are used.

### 3.4.4. POLYMER-FLUORESCENT PROTEINS CO-ASSEMBLY AND FUNCTION TEST

To characterize the structural change of NPs fabricated by microfluidic method, EGFP and another fluorescent protein mCherry (or BSA) were used to co-assemble with P4VP polymer to produce polymer multi-protein NPs P4VP-EGFP-mCherry and P4VP-EGFP-BSA. Mass ratio of polymer/EGFP/mCherry (or BSA) was fixed as 4:1:1. The BSA was used in the P4VP-EGFP-BSA to balance the polymer protein ratio to control the NPs size. TEM imaging reveals that the homogeneous polymer proteins NPs were fabricated successfully by microfluidic method (**Figure 3.13**). Fluorescence images of P4VP-EGFP-mCherry and P4VP-EGFP-BSA NPs were taken by a laser scanning confocal microscopy (**Figure 3.14**). This laser is suitable to excite EGFP and minimize the 'cross talk' signal from mCherry simultaneously (P4VP-mCherry-BSA NPs cannot be detected, data not shown). Both P4VP-EGFP-mCherry and P4VP-EGFP-BSA NPs showed bright signals in green channel. By excluding the effect of EGFP 'leaking' signal in red channel and the minimal 'cross-talk' signal from mCherry, the red/green signal

86

intensity ratio was calculated for P4VP-EGFP-mCherry and P4VP-EGFP-BSA single NPs to show an apparent fluorescence resonance energy transfer (FRET). The red/green signal intensity ratio of P4VP-EGFP- mCherry is much higher than that of P4VP-EGFP-BSA (~two-fold changes, **Figure 3.14g**), which reveals significant FRET occurring between the assembled EGFP and mCherry on the NPs. This result not only demonstrates the function of both fluorescent proteins still sustained but also implies a very closed distance between the two proteins on the NPs, which could be potentially used for bio-imaging applications.[54]
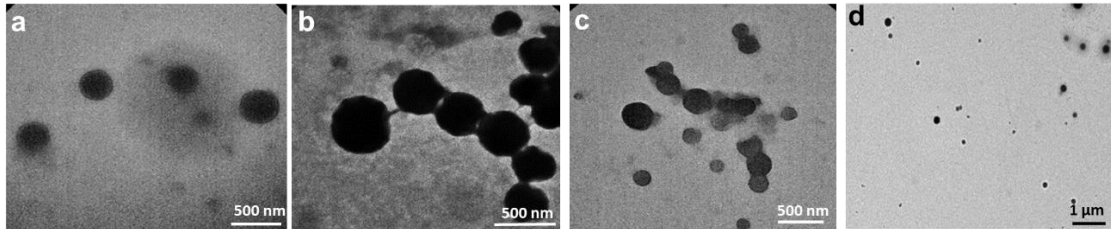


**Figure 3.13** TEM images of P4VP-EGFP-BSA (a), P4VP-EGFP-mCherry prepared by microfluidic method with 10 µL/min (b) and conventional stirring method (c). Mass ratio of P4VP: total proteins = 2:1. P4VP-CmlI NPs prepared by conventional stirring method (d). For assembly,.0.25 mg/mL P4VP, 1.1 mg/mL CmlI were used.
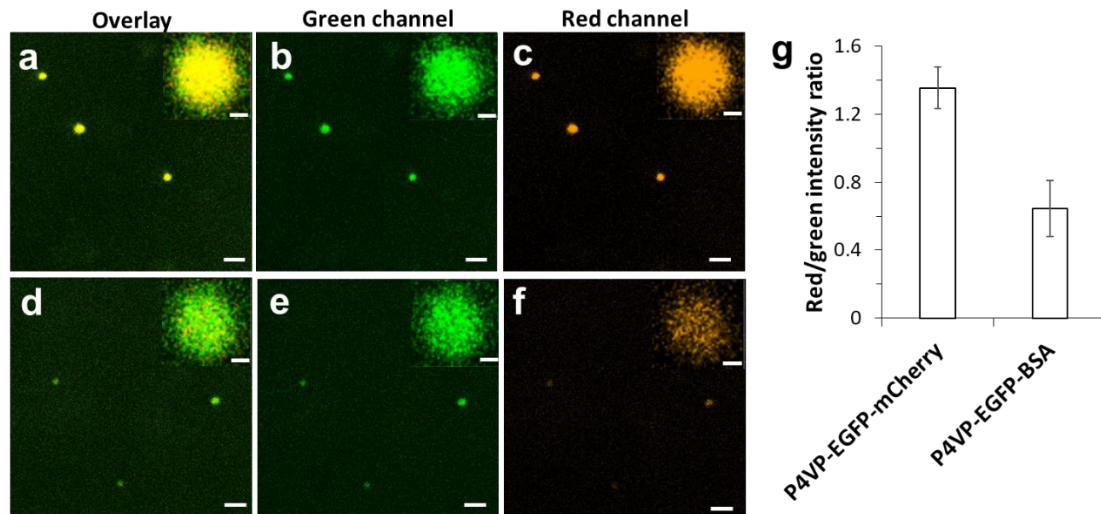
**Figure 3.14** Function characterization of P4VP-protein(s) NPs prepared by microfluidic method. Fluorescence microscopy images of P4VP-EGFP-mCherry (a-c), P4VP-EGFP-BSA (d-f) show the sustained fluorescence protein(s) function on NPs and a significant FRET effect (insets). Scale bars: 5 μm. Insets: representative image of single P4VP-EGFP-BSA and P4VP-EGFP-mCherry NP; Scale bars: 500 nm. (g) Signal intensity ratio of Red to green channels of P4VP-EGFP-mCherry and P4VP-EGFP-BSA prepared by microfluidic method. Error bar stands for standard deviation of ten single nanoparticles of each samples. For co-assembly, 0.05 mg/mL P4VP, 0.0125 mg/mL EGFP, 0.0125 mg/mL mCherry or 0.0125 mg/mL BSA and 2 μL/min flow rate were used.

## 3.4.5. POLYMER-ENZYME CO-ASSEMBLY AND ACTIVITY TEST

To further evaluate the sustained protein function on the NPs, an N-oxygenase CmlI[55] was used as a model enzyme to co-assemble with P4VP polymer by microfluidic and conventional bulk method (as reported previously).[51] TEM image reveals highly uniform P4VP-CmlI NPs fabricated by this microfluidic method (**Figure 3.15a**). It is worth to note that the homogeneity of P4VP-CmlI NPs is slightly better than other P4VP-proteins NPs by using microfluidic method, which could be attributed to multiple factors including protein's MW, surface charge and hydrophobicity and others. More systematic study will be needed to understand this difference. CmlI enzyme activity can be determined by a *p*-nitrosophenol (*p*NOP) based chromogenic assay with presence of *p*-aminophenol (*p*AP) as substrate,

nicotinamide adenine dinucleotide (NADH) as electron source and phenazine mediator (**Figure 3.15a inset**).[51] By comparing with the activity with the same amount of free enzyme, P4VP-CmlI NPs from either microfluidic method or bulk method show slightly higher activity than the free enzyme (**Figure 3.15b**), which can be attributed to the faster electron transferring process upon polymer assembly.[51] This result confirms that CmlI enzyme function can be fully maintained after co-assembly with P4VP using the microfluidic system.
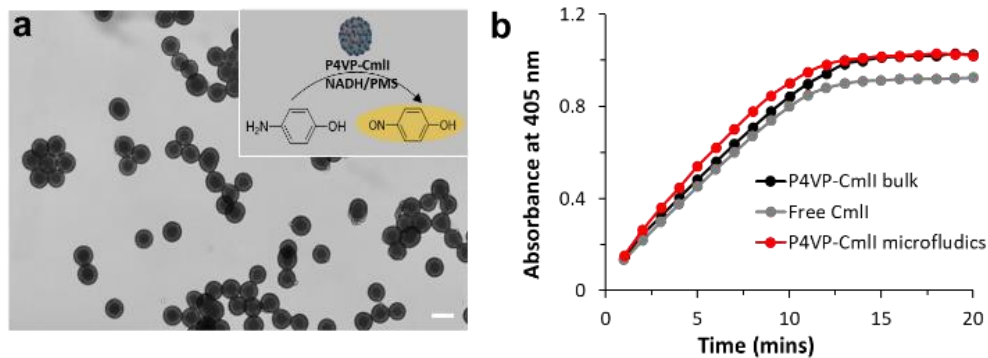


**Figure 3.15** (a) Representative TEM image of P4VP-CmlI NPs generated by microfluidic method and the chromogenic reaction scheme (inset), which can be used to characterize the polymer-enzyme NPs' activity. Flow rate 2 μL/min was used for NPs preparation. Scale bar: 200 nm. (b) The chromogenic reaction shows that P4VP-CmlI NPs from microfluidic method have enzyme function fully sustained. Flow rate 10 μL/min was used for the NPs sample production. For co-assembly in both microfluidic method and stirring method 0.25 mg/mL P4VP, 1.1 mg/mL CmlI were used. For the chromogenic activity assay 1 mM pAP, 2 mM NADH, 40 μM PMS were used.

3.5. CONCLUSION

In this work, we described an EK-based microfluidic method to fabricate functional polymer-protein(s) NPs. The principle of fast mixing in the microchannel was illustrated qualitatively. Experimentally, we identified the size distribution of NPs fabricated by this microfluidic method could be significantly improved by comparing to that prepared by conventional bulk method due to the fast mixing process. The NPs size could be controlled by adjusting polymer/proteins ratio in the microchannel. More importantly, the

89

functionality of proteins coated were sustained. Overall, this EK-based microfluidic method displayed great advantages to fabricate functional nanoparticles, which could be potentially used in nanoparticle preparation applications in the future.

## 3.6 REFERENCES

(1)     Balazs, A. C.; Emrick, T.; Russell, T. P. Nanoparticle Polymer Composites: Where Two Small Worlds Meet. *Science* **2006**, *314* (5802), 1107–1110.

(2)     Rao, J. P.; Geckeler, K. E. Polymer Nanoparticles: Preparation Techniques and Size-Control Parameters. *Prog. Polym. Sci.* **2011**, *36* (7), 887–913.

(3)     McQuade, D. T.; Pullen, A. E.; Swager, T. M. Conjugated Polymer-Based Chemical Sensors. *Chem. Rev.* **2000**, *100* (7), 2537–2574.

(4)     Sha, L.; Wang, D.; Mao, Y.; Shi, W.; Gao, T.; Zhao, Q.; Wang, S. Hydrophobic Interaction Mediated Coating of Pluronics on Mesoporous Silica Nanoparticle with Stimuli Responsiveness for Cancer Therapy. *Nanotechnology* **2018**, *29* (34), 345101.

(5)     Li, W.-P.; Shanmugam, V.; Huang, C.-C.; Huang, G.-D.; Huang, Y.-K.; Chiu, S.-H.; Yeh, C.-S. Eccentric Inorganic-Polymeric Nanoparticles Formation by Thermal Induced Cross-Linked Esterification and Conversion of Eccentricity to Raspberry-like Janus. *Chem. Commun. (Camb.)* **2013**, *49* (16), 1609–1611.

(6)     Hadinoto, K.; Sundaresan, A.; Cheow, W. S. Lipid–Polymer Hybrid Nanoparticles as a New Generation Therapeutic Delivery Platform: A Review. *European Journal of Pharmaceutics and Biopharmaceutics* **2013**, *85* (3, Part A), 427–443.

(7)     Care, A.; Bergquist, P. L.; Sunna, A. Solid-Binding Peptides: Smart Tools for Nanobiotechnology. *Trends Biotechnol.* **2015**, *33* (5), 259–268.

(8)     Mahmoudi, M.; Lynch, I.; Ejtehadi, M. R.; Monopoli, M. P.; Bombelli, F. B.; Laurent, S. Protein−Nanoparticle Interactions: Opportunities and Challenges. *Chem. Rev.* **2011**, *111* (9), 5610–5637.

(9)     Welch, R. P.; Lee, H.; Luzuriaga, M. A.; Brohlin, O.; Gassensmith, J. J. Protein-Polymer Delivery: Chemistry from the Cold Chain to the Clinic. *Bioconjugate Chem.* **2018**, 29 (9), 2867–2883.

(10)     Lu, Y.; Xue, F.; Zhou, Z.; Shi, M.; Yan, Y.; Qin, L.; Yang, H.; Yang, S. Phosphorescent Polymeric Nanoparticles by Coordination Cross-Linking as a Platform

for Luminescence Imaging and Photodynamic Therapy. *Chemistry* **2014**, *20* (49), 16242–16247.

(11)     Melnychuk, N.; Klymchenko, A. S. DNA-Functionalized Dye-Loaded Polymeric Nanoparticles: Ultrabright FRET Platform for Amplified Detection of Nucleic Acids. *J. Am. Chem. Soc.* **2018**, *140* (34), 10856–10865.

(12)     Khambalkar, V.; Birajdar, S.; Adhyapak, P.; Kulkarni, S. Nanocomposite of Polypyrrol and Silica Rods-Gold Nanoparticles Core–Shell as an Ammonia Sensor. *Nanotechnology* **2019**, *30* (10), 105501.

(13)     Zhang, Y.; Ge, J.; Liu, Z. Enhanced Activity of Immobilized or Chemically Modified Enzymes. *ACS Catal.* **2015**, *5* (8), 4503–4513.

(14)     Ding, Y.; Kang, Y.; Zhang, X. Enzyme-Responsive Polymer Assemblies Constructed through Covalent Synthesis and Supramolecular Strategy. *Chem. Commun.* **2014**, *51* (6), 996–1003.

(15)     Fan, W.; Liu, L.; Zhao, H. Co-Assembly of Patchy Polymeric Micelles and Protein Molecules. *Angew. Chem. Int.* **2017**, *56* (30), 8844–8848.

(16)     Hudalla, G. A.; Sun, T.; Gasiorowski, J. Z.; Han, H.; Tian, Y. F.; Chong, A. S.; Collier, J. H. Gradated Assembly of Multiple Proteins into Supramolecular Nanomaterials. *Nature Materials* **2014**, *13* (8), 829–836.

(17)     Chen, J.; Wu, M.; Gong, L.; Zhang, J.; Yan, B.; Liu, J.; Zhang, H.; Thundat, T.; Zeng, H. Mechanistic Understanding and Nanomechanics of Multiple Hydrogen-Bonding Interactions in Aqueous Environment. *J. Phys. Chem. C* **2019**, *123* (7), 4540–4548.

(18)     Wang, T.; Fan, X.; Hou, C.; Liu, J. Design of Artificial Enzymes by Supramolecular Strategies. *Curr. Opin. Struct. Biol.* **2018**, *51*, 19–27.

(19)     Unzueta, U.; Serna, N.; Sánchez-García, L.; Roldán, M.; Sánchez-Chardi, A.; Mangues, R.; Villaverde, A.; Vázquez, E. Engineering Multifunctional Protein Nanoparticles by in Vitro Disassembling and Reassembling of Heterologous Building Blocks. *Nanotechnology* **2017**, *28* (50), 505102.

(20)     Gräfe, C.; Lühe, M. von der; Weidner, A.; Globig, P.; Clement, J. H.; Dutz, S.; Schacher, F. H. Protein Corona Formation and Its Constitutional Changes on Magnetic Nanoparticles in Serum Featuring a Polydehydroalanine Coating: Effects of Charge and Incubation Conditions. *Nanotechnology* **2019**, *30* (26), 265707.

(21)     Suthiwangcharoen, N.; Li, T.; Wu, L.; Reno, H. B.; Thompson, P.; Wang, Q. Facile Co-Assembly Process to Generate Core–Shell Nanoparticles with Functional Protein Corona. *Biomacromolecules* **2014**, *15* (3), 948–956.

91

(22)     Tuncel, D.; Volkan Demir, H. Conjugated Polymer Nanoparticles. *Nanoscale* **2010**, *2* (4), 484–494.

(23)     Renna, L. A.; Boyle, C. J.; Gehan, T. S.; Venkataraman, D. Polymer Nanoparticle Assemblies: A Versatile Route to Functional Mesostructures. *Macromolecules* **2015**, *48* (18), 6353–6368.

(24)     Duranoğlu, D.; Uzunoglu, D.; Mansuroglu, B.; Arasoglu, T.; Derman, S. Synthesis of Hesperetin-Loaded PLGA Nanoparticles by Two Different Experimental Design Methods and Biological Evaluation of Optimized Nanoparticles. *Nanotechnology* **2018**, *29* (39), 395603.

(25)     Zhao, H.; Lin, Z. Y.; Yildirimer, L.; Dhinakar, A.; Zhao, X.; Wu, J. Polymer-Based Nanoparticles for Protein Delivery: Design, Strategies and Applications. *J. Mater. Chem. B* **2016**, *4* (23), 4060–4071.

(26)     DeFrates, K.; Markiewicz, T.; Gallo, P.; Rack, A.; Weyhmiller, A.; Jarmusik, B.; Hu, X. Protein Polymer-Based Nanoparticles: Fabrication and Medical Applications. *Int J Mol Sci* **2018**, *19* (6) 1717.

(27)     Badilescu, S.; Packirisamy, M. Microfluidics-Nano-Integration for Synthesis and Sensing. *Polymers* **2012**, *4* (2), 1278–1310.

(28)     Karnik, R.; Gu, F.; Basto, P.; Cannizzaro, C.; Dean, L.; Kyei-Manu, W.; Langer, R.; Farokhzad, O. C. Microfluidic Platform for Controlled Synthesis of Polymeric Nanoparticles. *Nano Lett.* **2008**, *8* (9), 2906–2912.

(29)     Kim, Y.; Lee Chung, B.; Ma, M.; Mulder, W. J. M.; Fayad, Z. A.; Farokhzad, O. C.; Langer, R. Mass Production and Size Control of Lipid–Polymer Hybrid Nanoparticles through Controlled Microvortices. *Nano Lett.* **2012**, *12* (7), 3587–3591.

(30)     Dendukuri, D.; Doyle, P. S. The Synthesis and Assembly of Polymeric Microparticles Using Microfluidics. *Advanced Materials* **2009**, *21* (41), 4071–4086.

(31)     Li, T.; Wu, L.; Suthiwangcharoen, N.; Bruckman, M. A.; Cash, D.; Hudson, J. S.; Ghoshroy, S.; Wang, Q. Controlled Assembly of Rodlike Viruses with Polymers. *Chem. Commun.* **2009**, *0* (20), 2869–2871.

(32)     Li, T.; Ye, B.; Niu, Z.; Thompson, P.; Seifert, S.; Lee, B.; Wang, Q. Closed-Packed Colloidal Assemblies from Icosahedral Plant Virus and Polymer. *Chem. Mater.* **2009**, *21* (6), 1046–1050.

(33)     Li, T.; Niu, Z.; Emrick, T.; Russell, T. P.; Wang, Q. Core/Shell Biocomposites from the Hierarchical Assembly of Bionanoparticles and Polymer. *Small* **2008**, *4* (10), 1624–1629.

(34)    Lu, L.; Yuan, L.; Yan, J.; Tang, C.; Wang, Q. Development of Core–Shell Nanostructures by In Situ Assembly of Pyridine-Grafted Diblock Copolymer and Transferrin for Drug Delivery Applications. *Biomacromolecules* **2016**, *17* (7), 2321–2328.

(35)    Feng, Q.; Sun, J.; Jiang, X. Microfluidics-Mediated Assembly of Functional Nanoparticles for Cancer-Related Pharmaceutical Applications. *Nanoscale* **2016**, *8* (25), 12430–12443.

(36)    Kim, H.; Min, K.-I.; Inoue, K.; Im, D. J.; Kim, D.-P.; Yoshida, J. Submillisecond Organic Synthesis: Outpacing Fries Rearrangement through Microfluidic Rapid Mixing. *Science* **2016**, *352* (6286), 691–694.

(37)    Dobhal, A.; Kulkarni, A.; Dandekar, P.; Jain, R. A Microreactor-Based Continuous Process for Controlled Synthesis of Poly-Methyl-Methacrylate-Methacrylic Acid (PMMA) Nanoparticles. *J. Mater. Chem. B* **2017**, *5* (18), 3404–3417.

(38)    Wang, G. R.; Yang, F.; Zhao, W. There Can Be Turbulence in Microfluidics at Low Reynolds Number. *Lab Chip* **2014**, *14* (8), 1452–1458.

(39)    Wang, G.; Yang, F.; Zhao, W.; Chen, C.-P. On Micro-Electrokinetic Scalar Turbulence in Microfluidics at a Low Reynolds Number. *Lab Chip* **2016**, *16* (6), 1030–1038.

(40)    Zhao, W.; Yang, F.; Wang, K.; Bai, J.; Wang, G. Rapid Mixing by Turbulent-like Electrokinetic Microflow. *Chem. Eng. Sci.* **2017**, *165*, 113–121.

(41)    Oddy, M. H.; Santiago, J. G.; Mikkelsen, J. C. Electrokinetic Instability Micromixing. *Anal. Chem.* **2001**, *73* (24), 5822–5832.

(42)    Chen, C.-H.; Lin, H.; Lele, S. K.; Santiago, J. G. Convective and Absolute Electrokinetic Instability with Conductivity Gradients. *J. Fluid Mech.* **2005**, *524*, 263–303.

(43)    Yang, F.; Kuang, C.; Zhao, W.; Wang, G. AC Electrokinetic Fast Mixing in Non-Parallel Microchannels. *Chem Eng Comm* **2017**, *204* (2), 190–197.

(44)    Podgórska, W.; Marchisio, D. L. Modeling of Turbulent Drop Coalescence in the Presence of Electrostatic Forces. *Chem Eng Res Des* **2016**, *108*, 30–41.

(45)    Ramos, A.; Morgan, H.; Green, N. G.; Castellanos, A. Ac Electrokinetics: A Review of Forces in Microelectrode Structures. *J. Phys. D: Appl. Phys.* **1998**, *31* (18), 2338–2353.

(46)    R.F. Probstein, Physicochemical Hydrodynamics: An Introduction, 2nd Ed. John Wiley.2003.

(47)    Baygents, J. C.; Baldessari, F. Electrohydrodynamic Instability in a Thin Fluid Layer with an Electrical Conductivity Gradient. *Physics of Fluids* **1998**, *10* (1), 301–311.

(48)    J.R. Melcher, Continuum Electromechanics. MIT Press, Cambridge, MA. 1981.

(49)    G.A. Truskery, F. Yuan, D.F. Katz, Transport Phenomena in Biological Systems, 2nd Ed. Person, Prentice Hall. 2010.

(50)    Ma, J.; Lee, S. M.-Y.; Yi, C.; Li, C.-W. Controllable Synthesis of Functional Nanoparticles by Microfluidic Platforms for Biomedical Applications – a Review. *Lab Chip* **2017**, *17* (2), 209–226.

(51)    Zhang, L.; Xu, Y.; Makris, T. M.; Wang, Q. Enhanced Arylamine N-Oxygenase Activity of Polymer–Enzyme Assemblies by Facilitating Electron-Transferring Efficiency. *Biomacromolecules* **2018**, *19* (3), 918–925.

(52)    Wang, Q.; Lu, L.; Zhang, L.; Yuan, L.; Zhu, T.; Chen, W.; Wang, G. Artificial Cellulosome Complex from the Self-Assembly of NTANi Functionalized Polymeric Micelles and Cellulases. *ChemBioChem* 20,1394 –1399.

(53)    Johnson, B. K.; Prud'homme, R. K. Mechanism for Rapid Self-Assembly of Block Copolymer Nanoparticles. *Phys. Rev. Lett.* **2003**, *91* (11), 118302.

(54)    Arai, Y.; Nagai, T. Extensive Use of FRET in Biological Imaging. *Microscopy (Oxf)* **2013**, *62* (4), 419–428.

(55)    Lu, H.; Chanco, E.; Zhao, H. CmlI Is an N-Oxygenase in the Biosynthesis of Chloramphenicol. *Tetrahedron* **2012**, *68* (37), 7651–7654.

CHAPTER 4

USING SMALL MOLECULES TO ENHANCE OLETSA ENZYME ACTIVITY IN

SITU

## 4.1 INTRODUCTION

Conversion of aliphatic carboxylic acids (e.g. fatty acids) into fuels and platform chemicals represents a sustainable strategy in chemical industry. Despite the success of current chemical methodologies in the decarboxylation of aliphatic carboxylic acids,[1–3] the required harsh conditions and high loadings of precious metal catalysts imply a high environmental impact. Therefore, a biocatalytic process at mild condition would be a viable alternative.[4,5] Although some enzymes that utilize iron-containing cofactors to active $O_2$ or $H_2O_2$ for the transformation of $C_n$ fatty aldehyde or fatty acids to $C_{n-1}$ alkenes have been reported recently,[6–9] the relatively sluggish catalytic efficiencies of the native enzymes limit their practical applications.

Recently, increasing attentions have been given to a group of cytochrome P450s from the CYP152 family named OleT, which catalyses the oxidative decarboxylation of fatty acids to form terminal olefins.[10–12] This single-step reaction provides a route for drop-in fuel production from an abundant natural resource. After the discovery of OleT$_{JE}$ from *Jeotgalicoccus sp.* 8456 by Rude and co-workers in 2011,[10] collective efforts have been placed to understand this biocatalyst and the unique decarboxylation pathways. With $H_2O_2$ as a co-factor,[13] the highly reactive and remarkably stable intermediates compound I[14] and compound II[15] can be generated to achieve decarboxylation instead of the oxygen rebound producing hydroxylated products. Therefore, $H_2O_2$ has served as a desirable attribute for industrial transformations because of its low cost and easily scalability. On the other hand, the $H_2O_2$ dependent decarboxylation is highly inefficient compared to most

O₂ dependent CYPs, primarily due to the potential for oxidative modification of heme prosthetic group.[16] To overcome this limitation, different strategies including protein engineering,[17] photochemistry[18] and process engineering[19] that generate $H_2O_2$ in a controlled manner have been reported. Very recently, a functional ortholog from *Staphylococcus aureus*, $OleT_{SA}$, was characterized by Thomas Makris and others that possesses improved features including enhanced solubility and high stability.[20,21] These features enable this ortholog to be a promising candidate for synthesis applications.

Similar to many other P450s, OleT has been demonstrated to accommodate a broad range of substrates including different fatty acids and non-native substrates with a diverse size distribution and structure variation.[11,22] Based on site-directed mutagenesis studies, small alterations of the local microenvironment[23,24] can be translated into its reactivity. Interestingly enough, the C-C bond cleavage in OleT can be regulated by modifications of the enzyme F-G loop that is 17 Å from the active site, reflecting a flexible substrate pocket which can impart effect on its catalysis.[20,25] In addition, cooperative binding of different compounds with other P450 enzymes[26–29] and multiple substrates binding in the enzyme active center[30] have been experimentally investigated by many groups. Therefore, we envisioned that the application of appropriate small molecules to access the OleT enzyme active pocket may be a promising direction to leverage its catalysis efficiency.

The fatty acid binding pocket in OleT demonstrates a highly hydrophobic feature. Particularly, hydrophobic residues including Phe46, Phe294, Phe79, Phe173, Phe291, Phe246, Phe296, Val292, Pro246, Ile170 serve as a 'hydrophobic

97

cage' for the fatty acid substrate in OleT$_{JE}$,[22,31] which are also highly conserved in OleT$_{SA}$.[20] Wang and co-workers reported that only meagre or no activity improvement was observed with the mutation of Phe to Ala near both substrate entrance and the active site suggesting steric hindrance has minor impact during the catalysis.[22] We hypothesize that nonpolar small molecules have chances to access the enzyme hydrophobic pocket and influence the catalysis. To test this hypothesis, a list of small molecules was synthesized, and the OleT enzyme catalytic activity was analysed in the presence and absence of these small molecules. Our results showed that these molecules could enter the enzyme active center and affect the heme spin state. Interestingly, some of these molecules could augment the enzymatic activity of OleT. The enhanced effect of these molecules is more prominent when high concentration of $H_2O_2$ was used to active the enzyme. And if an $H_2O_2$ gradual releasing method was used, such as the GOx method as described in Chapter 2, the enhanced effect of the small molecules was diminished. We therefore proposed that the origin of the enhancement was from the enzyme oxidation step and the inhibition of the toxic effect due to a rapid $H_2O_2$ consumption may have played a critical role in this process.

## 4.2 EXPERIMENTAL SECTION

### 4.2.1 MATERIALS

Eicosanoic acid (C20:0), stearic acid (C18:0), palmitic acid (C16:0), myristic acid (C14:0), lauric acid (C12:0), and capric acid (C10:0) were purchased from BDH Chemicals. The alkene standard 1-hexadecene was purchased from TCI chemicals. Benzene, toluene, GOx from *Aspergillus niger*, $H_2O_2$, hydrocinnamic acid, and 3-(4-

98

bromophenyl) propionic acid were purchased from Sigma-Aldrich. D-Glucose was purchased from Fisher. Unless otherwise noted, all chemicals and solvents used were of analytical grade and were used as received from commercial sources. Unless otherwise noted, a solution of 200 mM $K_2HPO_4$, 100 mM NaCl, pH 7.4 was used as buffer.

### 4.2.2 OLET$_{SA}$ ENZYME EXPRESSION AND PURIFICATION

The protein expression and purification process is the same as that described in Chapter 2. Briefly, the kanamycin-resistant plasmid T5 containing a OleT$_{SA}$-His$_6$ gene was transformed BL21(DE3) containing the chloramphenicol-resistant pTF2 plasmid encoding for GroEL/GroES/Tig chaperones. A modified Terrific Broth (TB) (24 g/L yeast extract, 12 g/L tryptone, 4 g/L peptone) supplemented with 50 μg/mL kanamycin and 20 μg/mL chloramphenicol was used for culturing. For protein expression, 125 mg/L thiamine, and trace metals, 100 μM IPTG, 10 ng/mL tetracycline and 10 mg/L of 5-aminolevulinic acid were added. The expression was done at 18 °C for 16-18 h. The protein was purified using nickel-nitriloacetic acid (Ni-NTA) affinity chromatography followed by Butyl-S-Sepharose column polishing step as described previously. Fractions with an Rz value (Abs418 nm/Abs280 nm) above 1.2 were pooled and dialyzed against buffer A. Proteins were stored at -80 °C until further use.

### 4.2.3 GENERAL PROCEDURE TO PREPARE DIFFERENT MOLECULES
### 4.2.3.1 PREPARATION OF 1-PHENYL-1H-1,2,3-TRIAZOLE (MOLECULE **3**)
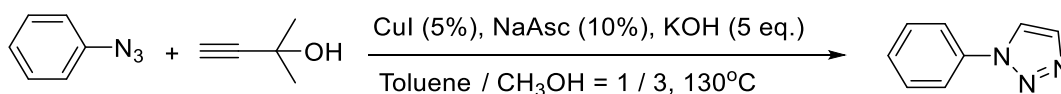


**Scheme 4.1** Synthesis of molecule **3**.

99

In an oven dried Schlenk tube, azidobenzene (1 mmol), 2-methylbut-3-yn-2-ol (1 mmol), CuI (5 mol%), Sodium ascorbate (10 mol%) and KOH (5 mmol) were mixed in toluene and methanol (v/v =1:3, 8 mL) stirred at 130 °C for 2 days under argon. The mixture was cooled down to room temperature and purified by flash chromatography (hexane/ethylacetate = 10:1-3:1) to afford the corresponding product of yield 70 %.[32]

4.2.3.2 PREPARATION OF 4-MONOSUBSTITUTED 1-PHENYL-1H-1,2,3-TRIAZOLE (MOLECULE **4** AND **7**)



R= *n*-butyl or CH$_3$OH
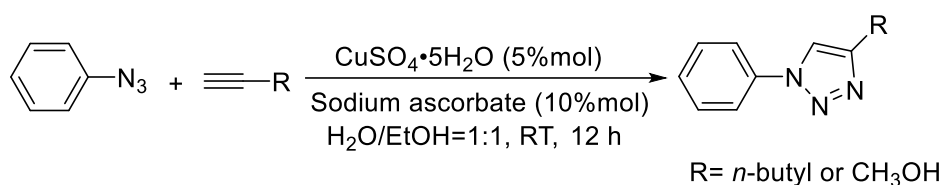
**Scheme 4.2** Synthesis of molecule **4** and **7**

Azidobenzene (1 mmol) and terminal alkene (1 mmol) were mixed in water and ethanol (v/v =1:1, 14 mL). Sodium ascorbate (10 mol%) of freshly prepared 1 M solution in water was added, followed by the addition of CuSO$_4$·5H$_2$O (5 mol%) in water. The mixture was stirred overnight at room temperature. The solvent was completely removed and purified by column using hexane/ethyl acetate= 10:1-2:1, or DCM/methanol = 100:1-50:1, as the eluent to afford the corresponding product. The average yields are 80-85 %.

### 4.2.3.3 PREPARATION OF N-SUBSTITUTED BENZENE SULFONAMIDE (MOLECULE 5)



R= *n*-butyl or ethyl
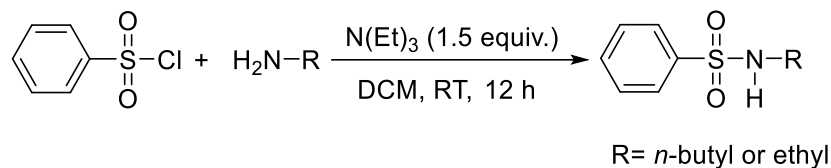
**Scheme 4.3** Synthesis of molecule **5**.

To a solution of N-butylamine or N-ethylamine (4 mmol) in dry DCM (10 mL), triethylamine (6 mmol) was added followed by a solution of benzenesulfonyl chloride (4 mmol) in dry DCM (10 mL) in an ice bath. The reaction mixture was stirred overnight at room temperature. The DCM was evaporated under reduced pressure, $H_2O$ (10 mL) was added, and the pH was adjusted to 2 with 1 N HCl. The product was extracted with DCM (3×10 mL), and the combined organic layers were concentrated under reduced pressure. The rude product was purified by column using Hexane/Ethyl acetate = 20:1-10:1 as eluent to afford the target product. The average yields were 85-88 %.

### 4.2.4 SMALL MOLECULES CHARACTERIZATION

The $^1H$ and $^{13}C$ NMR spectra were recorded at 298 K in deuterated solvents using Bruker Advance 400 MHz spectrometer. Data are represented as below: chemical shift, multiplicity (s = singlet, d = doublet, t = triplet, m = multiplet), coupling constants in Hertz (Hz), integration.

**1-phenyl-1*H*-1,2,3-trizaole** (Molecule **3)**

White solid. $^1H$ NMR (400 MHz, CDCl$_3$): $\delta$ 8.00 (d, $J$ = 0.1 Hz, 1 H), 7.84 (s, 1 H), 7.75-7.72 (m, 2 H), 7.54-7.49 (m, 2 H), 7.46-7.41 (m, 1 H). $^{13}C$ NMR (100 MHz, CDCl$_3$): $\delta$ 137.1, 134.6, 129.9, 128.9, 121.8, 120.8. HRMS: [M + H]$^+$ *m/z* calcd for C$_8$H$_7$N$_3$H$^+$: 146.0713, found: 146.0713.
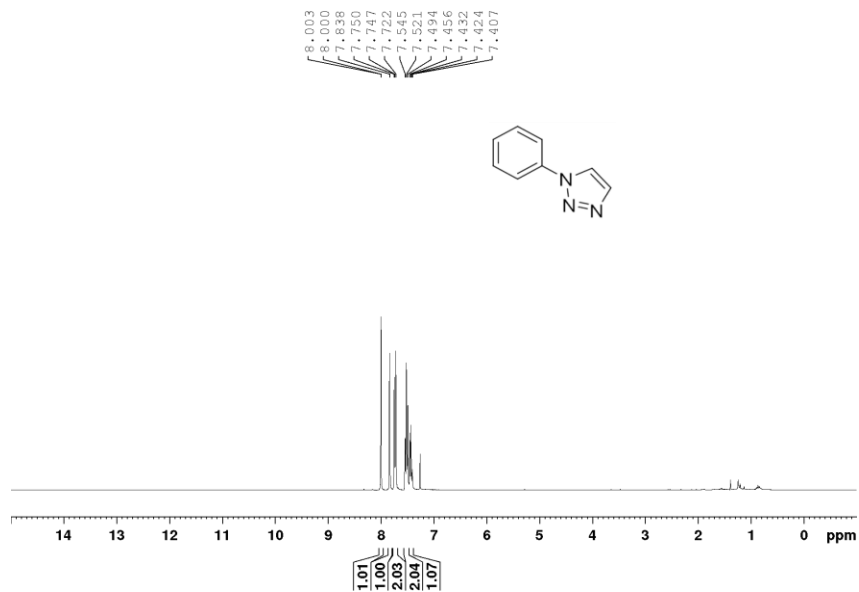
**Figure 4.1** ^{1}H NMR spectrum of Molecule **3**
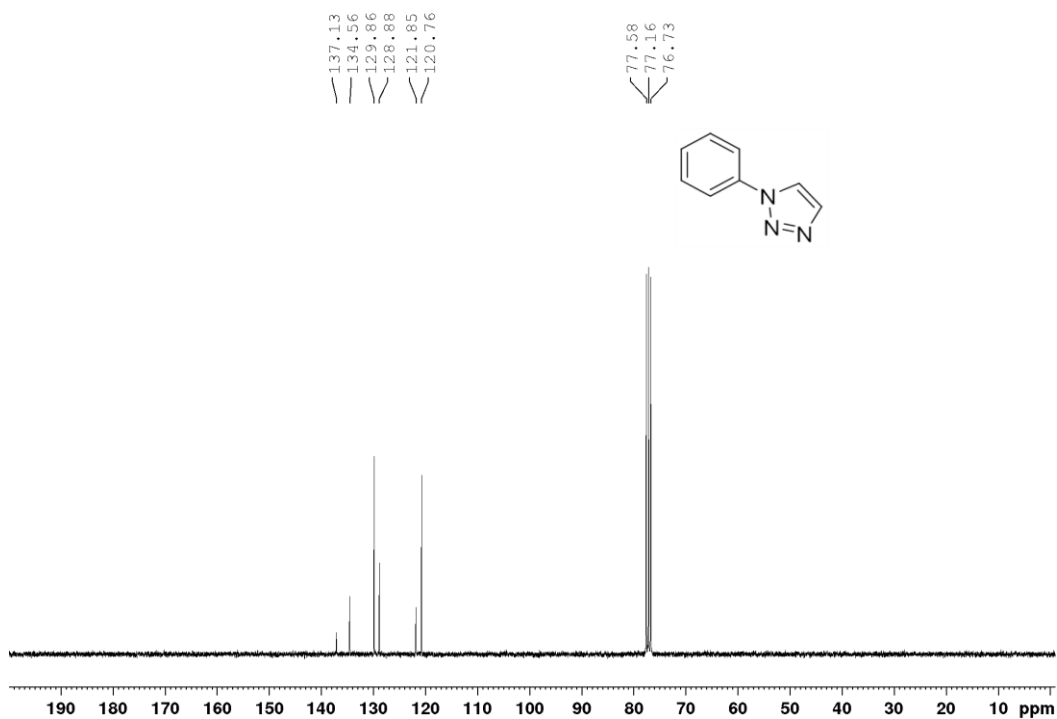


**Figure 4.2** ^{13}C NMR spectrum of Molecule **3**

**4-bultyl-1-phenyl-1H-1,2,3-triazole** (Molecule **4**)

Yellow solid. ^{1}H NMR (400 MHz, CDCl$_3$): $\delta$ 7.71 (s, 1 H), 7.68 (d, $J$ = 7.9 Hz, 2 H), 7.46 (d, $J$ = 7.7 Hz, 2 H), 7.39-7.33 (m, 1 H), 2.76 (d, $J$ = 7.7 Hz, 2 H), 1.74-1.64 (m, 2 H), 1.46-

102

1.33 (m, 2 H), 0.92 (t, $J$ = 7.3 Hz, 3 H). $^{13}$C NMR (100 MHz, CDCl$_3$): $\delta$ 149.2, 137.3, 129.7, 128.4, 120.3, 118.9, 31.5, 25.4, 22.3, 13.9. HRMS: [M + H]$^+$ $m/z$ calcd for C$_{12}$H$_{15}$N$_3$H$^+$: 202.1339, found: 202.1339
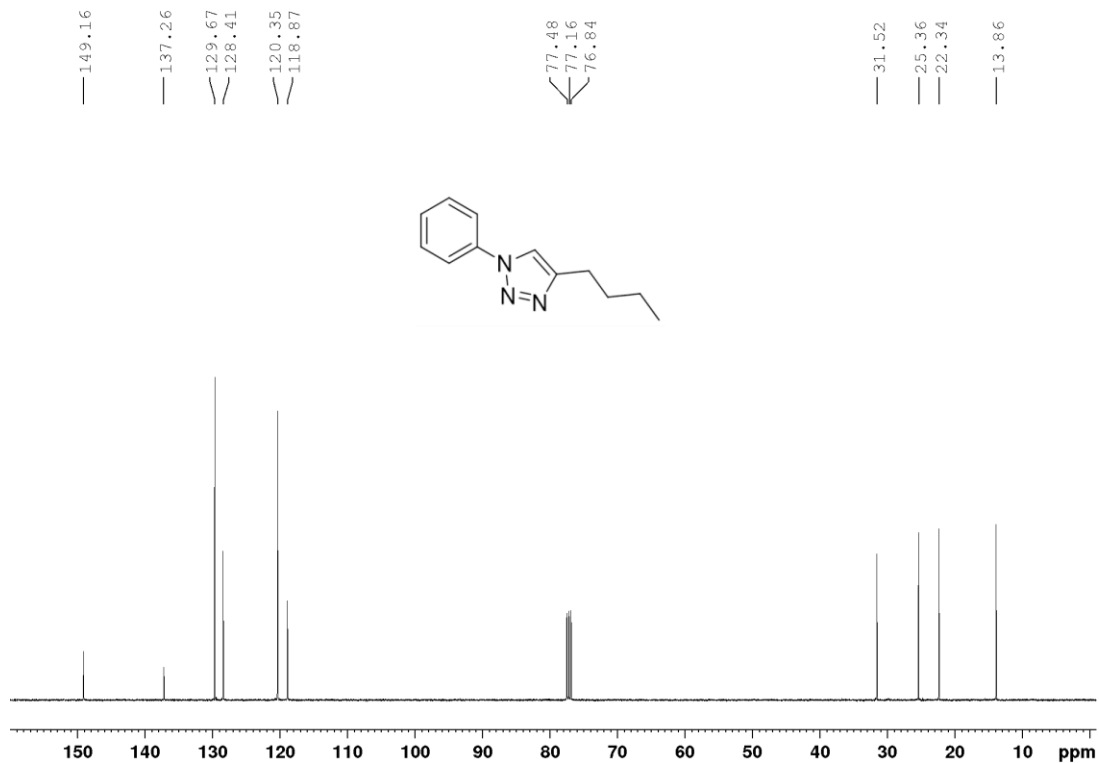


**Figure 4.3** $^1$H NMR spectrum of Molecule **4**
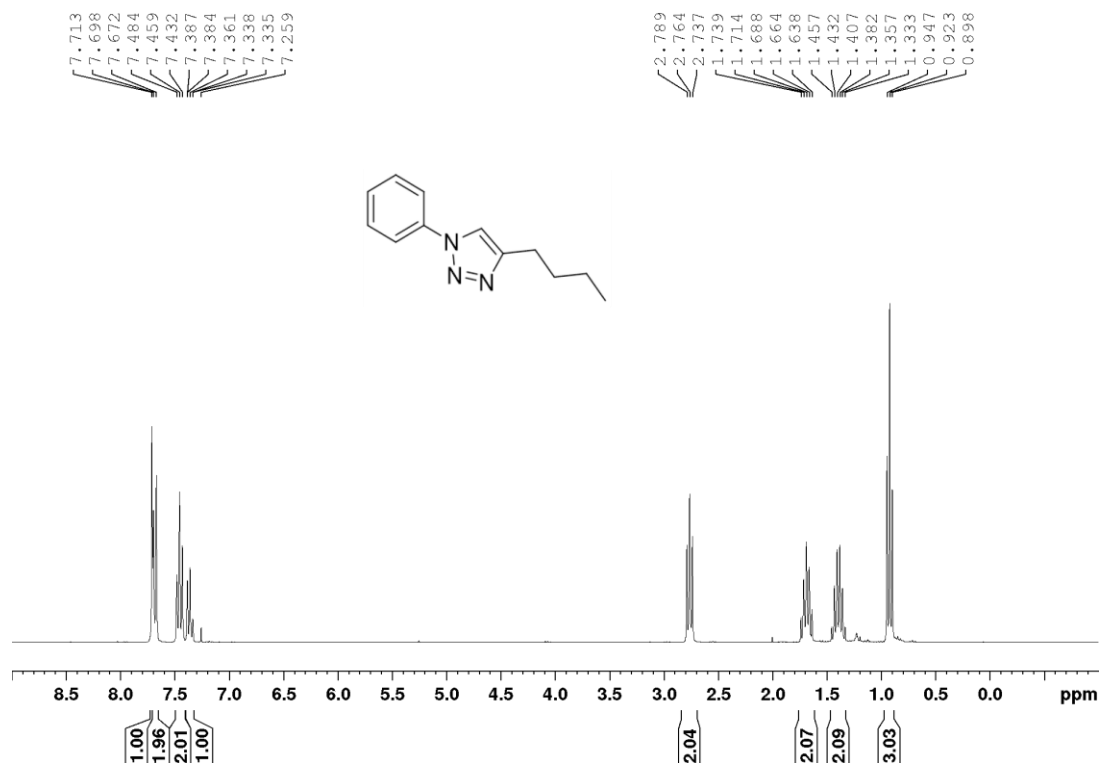
**Figure 4.4** ^{13}C NMR spectrum of Molecule **4**

**N-butylbenzenesulfonamide** (Molecule **5**)

Yellow oil. ^{1}H NMR (400 MHz, CDCl$_3$): $\delta$ 7.89-7.88 (m, 1 H), 7.87-7.86 (m, 1 H), 7.59-7.55 (m, 1 H), 7.52-7.48 (m, 2 H), 4.87 (s, 1H), 2.96-2.90 (m, 2 H), 1.46-1.39 (m, 2 H), 1.31-1.22 (m, 2 H), 0.82 (t, $J$ = 3.2 Hz, 3 H). ^{13}C NMR (100 MHz, CDCl$_3$): $\delta$ 140.0, 132.7, 129.2, 127.1, 43.0, 31.6, 19.8, 13.6. HRMS: [M + H]$^+$ $m/z$ calcd for C$_{10}$H$_{15}$NO$_2$SH$^+$: 214.0896, found: 214.0896.
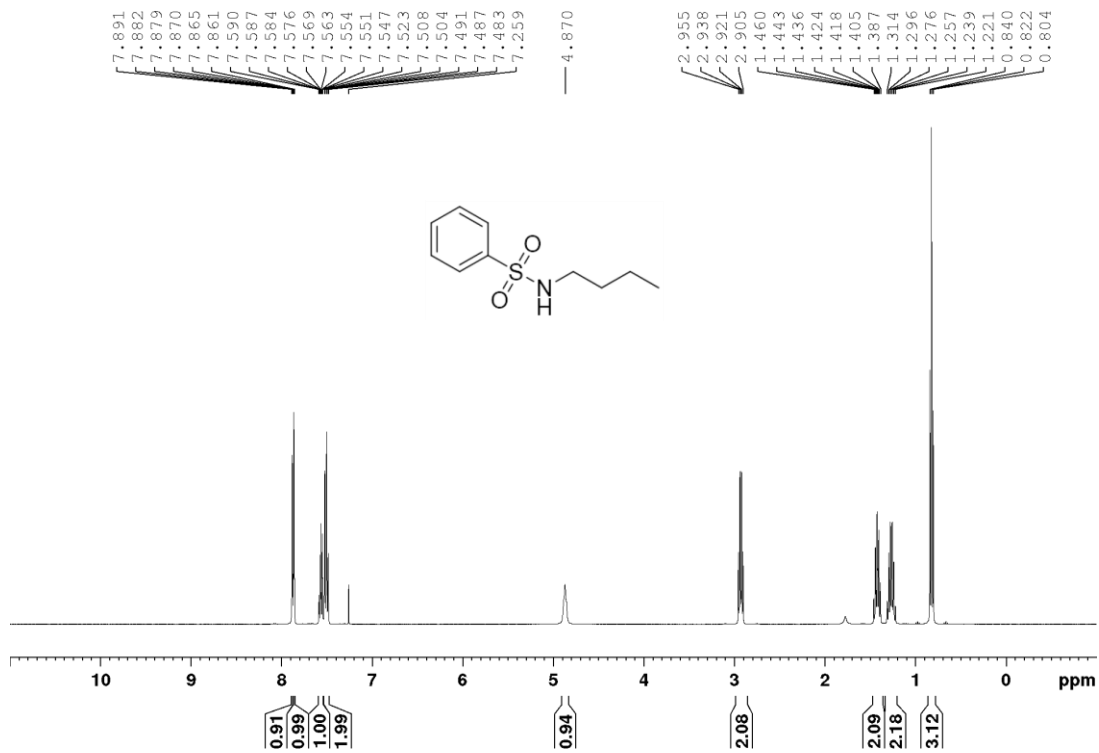
**Figure 4.5** ^{1}H NMR spectrum of Molecule **5**
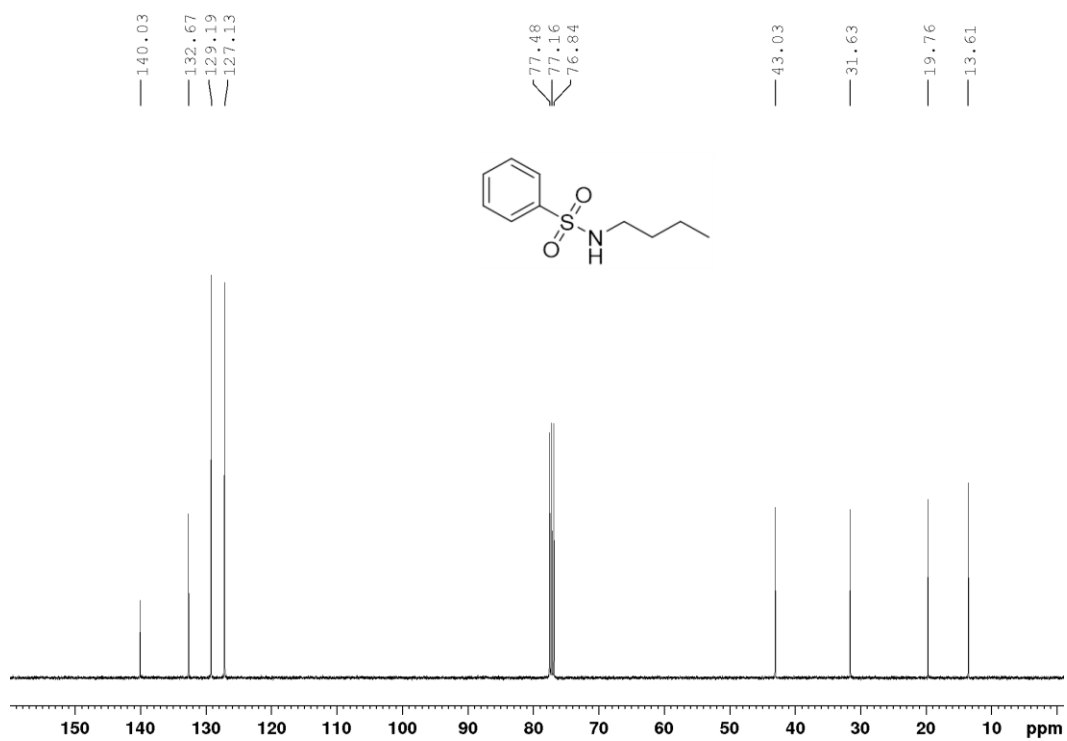


**Figure 4.6** ^{13}C NMR spectrum of compound Molecule **5**

**N-ethylbenzenesulfonamide** (Molecule **6**)

Yellow oil. $^1$H NMR (400 MHz, CDCl$_3$): $\delta$ 7.89-7.88 (m, 1 H), 7.87-7.86 (m, 1 H), 7.60-7.56 (m, 1 H), 7.54-7.49 (m, 2 H), 4.57 (s, 1 H), 3.05-2.98 (m, 2 H), 1.10 (t, $J$ = 7.2 Hz, 3 H). $^{13}$C NMR (100 MHz, CDCl$_3$): $\delta$ 140.0, 132.7, 129.2, 127.2, 38.4, 15.2. HRMS: [M + H]$^+$ $m/z$ calcd for C$_8$H$_{11}$NO$_2$SH$^+$: 186.0583, found: 186.0583.
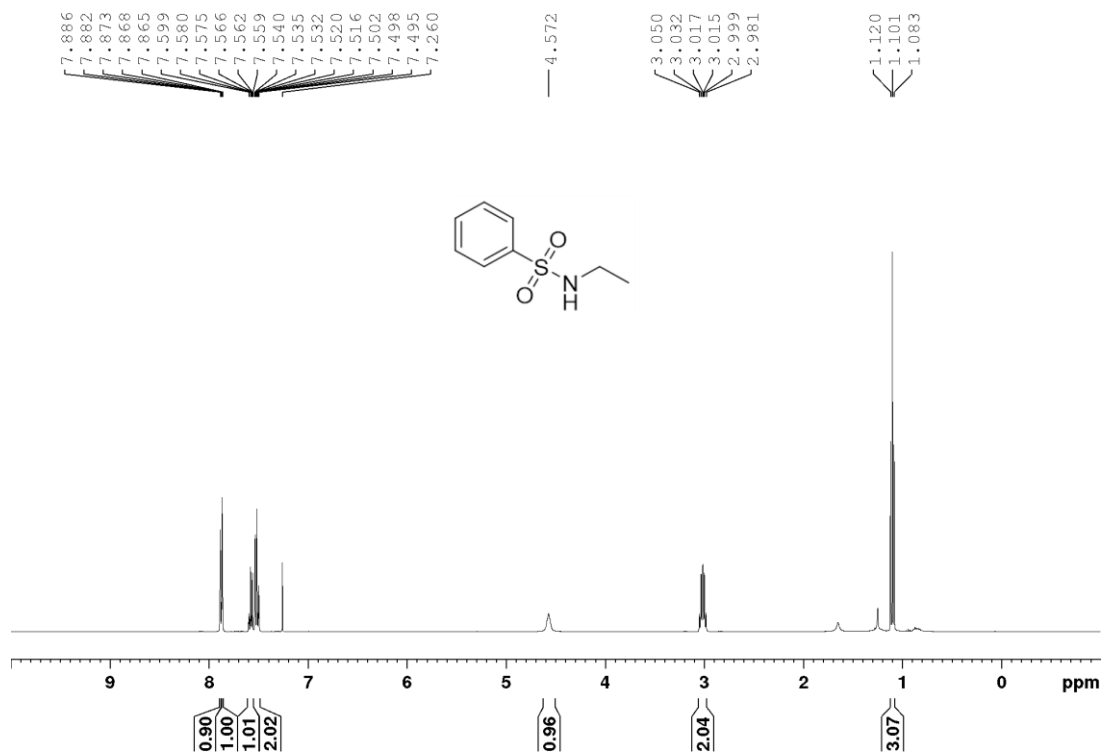


**Figure 4.7** $^1$H NMR spectrum of Molecule **6**
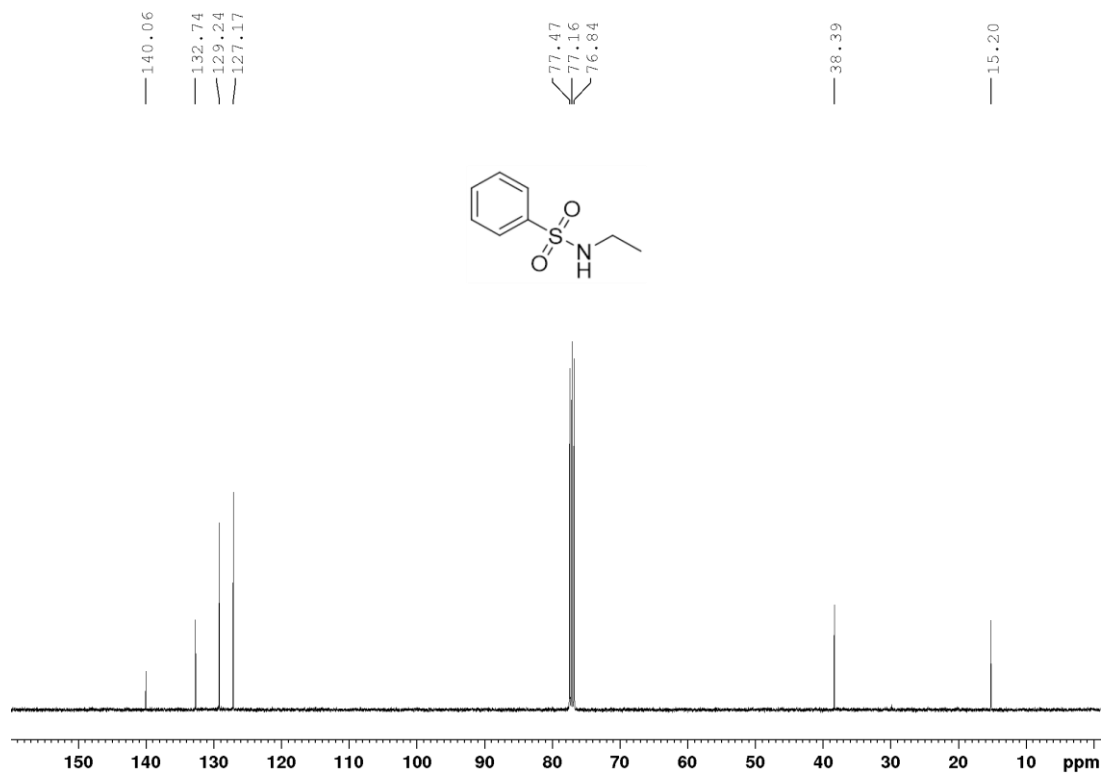
**Figure 4.8** $^{13}$C NMR spectrum of Molecule **6**

**(1-phenyl-1H-1,2,3-triazole-4-yl)methanol** (Molecule **7**)

Yellow oil. $^1$H NMR (400 MHz, DMSO-$d_6$): $\delta$ 8.69 (s, 1 H), 7.92-7.90 (m, 2 H), 7.62-7.58 (m, 2 H), 7.50-7.46 (m, 1 H), 5.36 (t, $J$ = 5.6 Hz, 1 H), 4.62 (d, $J$ = 5.7 Hz, 2 H). $^{13}$C NMR (100 MHz, DMSO-$d_6$): $\delta$ 149.7, 137.2, 130.3, 128.9, 121.5, 120.4, 55.4. HRMS: [M + H]$^+$ $m/z$ calcd for C$_9$H$_9$N$_3$OH$^+$: 176.0818, found: 176.0818.
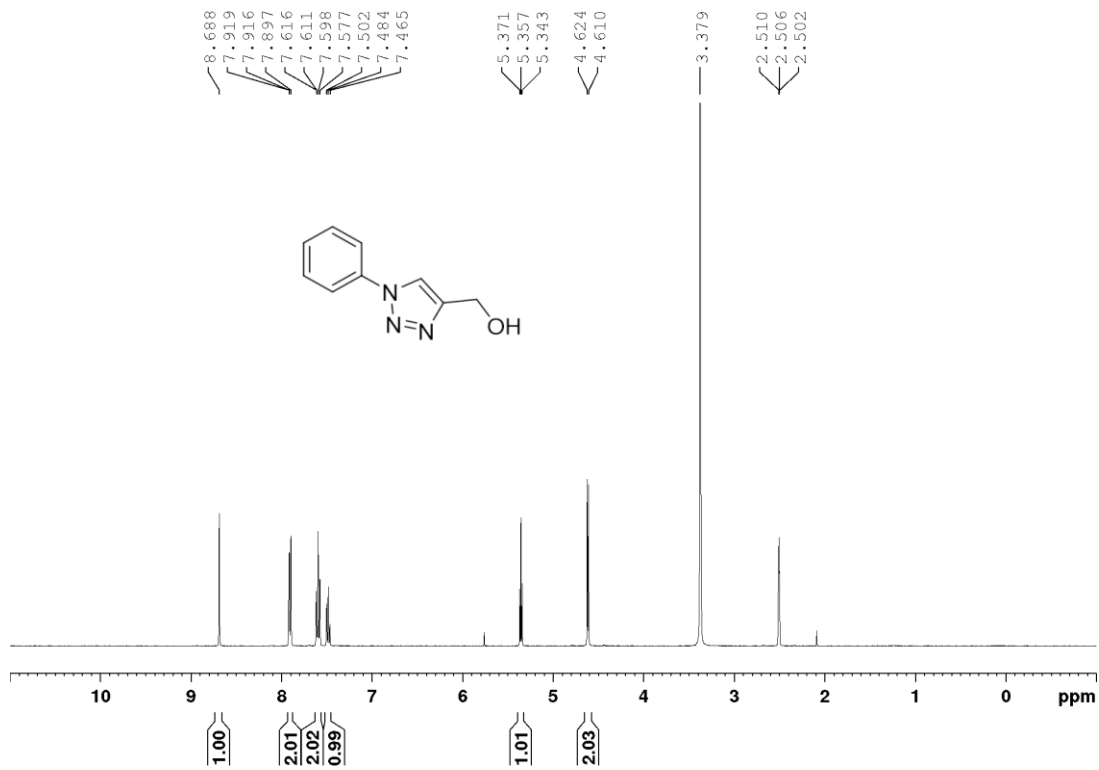
**Figure 4.9** ^{1}H NMR spectrum of Molecule **7**
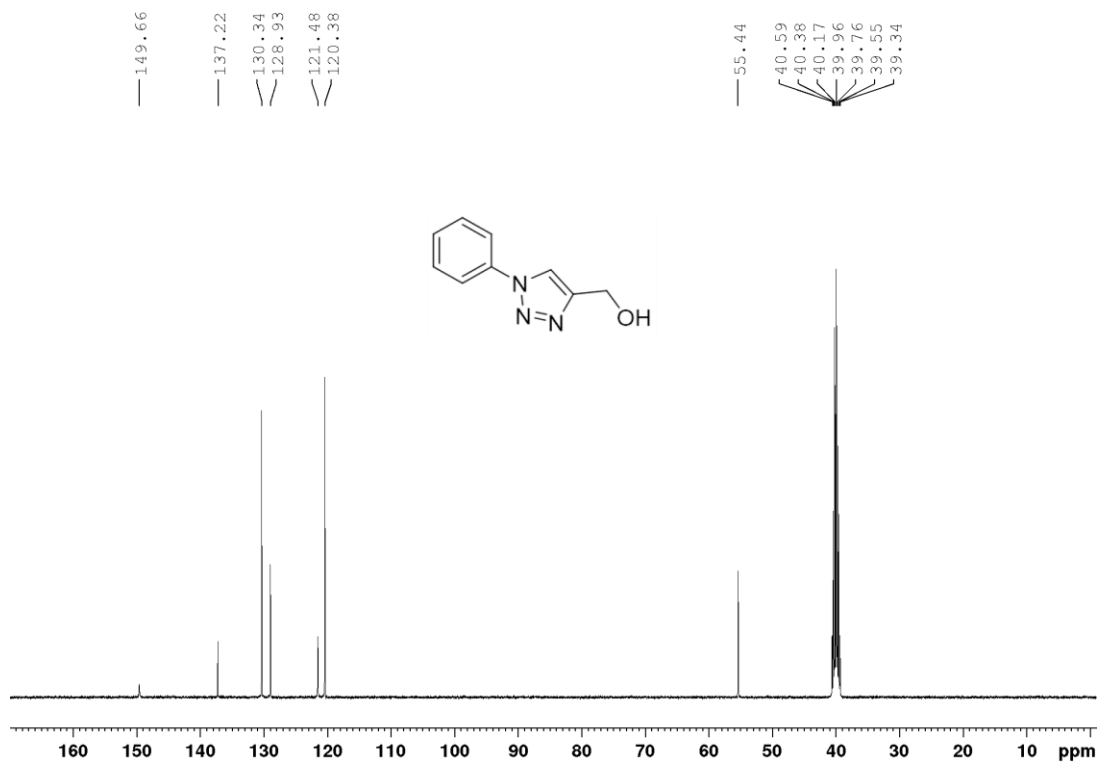


**Figure 4.10** ^{13}C NMR spectrum of Molecule **7**

## 4.2.5 UV-VIS SPECTRUM ANALYSIS

UV-Visible spectroscopy was detected on an HP 8453 spectrophotometer. A quartz cuvette with 1 cm path length was used. Different $OleT_{SA}$ enzyme in buffer A in the absence and presence of small molecules was analyzed.

## 4.2.6 OLET$_{SA}$ ENZYME ACTIVITY ASSAY

Eicosanoic acid and stearic acid stock (10 mM) were dissolved in 70% ethanol/30% Triton X-100 (v:v, unless otherwise noted) as stocks. Other fatty acids including palmitic acid, myristic acid and lauric acid were dissolved in DMSO to make 10 mM stocks. Hydrocinnamic acid and 3-(4-bromophenyl) propionic acid was dissolved in DMSO to make a 400 mM stock. To set up enzymatic reactions, $OleT_{SA}$ enzyme, substrate and small molecule diluted into desired concentration from stocks in buffer for multiple-turnover reactions in a 150 μL volume. Small molecules were omitted for control reactions. 2 mM of $H_2O_2$ was added to initiate the reactions in $H_2O_2$ method. 300 nM of GOx was used in GOx method, and 6.6 mM of D-glucose was added to initiate the reactions unless otherwise noted. The steady-state reactions were quenched with 0.4 mM HCl or 1% acetic acid for GC/GC-MS or LC/LC-MS analysis, respectively.
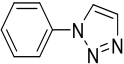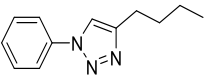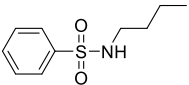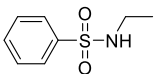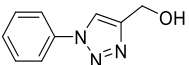
## 4.3 RESULT AND DISCUSSION

### 4.3.1 SMALL MOLECULES PROFILE EXPLORED ON OLET$_{SA}$ CATALYSIS

Initially benzene (**1**) and toluene (**2**) were added to the reaction of hydrocinnamic acid catalysed with $OleT_{SA}$. As shown in **Table 4.1**, an enhancement of 14% and 20% were observed respectively in the presence of 1 mM of benzene and toluene. This result promoted us to further synthesize a series of small molecules (**3-7**). OleT metabolized hydrocinnamic acid reactions with and without these small molecules were analyzed by HPLC (**Table 4.1**).

109

**Table 4.1** The small molecules' effect on OleT$_{SA}$ activity

| Molecule | Structure | OleT activity[a] enhancement (%) |
|:---:|:---:|:---:|
| 1 | | $14 \pm 2$ |
| 2 | | $20 \pm 3$ |
| 3 | | $79 \pm 11$ |
| 4 | | $209 \pm 23$[b] |
| 5 | | $101 \pm 18$[b] |
| 6 | | $63 \pm 5$ |
| 7 | | $-6 \pm 1$ |

[a] Reaction condition: 5 µM OleT$_{SA}$, 2 mM H$_2$O$_2$, 2 mM hydrocinnamic acid, incubation at RT for 30 min with and without 1 mM small molecules.
[b] Because OleT can further metabolize styrene into styrene oxide, which was not characterized in this work, the observed enhancement at 30 min reactions is lower than that at 10 min reactions (see **Figure 4.12**).

## 4.3.2 UV-VIS SPECTROSCOPIC ANALYSIS

It has been well established that UV-Vis spectra of cytochrome P450s is sensitive to the redox state of the heme as well as its local environment.[33] OleT is in a low-spin ferric resting state with its heme iron axially coordinated by cysteine thiolate and a distal H$_2$O molecule, which shows a maximum Soret band at 418 nm. Substrate binding displaces the axial water and converts the heme iron from low-spin to a high-spin state with a maximum Soret band at 394 nm (**Figure 4.11**).[16]

Therefore, we can readily use UV-Vis spectroscopy to evaluate the interaction of small molecules with the OleT active site. As shown in **Figure 4.12B**, with addition of 2.5 mM of **3** to $OleT_{SA}$ (at the low-spin state), a shift of heme spectrum was observed, indicating a close proximity of **3** to the heme. Similar phenomenon was observed for the as-purified $OleT_{SA}$ treating with **3** (**Figure 4.12C**), while **3** has no specific absorbance above 300 nm wavelength (**Figure 4.12D**). These spectrum shifts suggest an interfering effect between heme and $H_2O$/substrates. With addition of eicosanoic acid (C20 FA) followed by **3**, the enzyme shifted from low-spin state to high-spin state, clearly demonstrating that the presence of **3** does not hinder the C20 FA binding to the enzyme active site.
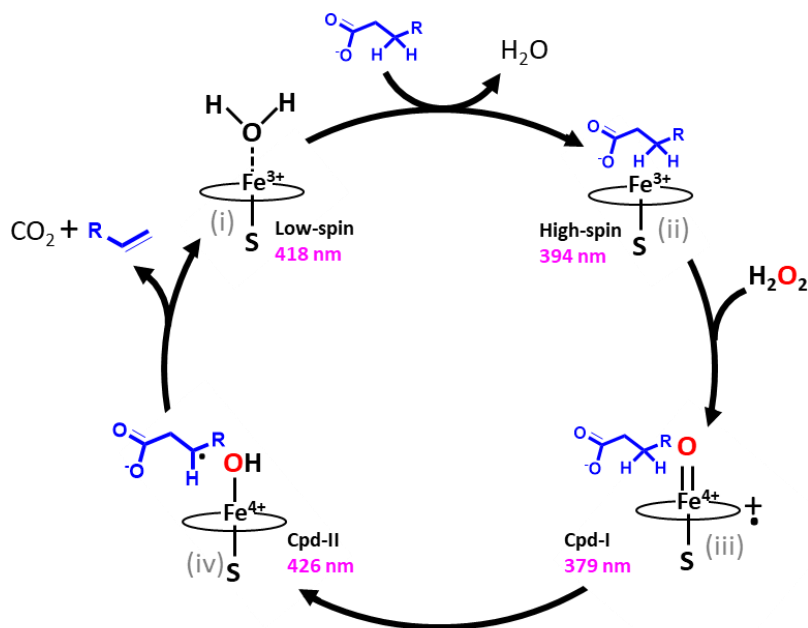


**Figure 4.11** Scheme of the $OleT_{SA}$ catalytic cycle. $OleT_{SA}$ is in a ferric resting state with its heme iron coordinated by a $H_2O$ molecule. (i). Substrate binding displaces the axial water and converts the heme iron from low-spin to a high-spin state. (ii). $H_2O_2$ reacts with the high-spin enzyme to yield the reactive ferryl (FeIV)-oxo porphyrin radical cation (Cpd I, iii). Cpd I abstracts a hydrogen atom from the Cβ position, resulting in formation of a substrate radical and the ferryl (FeIV)-hydroxo species (Cpd II, iv), from which Cα–Cβ double bond forms, a $CO_2$ eliminates and a terminal alkene releases. The simultaneous recruitment of a proton to the heme restores the resting state(i).
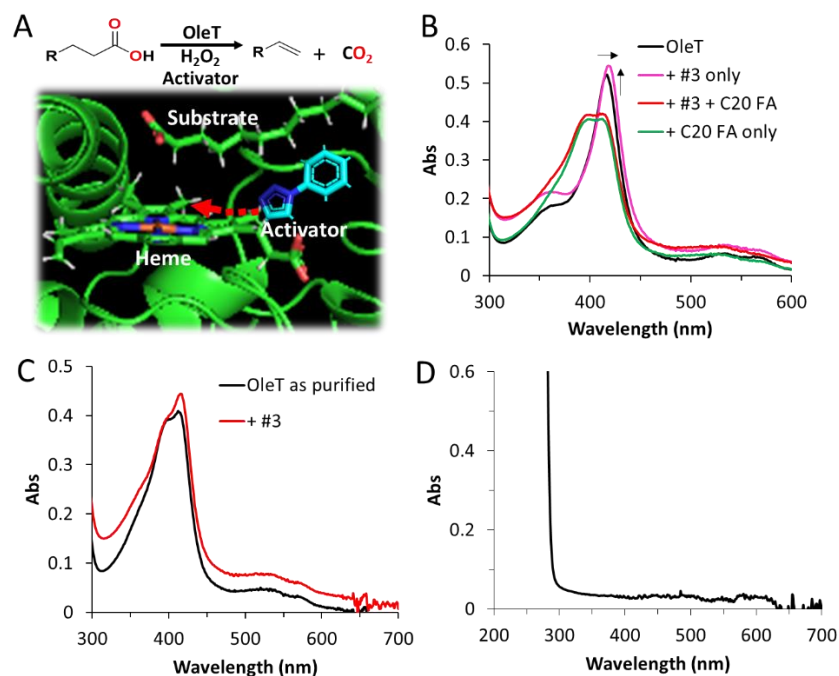
**Figure 4.12 (A)** Scheme of OleT_{SA} catalyzed decarboxylation reactions with activator (top) and fatty acids coordinating to the active center with small molecule accessing (bottom). **(B)** UV-Vis spectrum of low-spin state of OleT_{SA} (5 μM) binding with **3** (2.5 mM) and eicosanoic acid (5 μM). **(C)** UV-Vis spectrum of OleT_{SA} as purified treated by **3** (5 mM) and **(D) 3** only (5 mM).

### 4.3.3 OLET_{SA} ACTIVITY ANALYSIS IN THE PRESENCE OF SMALL MOLECULES

To test the effect of **3** on OleT_{SA} enzymatic activity, OleT catalyzed C20 FA reactions was done in the presence of different concentration of **3**. Nonadecene, as the sole product of the reaction, was monitored. As shown in **Figure 4.13A**, with increasing concentration of **3** from 1 mM to 20 mM added, increasing production of nonadecene was obtained, indicating that **3** acted as an OleT_{SA} enzyme activator in these reactions. Neither saturation nor inhibiting effect was observed, which implies that the small molecules do not hinder the C20 FA binding to the enzyme. A typical time course analysis of the reaction with C20 FA as substrate was shown in **Figure 4.13B**. Interestingly, a burst of product release was observed at 5 min of reaction, and more than 2.5-fold nonadecene yield was obtained in the presence of **3.** A similar

enhanced OleT activity was observed with stearic acid (C18 FA) and hydrocinnamic acid as substrates (**Figure 4.13C**, **Figure 4.14**). When the chain length of fatty acid got shorter, the enhancement of catalytic efficiency became less significant (e.g. 49% of enhancement for palmitic acid (C16 FA) vs. 31% of enhancement for myristic acid (C14 FA) vs. < 7% of enhancement for lauric acid (C12 FA) (**Figure 4.13C, Figure 4.14**). We believe that the varied conformation of the different chain length of fatty acids in the hydrophobic enzyme pocket may restrict the small molecule's effect. Above data support our hypothesis that the small molecules get access to enzyme pocket and accelerate the catalysis by modifying heme local environment (**Figure 4.11A**).
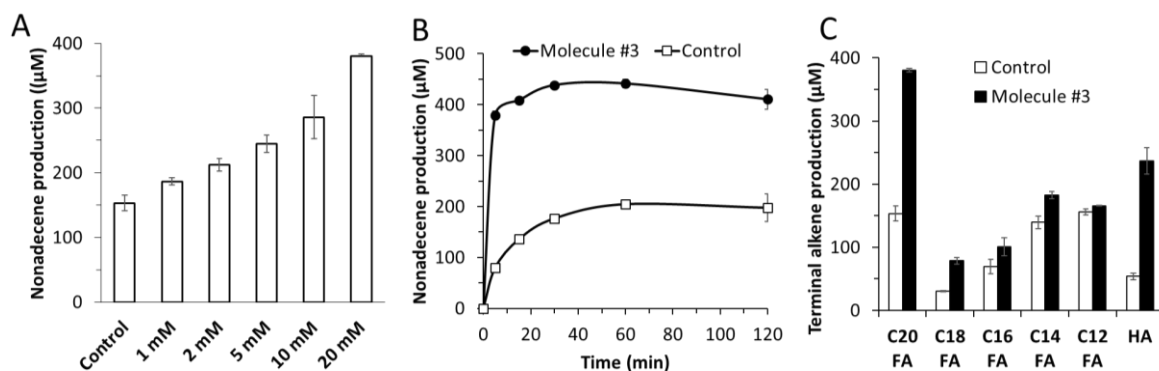


**Figure 4.13** (A) OleT$_{SA}$ activity test in the presence of different concentration **of 3.** Reaction condition: 5 μM OleT$_{SA}$, 1 mM C20 FA, 2 mM H$_2$O$_2$, 60 min at room temperature. (B) Time course study of nonadecene production in the presence or absence of **3**. Reactions were performed with 1 mM C20 FA, 2 mM H$_2$O$_2$, with 20 mM **3** or without **3** (as control). (C) Up to 3.5-fold enhanced OleT activity in the presence of **3** can be achieved depending on different substrates including C20 FA, C18 FA, C16 FA, C14 FA, C12 FA and hydrocinnamic acid (HA). Only corresponding terminal alkene production was recorded here. Reaction condition: 5 μM OleT$_{SA}$, 1 mM substrates. 2 mM H$_2$O$_2$. Note: C20 fatty acid was dissolved in 70% ethanol/30% triton, all other substrate stocks were dissolved in DMSO. For the reactions with C20, C18, C16, C14 FA substrates, 20 mM small molecule was used; for reactions with C12 FA and HA substrate, 2 mM small molecule was used. Error bars indicate the standard deviation of duplicate experiments (n = 2).
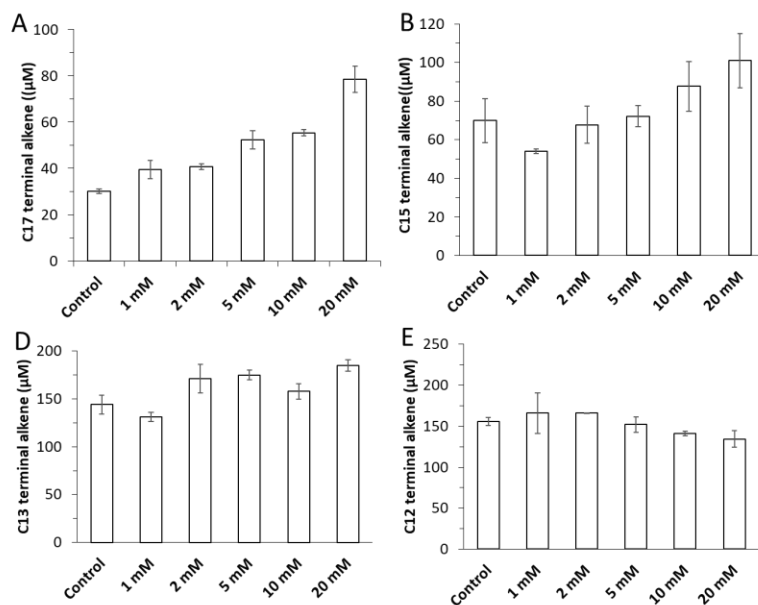
**Figure 4.14** Molecule **3** concentration dependence tests of OleT$_{SA}$ catalysis with C18 FA (A), C16 FA (B), C14 FA (C) and C12 FA (D). Corresponding alkene production was reported. Reaction condition: OleT$_{SA}$ 5 µM, fatty acid 0.5 mM, and 2 mM H$_2$O$_2$, 150 µL reaction incubation RT for 60 minutes. 250 µM C16 alkene was used as internal standard. 300 µL CHCl$_3$ extraction before GC. Error bars indicate the standard deviation of duplicate experiments (n = 2).

While **3** displays significantly activating effect on OleT catalysis, a high working concentration is required. One possible reason for this limitation is because of its low potency to pass through the enzyme channel. To overcome this limitation, by mimicking the fatty acid structure, **4** was synthesized with a four-carbon 'tail' attached to the triazole group (**Table 1**, **4**). We hypothesize that this molecule is easier to get into OleT enzyme active site, thus it can facilitate the catalysis by coordinating the heme structure and substrates. To avoid the potential blocking effect on fatty acids substrates due to the carbon tail of 4, hydrocinnamic acid (HA) and bromophenyl propionic acid (BA) were used as substrates to identify the effect of **4** on the enzyme activity. As shown in **Figure 4.15A**, in the presence of 1 mM of **4**, OleT$_{SA}$ displayed significant improved catalytic efficiency (5.5-fold enhancement for HA, 1.5-fold enhancement for BA relative to that in the absence of such small

114

molecules). Since HA binding does not introduce spin shift of OleT significantly, we used BA as a model to illustrate the binding spectra of OleT$_{SA}$ with **4**. As shown in **Figure 4.15B,** by treating with 50 μM BA, the enzyme showed a significant low-spin to high-spin switch. With the addition of **4** (the concentration increased from 50 μM to 200 μM) followed by BA, further extent of spin shifts of OleT$_{SA}$ occurred demonstrating a cooperative-like binding of small molecule and substrate with OleT active site. Furthermore, in the presence of 2 mM **4**, around 1-fold of decreased K$_D$ was obtained compared to that in the absence of small molecule (**Figure 4.15C**, **D**). Unexpectedly, we found that **4** could be hydroxylated by OleT$_{SA}$ with a slow reaction rate (**Figure 4.16**). Overall, these results confirm our hypothesis that the selected small molecules and substrates locate to the enzyme active site simultaneously as shown in **Figure 4.11A**. C20 FA metabolism was also tested in the presence of **4**, no notable enhanced OleT activity was observed, which may be attributed to the blocking effect of these small molecules to the large fatty acids. or a different conformation of the more complicated van der Waals complex. Further investigation of the enzyme/small molecules complex structure will be helpful to understand the reasons.

Another set of molecules including **5**, **6**, **7** (Table 4.1) were synthesized to further explore the potential OleT enzyme activators with HA as substrate. **5** can also serve as a potent OleT activator (e.g. > 100% enhancement of OleT activity on hydrocinnamic acid). While with a short 'hydrophobic tail' in **6**, the enhanced effect was significant decreased. With one hydroxyl group added in the end of the tail of

**7**, the enhanced effect on the enzyme was totally abolished implying the importance of the nonpolar tails.
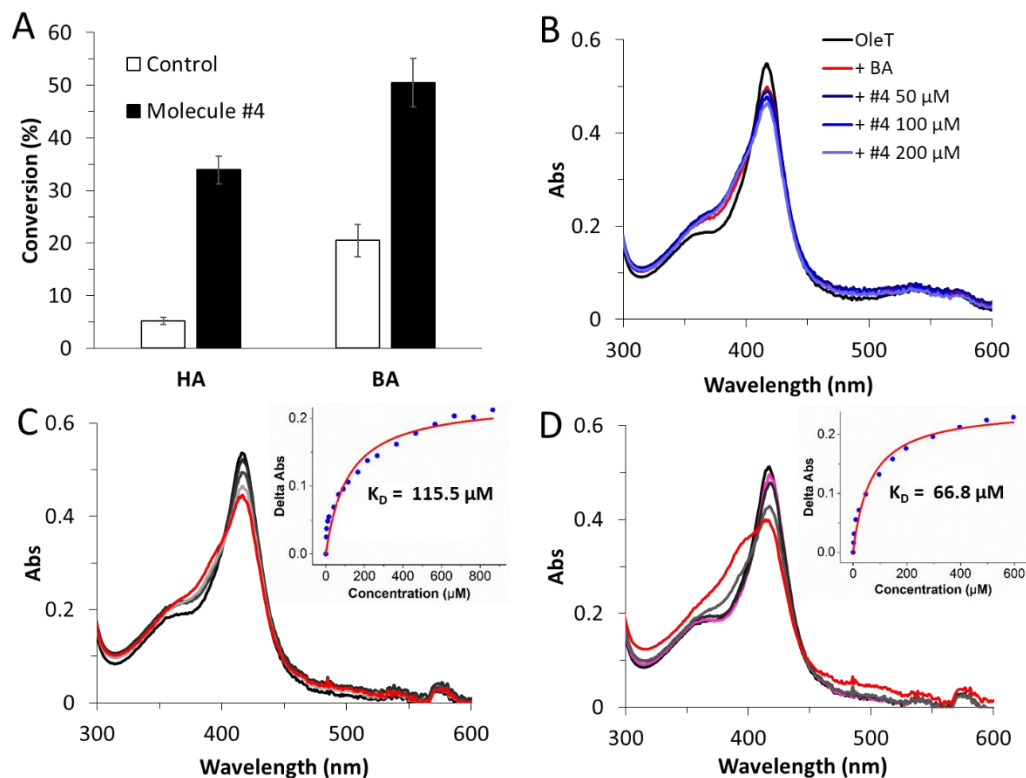


**Figure 4.15** (A) Molecule **4** increases OleT activity on hydrocinnamic acid (HA) and bromophenyl propionic acid (BA) as substrates. OleT$_{SA}$ (5 μM), **4 (**1 mM), substrate (1 mM), and H$_2$O$_2$ (2 mM) were incubated at room temperature for 10 min. The reactions without **4** were carried out as controls. Error bars indicate the standard deviation of duplicate experiments (n = 2). (B) BA (50 μM) and **4** demonstrate cooperativity in binding spectra. (C) UV-Vis binding titration of BA with OleT and the dissociation constant calculation. (D) UV-Vis binding titration of BA with OleT in the presence of **4** (200 μM) and the dissociation constant calculation.

116
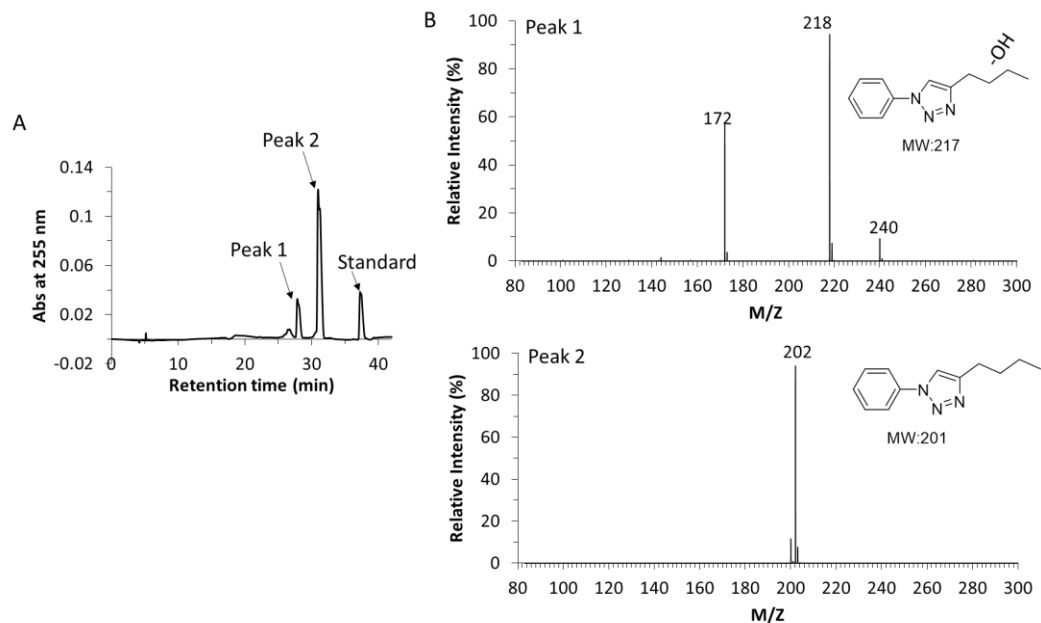
**Figure 4.16** (A) LC spectrum of metabolized **3** by OleT$_{SA}$. Reaction condition: 0.5 mM **4**, 5 μM OleT$_{SA}$, 2 mM H$_2$O$_2$, incubation at room temperature for 30 min. 1,2,3,4-tetrametyl benzene was used as standard. (B) Hydroxylated product was identified by mass spectrometry analysis (Top). The mass spectrometry analysis of Molecule **3** is shown (Bottom) Further characterization of the product is undergoing in our lab.

## 4.3.4 THE ORIGINS OF THE OLET$_{SA}$ ACTIVITY ENHANCEMENT ANALYSIS

The shift of heme spectrum of low-spin state enzyme (**Figure 4.12B**) caused by the small molecules suggesting that these small molecules could alter the heme/H$_2$O local environment, from which the enzyme could be readily oxidized by H$_2$O$_2$ for its catalysis (Figure 4.1). It is possible that the reactivity between heme and H$_2$O$_2$ is altered by the small molecule, which facilitates the enzyme's catalysis. The improved efficiency in this step further releases the oxidative stress caused by excess of H$_2$O$_2$. Both effects could contribute to the apparent enzymatic activity. To identify this possibility, a H$_2$O$_2$ titration assay was done in the presence and absence of **3**. As shown in **Figure 4.17A**, the optimal concentration of H$_2$O$_2$ for OleT$_{SA}$ activity was 2 mM. With increasing concentration of H$_2$O$_2$, OleT$_{SA}$ showed decreased activity because of the oxidative toxicity of H$_2$O$_2$. Clearly

117

the enhanced effect of the small molecule was highly related to the $H_2O_2$ concentration.

For example, when 0.2 mM $H_2O_2$ was used, only around 20% enhancement was obtained

in the presence of 2 mM of **3**. With increasing $H_2O_2$ concentration up to 30 mM, 6 to 50-

fold enhancement was observed. It suggests that the toxicity of $H_2O_2$ to OleT$_{SA}$ enzyme

can be dramatically inhibited by small molecules indicating an oxidative stress releasing

involved mechanism. In Chapter 2, we utilized GOx and glucose to develop an in situ $H_2O_2$

generating method to optimize the OleT catalytic efficiency by minimizing $H_2O_2$ toxicity.

With this method, the small molecule dependent enhancement on the enzyme catalytic

efficiency was diminished (**Figure 4.17B**) further supporting our hypothesis that the origin

of the enhancement of small molecules is from enzyme oxidative step.
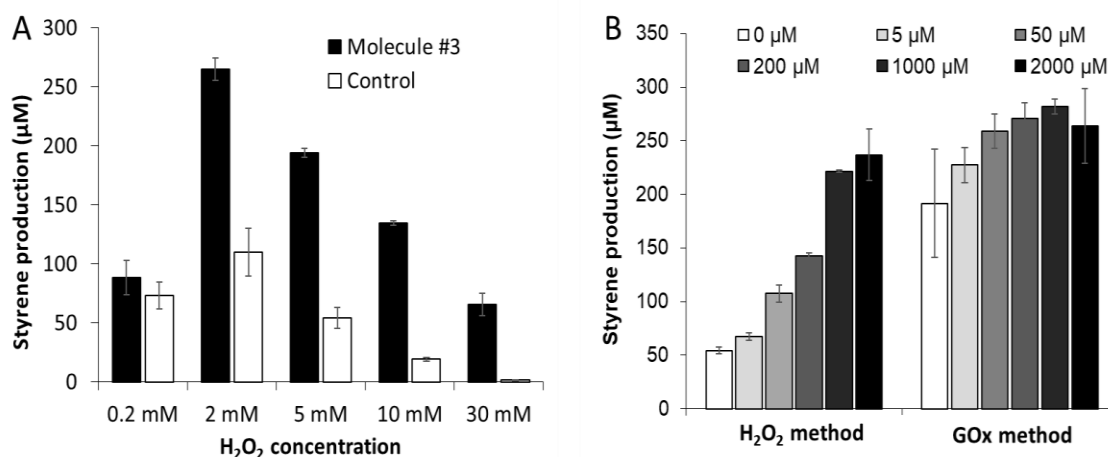


**Figure 4.17** (A) Molecule **3** stimulates OleT enzymatic activity in the presence of high $H_2O_2$ concentration. Reactions were performed with 5 µM OleT$_{SA}$, 2 mM **3**, 2 mM HA and different concentration of $H_2O_2$ for 1h reaction at room temperature. (B) The enhanced effect of **3** on OleT catalytic efficiency is diminished with an $H_2O_2$ in-situ release process (GOx method). One-time addition of $H_2O_2$ (2 mM) was used in $H_2O_2$ method. GOx (300 nM) and glucose (6.6 mM) were used in GOx method. In all conditions, 5 µM OleT$_{SA}$, 1 mM HA, 1-hour reaction at room temperature were used in all conditions. Error bars indicate the standard deviation of duplicate experiments (n = 2).

4.4 CONCLUSION

In summary, we report to use small molecules to leverage P450 OleT$_{SA}$

enzymatic catalysis. Though only a small scale of molecules explored in this work,

up to 6-fold enhanced OleT enzymatic activity have been obtained. We found that the small molecules and enzyme substrates could reside in the enzyme active site simultaneously, and proposed the origins of the enhancement were from the enzyme oxidation step and an $H_2O_2$ toxicity inhibiting effect. Our work sheds the light to the application of small molecules to increase OleT catalytic efficiency, which could be potentially used for future olefin-production applications. However, further mechanistic investigation, especially on the enzyme-small molecule-substrate complex structure data, is necessary to better understand the system. It may also provide direct evidence and useful information for the design of next generation activators.

## 4.5 REFERENCES

(1)     Aransiola, E. F.; Ojumu, T. V.; Oyekola, O. O.; Madzimbamuto, T. F.; Ikhu-Omoregbe, D. I. O. A Review of Current Technology for Biodiesel Production: State of the Art. *Biomass Bioenergy* **2014**, *61*, 276–297.

(2)     Das, S.; Join, B.; Junge, K.; Beller, M. A General and Selective Copper-Catalyzed Reduction of Secondary Amides. *Chem. Commun.* **2012**, *48* (21), 2683–2685.

(3)     Das, S.; Möller, K.; Junge, K.; Beller, M. Zinc-Catalyzed Chemoselective Reduction of Esters to Alcohols. *Chem. Eur. J.* **2011**, *17* (27), 7414–7417.

(4)     Robles-Medina, A.; González-Moreno, P. A.; Esteban-Cerdán, L.; Molina-Grima, E. Biocatalysis: Towards Ever Greener Biodiesel Production. *Biotechnol. Adv.* **2009**, *27* (4), 398–408.

(5)     Dennig, A.; Kurakin, S.; Kuhn, M.; Dordic, A.; Hall, M.; Faber, K. Enzymatic Oxidative Tandem Decarboxylation of Dioic Acids to Terminal Dienes. *Eur J Org Chem* **2016**, *2016* (21), 3473–3477.

(6)     Qiu, Y.; Tittiger, C.; Wicker-Thomas, C.; Le Goff, G.; Young, S.; Wajnberg, E.; Fricaux, T.; Taquet, N.; Blomquist, G. J.; Feyereisen, R. An Insect-Specific P450 Oxidative Decarbonylase for Cuticular Hydrocarbon Biosynthesis. *Proc. Natl. Acad. Sci. U.S.A.* **2012**, *109* (37), 14858–14863.

(7)      Schirmer, A.; Rude, M. A.; Li, X.; Popova, E.; Cardayre, S. B. del. Microbial Biosynthesis of Alkanes. *Science* **2010**, *329* (5991), 559–562.

(8)      Rui, Z.; Harris, N. C.; Zhu, X.; Huang, W.; Zhang, W. Discovery of a Family of Desaturase-Like Enzymes for 1-Alkene Biosynthesis. *ACS Catal.* **2015**, *5* (12), 7091–7094.

(9)      Kallio, P.; Pásztor, A.; Thiel, K.; Akhtar, M. K.; Jones, P. R. An Engineered Pathway for the Biosynthesis of Renewable Propane. *Nat Commun* **2014**, *5*, 1–8.

(10)     Rude, M. A.; Baron, T. S.; Brubaker, S.; Alibhai, M.; Cardayre, S. B. D.; Schirmer, A. Terminal Olefin (1-Alkene) Biosynthesis by a Novel P450 Fatty Acid Decarboxylase from Jeotgalicoccus Species. *Appl. Environ. Microbiol.* **2011**, *77* (5), 1718–1727.

(11)     Lu, C.; Shen, F.; Wang, S.; Wang, Y.; Liu, J.; Bai, W.-J.; Wang, X. An Engineered Self-Sufficient Biocatalyst Enables Scalable Production of Linear α-Olefins from Carboxylic Acids. *ACS Catal.* **2018**, *8* (7), 5794–5798.

(12)     Dennig, A.; Kuhn, M.; Tassoti, S.; Thiessenhusen, A.; Gilch, S.; Bülter, T.; Haas, T.; Hall, M.; Faber, K. Oxidative Decarboxylation of Short-Chain Fatty Acids to 1-Alkenes. *Angew Chem Int Ed* **2015**, *54* (30), 8819–8822.

(13)     Wise, C. E.; Hsieh, C. H.; Poplin, N. L.; Makris, T. M. Dioxygen Activation by the Biofuel-Generating Cytochrome P450 OleT. *ACS Catal.* **2018**, 9342–9352.

(14)     Grant, J. L.; Hsieh, C. H.; Makris, T. M. Decarboxylation of Fatty Acids to Terminal Alkenes by Cytochrome P450 Compound I. *J. Am. Chem. Soc.* **2015**, *137* (15), 4940–4943.

(15)     Grant, J. L.; Mitchell, M. E.; Makris, T. M. Catalytic Strategy for Carbon−carbon Bond Scission by the Cytochrome P450 OleT. *PNAS* **2016**, *113* (36), 10049–10054.

(16)     Munro, A. W.; McLean, K. J.; Grant, J. L.; Makris, T. M. Structure and Function of the Cytochrome P450 Peroxygenase Enzymes. *Biochem. Soc. Trans.* **2018**, *46* (1), 183–196.

(17)     Matthews, S.; Tee, K. L.; Rattray, N. J.; McLean, K. J.; Leys, D.; Parker, D. A.; Blankley, R. T.; Munro, A. W. Production of Alkenes and Novel Secondary Products by P450 OleTJE Using Novel H2O2-Generating Fusion Protein Systems. *FEBS Lett.* **2017**, *591* (5), 737–750.

(18)     Zachos, I.; Gaßmeyer, S. K.; Bauer, D.; Sieber, V.; Hollmann, F.; Kourist, R. Photobiocatalytic Decarboxylation for Olefin Synthesis. *Chem. Commun.* **2015**, *51* (10), 1918–1921.

(19)    Amaya, J. A.; Rutland, C. D.; Makris, T. M. Mixed Regiospecificity Compromises Alkene Synthesis by a Cytochrome P450 Peroxygenase from Methylobacterium Populi. *J. Inorg. Biochem.* **2016**, *158*, 11–16.

(20)    Amaya, J. Mechanisms of Decarboxylation in The CYP152 Family of Cytochrome P450S. *Theses and Dissertations* **2018**.

(21)    Jiang, Y.; Li, Z.; Wang, C.; Zhou, Y. J.; Xu, H.; Li, S. Biochemical Characterization of Three New α-Olefin-Producing P450 Fatty Acid Decarboxylases with a Halophilic Property. *Biotechnol. Biofuels* **2019**, *12* (1), 79.

(22)    Wang, J.; Lonsdale, R.; Reetz, M. T. Exploring Substrate Scope and Stereoselectivity of P450 Peroxygenase OleTJE in Olefin-Forming Oxidative Decarboxylation. *Chem. Commun.* **2016**, *52* (52), 8131–8133.

(23)    Hsieh, C. H.; Makris, T. M. Expanding the Substrate Scope and Reactivity of Cytochrome P450 OleT. *Biochem. Biophys. Res. Commun* **2016**, *476* (4), 462–466.

(24)    Matthews, S.; Belcher, J. D.; Tee, K. L.; Girvan, H. M.; McLean, K. J.; Rigby, S. E. J.; Levy, C. W.; Leys, D.; Parker, D. A.; Blankley, R. T.; et al. Catalytic Determinants of Alkene Production by the Cytochrome P450 Peroxygenase OleTJE. *J. Biol. Chem.* **2017**, *292* (12), 5128–5143.

(25)    Amaya, J. A.; Rutland, C. D.; Leschinsky, N.; Makris, T. M. A Distal Loop Controls Product Release and Chemo- and Regioselectivity in Cytochrome P450 Decarboxylases. *Biochemistry* **2018**, *57* (3), 344–353.

(26)    Hummel, M. A.; Gannett, P. M.; Aguilar, J. S.; Tracy, T. S. Effector-Mediated Alteration of Substrate Orientation in Cytochrome P450 2C9. *Biochemistry* **2004**, *43* (22), 7207–7214.

(27)    Cameron, M. D.; Wen, B.; Roberts, A. G.; Atkins, W. M.; Patricia Campbell, A.; Nelson, S. D. Cooperative Binding of Acetaminophen and Caffeine within the P450 3A4 Active Site. *Chem. Res. Toxicol.* **2007**, *20* (10), 1434–1441.

(28)    Mast, N.; Verwilst, P.; Wilkey, C. J.; Guengerich, F. P.; Pikuleva, I. A. In Vitro Activation of Cytochrome P450 46A1 (CYP46A1) by Efavirenz-Related Compounds. *J. Med. Chem.* **2019**. doi.org/10.1021/acs.jmedchem.9b01383.

(29)    Shoji, O.; Aiba, Y.; Watanabe, Y. Hoodwinking Cytochrome P450BM3 into Hydroxylating Non-Native Substrates by Exploiting Its Substrate Misrecognition. *Acc. Chem. Res.* **2019**, *52* (4), 925–934.

(30)    Wang, M.; Baaden, M.; Wang, J.; Liang, Z. A Cooperative Mechanism of Clotrimazoles in P450 Revealed by the Dissociation Picture of Clotrimazole from P450. *J. Chem. Inf. Model.* **2014**, *54* (4), 1218–1225.

(31)    Hsieh, C. H.; Huang, X.; Amaya, J. A.; Rutland, C. D.; Keys, C. L.; Groves, J. T.; Austin, R. N.; Makris, T. M. The Enigmatic P450 Decarboxylase OleT Is Capable of, but Evolved To Frustrate, Oxygen Rebound Chemistry. *Biochemistry* **2017**, *56* (26), 3347–3357.

(32)    Liu, Y.; Han, C.; Ma, X.; Yang, J.; Feng, X.; Jiang, Y. One-Pot Synthesis of 1-Monosubstituted-1, 2, 3-Triazoles from 2-Methyl-3-Butyn-2-Ol. *Tetrahedron Letters* **2018**, *59* (7), 650–653.

(33)    Luthra, A.; Denisov, I. G.; Sligar, S. G. Spectroscopic Features of Cytochrome P450 Reaction Intermediates. *Arch Biochem Biophys* **2011**, *507* (1), 26–35.

CHAPTER 5

# BIPHASIC CATALYSIS USING SURFACTANT ASSISTED ENZYME BASED

# INTERFACIAL ASSEMBLY FOR TERMINAL ALKENE PRODUCTION

## 5.1 INTRODUCTION

Organic-aqueous biphasic catalysis is an important process in chemical industry because it provides a way of heterogenizing the catalysts and substrates/products into two immiscible phases, which are ready for separation and purification.[1,2] This process is particularly useful for enzyme based synthesis because enzymes prefer aqueous media like that in natural environment, while many substrates/products (e.g. lipids, fatty acids, alkenes) have limited solubility in water.[3] The organic-aqueous biphasic catalysis represent a promising strategy to address these limitations. The slow mass transportation due to the small interfacial areas in the biphasic reactions will, however, significantly reduce the enzymatic reaction rates. A versatile method to address this problem is to create an emulsion (i.e. classical emulsion, Pickering emulsion) with aqueous phase containing catalysts and organic phase containing the substrates and /or products.

A classical emulsion (as shown in **Figure 5.1A**) is to introduce surfactants or surface-active polymers (i.e. polymers with amphiphilic properties) to stabilize dispersions in aqueous or non-aqueous media.[4] The hydrophile-lipophile balance (HLB) number, the packing parameter setting by geometry of the surfactant molecules, and the extent of hydration/solvation by separated phase are important variables in determining whether aggregated surfactant (micelles or emulsion droplets) resides in either water, oil, or a third phase.[5] With selected surfactants and well-designed polymers, some examples of enzymatic reactions conducted in emulsions or reverse micelles as 'nanoreactor' have been reported.[6–9] The increased interfacial area of different phases and improved stability of enzymes encapsulated in the emulsion droplets were attributed to the advanced catalytic efficiency.

124

Solid nano- or microparticles can function in similar ways as surfactants to form emulsions, which was firstly reported by Picking and Ramsden[10] about a century ago and thus known as Pickering emulsions (**Figure 5.1B**). One key relevant parameter determining Pickering emulsion type is the contact angle (θ), which the particle makes with the interface determined by the partial wettability of the solid by different phases.[5,11,12] Pickering emulsion does not require surfactants that often show adverse effects on enzymes' functionality (for example through irritancy, hemolytic behavior), but retains the basic properties of classical emulsions. Pickering emulsions are usually much smaller than classical emulsions depending on the size of solid particles. Recently, increasing attentions have been given to use Pickering emulsion for enzymatic biphasic catalysis,[13–16] which demonstrated superior catalytic efficiency compared to conventional biphasic reactions. Besides solid particles, we and others have established that bionanoparticles such as plant viruses, bacterial phages and ferritins can also be used for Pickering emulsions to generate droplets or nanoparticles through interfacial assembly.[11,17,18]
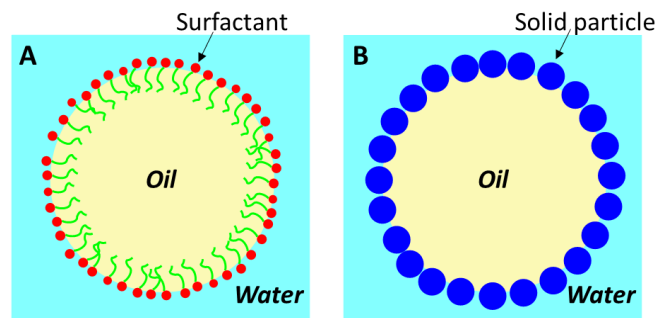


**Figure 5.1** Schematic illustration of classical (surfactant-based) emulsion (A) and a Pickering emulsion (B). Both represent oil-in-water type.

Many proteins are surface-active molecules because of their amphiphilic nature which makes them a logic choice as emulsifiers/stabilizers of emulsions. In particular, some milk proteins (e.g. β-lactoglobulin and β-casein) have been widely used in food

125

emulsions.[19] However, due to a dramatic change of the polarity in environment, many proteins could lose part of their tertiary structural features upon adsorption to the oil/water interface and generate considerable amounts of non-native secondary structures.[20] Except of some special interface-activating enzymes (e.g. lipase),[21] it is a challenge to employ functional proteins (e.g. enzymes) directly as the 'emulsifier' for emulsion formation. In our previous study, we utilized co-assembly strategy to generate polymer-protein core shell nanoparticles, in which enzymes, playing a surfactant-like role, adsorbed on the polymeric surface and stabilized the nanosturcutre.[22,23] Some efforts have been placed to utilize the polymers to modulate enzymes' surface properties in order to facilitate emulsions forming and maintain enzymes' function in a harsh environment.[15,24,25]

P450 OleT$_{SA}$ enzyme[26] catalyzes the conversion of fatty acids to terminal alkenes using hydrogen peroxide as a cofactor through a single step of decarboxylation. This process has attracted broad interests for the sustainable production of fuels that are compatible with the existing energy infrastructure.[27–29] However, the practical application of this enzyme is hampered by its sluggish turnover rate primarily due to the oxidative damage of the heme prosthetic group by the excess $H_2O_2$ or the derivatized oxidative species.[30] We tried to circumvent this oxidative side reaction by a glucose oxidase (GOx) enzyme based $H_2O_2$ in situ generating method, which has been described in Chapter 2. On the other hand, the low solubility of substrate, i.e. fatty acids, in water is another important factor limiting the synthetic application of this enzyme in conversional monophasic reactions. In this chapter, we explored a surfactant-assisted emulsion process to study OleT$_{SA}$ involved biphasic catalysis for fatty acid decarboxylation applications (**Scheme 5.1**).

Surfactants are amphiphilic compounds that lower the interfacial tension between organic and aqueous phases which have been widely used as emulsifiers, foaming agents, and dispersants in industry and research.[31] The decoration of surfactant on nanoparticles[32] and proteins[33,34] modulates their surface wetting properties and thus trigger interfacial assembly to form emulsions. In this work, we screened a list of surfactants, and revealed that the interaction between sodium dodecyl sulfate (SDS) and OleT$_{SA}$ can significantly facilitate the emulsion droplet formation. We hypothesize that the SDS modified enzymes acting as surface-active particles absorb on the oil/water interface via interfacial assembly, a similar process to the formation of Pickering emulsion.

In the biphasic catalytic reactions, fatty acids were dissolved in the oil phase. Equal amounts of SDS modify OleT$_{SA}$ and GOx enzyme were used to form emulsions, and D-mannose was added to initiate the tandem catalysis. We found that in the emulsion based biphasic reactions, the production of terminal alkene is comparable to that in conventional enzymatic reactions in aqueous solution, and above 96% of alkene product was enriched in organic layer. Overall, this surfactant-assisted enzyme based emulsion system represents an efficient method for biphasic catalysis and could be applied for enzyme based synthesis.
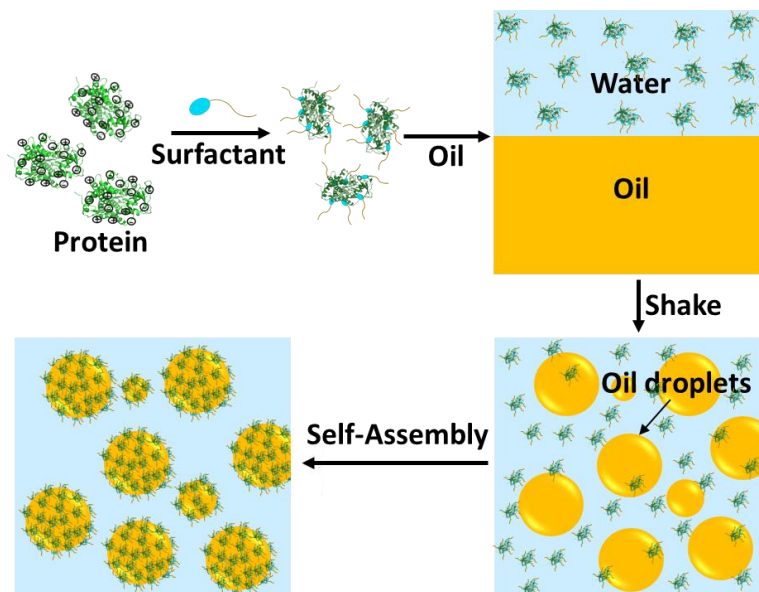
**Scheme 5.1** Schematic illustration of the of protein/surfactant complex formation, the self-assembly of protein/surfactant complex to generate emulsions.

## 5.2. EXPERIMENTAL DETAILS

### 5.2.1. MATERIALS

Eicosanoic acid (C20:0), stearic acid (C18:0), SDS and hexane were purchased from BDH Chemicals. Cetrimonium bromide (CTAB), dodecyltrimethylammonium bromide (DTAB), sodium Bis(2-ethylhexyl) sulfosuccinate (AOT), Trion X -100 and 1-hexadecene was purchased from TCI chemicals. GOx from *Aspergillus niger* and $H_2O_2$ were purchased from Sigma. D-Glucose was purchased from Fisher. All chemicals and solvents used were of analytical grade and were used as received from commercial sources. 200 mM $K_2HPO_4$, 100 mM NaCl, pH 7.4 was used as buffer A unless otherwise noted.

### 5.2.2. PROTEIN EXPRESSION AND PURIFICATION

The protein expression and purification process is the same as described in Chapter 2. Briefly, the kanamycin-resistant plasmid T5 containing a $OleT_{SA}$-$His_6$ gene was transformed BL21(DE3) containing the chloramphenicol-resistant pTF2 plasmid encoding

for GroEL/GroES/Tig chaperones. A modified Terrific Broth (TB) (24 g/L yeast extract, 12 g/L tryptone, 4 g/L peptone) supplemented with 50 μg/mL kanamycin and 20 μg/mL chloramphenicol was used for culturing. 125 mg/L thiamine, and trace metals, 100 μM IPTG, 10 ng/mL tetracycline and 10 mg/L of 5-aminolevulinic acid were added for protein expression, which was done at 18 °C for 16-18 h.[26] The protein was purified using nickel-nitriloacetic acid (Ni-NTA) affinity chromatography followed by Butyl-S-Sepharose column polishing step. Fractions with an Rz value (Abs418 nm/Abs280 nm) above 1.2 were pooled and dialyzed against 200 mM KPi pH 8. Proteins were stored at -80 °C until further use.[26]

### 5.2.3. EMULSIONS GENERATION VIA INTERFACIAL ASSEMBLY

The surfactants were dissolved in $H_2O$ (unless otherwise noted), then mixed with protein(s) solution, and incubated at room temperature for 10 min. Generally, the final concentration of surfactants used is lower than their critical micelle concentration (CMC, unless otherwise noted, see **Table 5.1**). Then equal volume of hexane was added into the above solution in a 1.5 mL tube. Shake the mixture by hand for several minutes to generate emulsions. For example, for SDS assisted enzyme emulsion formation, 150 μL of 6 mM SDS in $H_2O$ was mixed with 150 μL of 10 μM OleT$_{SA}$ in buffer A in a 1.5 mL tube and incubated for 10 minutes at room temperature before 300 μL hexane was added. The mixture was shaken gently for 1-3 minutes for emulsion formation. The emulsions were not purified for further characterization.

## 5.2.4 CHARACTERIZATION OF THE PROTEIN-SDS INTERACTION AND EMULSIONS

Fluorescent spectrum of OleT enzyme solution in the presence and absence of surfactant was measured by Varian Eclipse fluorescence spectrophotometer. The zeta potential was measured with dynamic light scattering (DLS, Zetasizer Nano ZS, Malvern Instruments). UV-Visible spectroscopy on an HP 8453 spectrophotometer and a quartz cuvette with 1 cm path length were used for UV-Vis test. For confocal imaging, EGFP/SDS solution was used as aqueous phase, hexane was used as organic phase for emulsion generation, excited at 488 nm. An organic soluble dye Nile red was used to stain the oil phase of $OleT_{SA}$/SDS emulsions.

## 5.2.5 ENZYMATIC REACTION IN BIPHASIC CATALYSIS AND THE ACTIVITY TEST

Aqueous solution (300 μL) including 5 μM $OleT_{SA}$, 5 μM GOx and 0.3 mM SDS in buffer A was incubated at room temperature for 10 minutes in a 1.5 mL Eppendorf tube. Hexane (300 μL) with 4 mM eicosanoic acid was used as the organic solution, which was added into the above aqueous solution in the tube and shaken for several minutes. D-Mannose was added to initiate the reaction (the final concentration was controlled at 7 mM). After 60 minutes' reaction, the emulsion phase and aqueous phase were separated into two 1.5 mL tubes. 10% HCL was added to quench the reactions. Then internal standard was added. For emulsion phase, centrifuge at 14000 g for 2 minutes to breakdown the oil drops and run the sample on GC. For aqueous phase, use the same volume of chloroform for extraction, run the chloroform layer on GC.

130

## 5.3. RESULT AND DISCUSSION

### 5.3.1. SURFACTANT SELECTION

Surfactants with opposite charge to proteins have been reported to interact with proteins through electrostatic interactions for interfacial assembly study.[34] In this work, we expanded the selection range and included different types of surfactants in order to identify the suitable one interacting with the $OleT_{SA}$ to form emulsion efficiently while sustaining enzyme activity (**Table 5.1**). We found that both negative and positive charged surfactants could facilitate the $OleT_{SA}$ based emulsion formation, though the emulsion droplet size and stability could be varied depending on the charge, size and other properties of individual surfactant. Among them, SDS was chosen because the interaction between SDS and $OleT_{SA}$ significantly facilitated the emulsions' formation and stabilization.

### 5.3.2. OLET_{SA} SDS INTERACTION CHARACTERIZATION
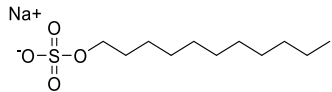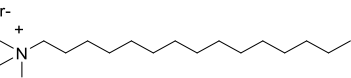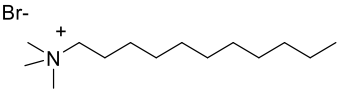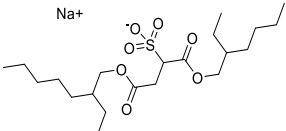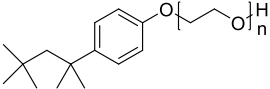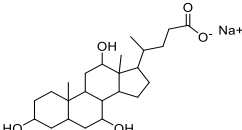
The interaction between SDS and denatured proteins has been well established. For example, high concentration of SDS (e.g. 80 mM ) was used to coat denatured proteins and mask its intrinsic charge for SDS-PAGE analysis.[35] We tested different concentration of SDS (**Table 5.1**) and figured out that 60:1 (e.g. 0.3 mM SDS and 5 μM OleT) was the optimal ratio to facilate the emulsion formation while with the enzyme activity susained. As shown in **Figure 5.2A**, the florscence spectrum of $OleT_{SA}$ did not change after SDS treating suggesting sustained enzyme conformation. An obvious heme spectrum shift was observed with SDS treatment indicating that some SDS molecules entered into the enzyme active center interferring the spin state of heme (**Figure 5.2B**). However, this effect did not influence enzyme activity significantly (**Figure 5.2C**). Formation of the $OleT_{SA}$/SDS complex was confirmed by the change of zeta potential from -7.5 to -10.3 after a SDS

131

treatment. Moreover, higher concentration of slat may interupt the enzyme/SDS interaction and interfer the complex formation (**Figure 5.2D**). This is consistent with our hypothesis that the negative charged SDS can interact with the positive residues on OleT surface, thus decreased its zeta potential.

## 5.3.2. INTERFACIAL ASSEMBLY OF OLET$_{SA}$-SDS TO FORM EMULSIONS AND ITS CHARACTERIZATION

Hexane as oil phase and OleT$_{SA}$/SDS dissolved in aqueous phase were used to generate microemulsions via interfacial assembly. As describe above, equal volume of hexane was added into Ole/SDS solution, with gentle shaking by hand, emulsions could be obtained. As controls, OleT enzyme only solution or SDS only solution, there was not obvious and stable emulsions formed (**Figure 5.3A**). These results further confirmed that the modification of OleT by SDS is key for a successful emulsion formation (likely due to the partial hydrophobilized effect). As shown in **Figure 5.3B**, the droplet size range of modified OleT/hexane emulsions was from ~50 – 300 μm. To visualize the type of emulsions, we applied water-immiscible Nile Red to stain the organic phase, in which red fluorescence only appeared in droplets indicating that oil-in-water (O/W) emulsions were formed (**Figure 5.3C**). In addition, we used EGFP protein solution to carry out a similar emulsion process in hexane. As expected, green emission was only observed in the continuous phase (**Figure 5.3D**). Based on above results, an oil-in-water (O/W) emulsion forming process via interfacial assembly was proposed and shown in **Scheme 5.1**.

**Table 5.1** Surfactants used to test emulsion formation

| Surfactant name | Structure | CMC (mM)* | Tested Conc. (mM) | Emulsion Formation (Y/N) |
|---|---|---|---|---|
| SDS |  | 8.2 | 0.01 – 3 | Y |
| CTAB |  | 1.0 | 2.0 | Y |
| DTAB |  | 14.5 | 3.0 | Y |
| AOT |  | 2.1 | 1.0 and 7.0 | N |
| Trion X - 100 |  | 2.4 | 2.0 | NA |
| Sodium Cholate |  | 14.0 | 10.0 | Y |

Note: OleT$_{SA}$ (5 µM) as aqueous solution and hexane as organic phase were used for all tests. *CMC value is based on reported data at 25 °C in water.[36,37] NA: Surfactant itself can form emulsion with hexane. So the effect of the surfactant cannot determined
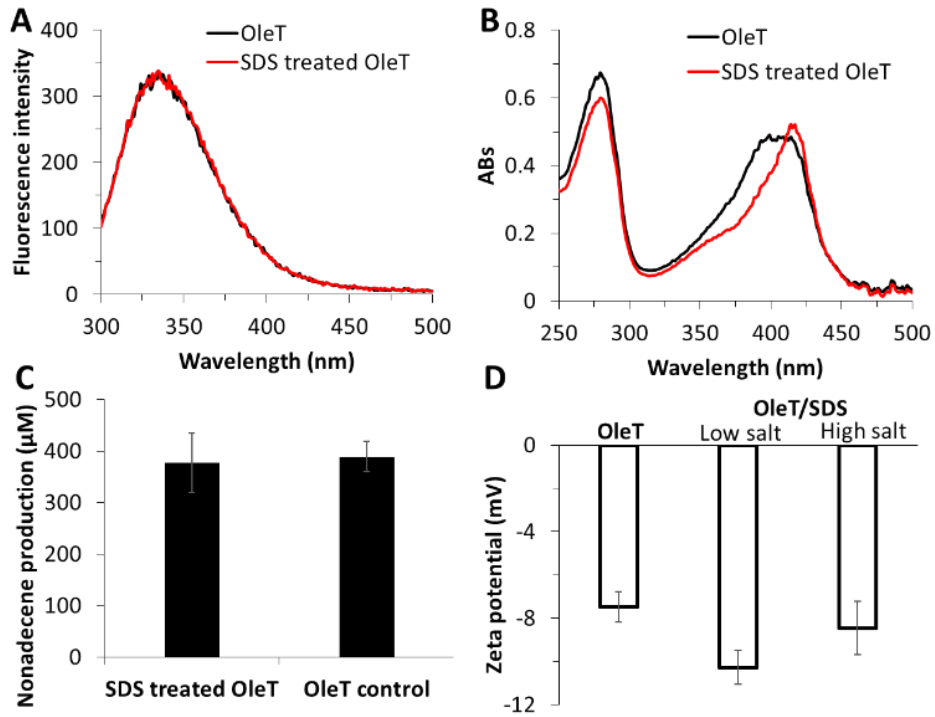
**Figure 5.2** (A) Fluorescence spectrum of OleT$_{SA}$ enzyme and SDS treated OleT$_{SA}$ enzyme excited at 280 nm. (B) UV-Vis spectrum of OleT$_{SA}$ and SDS treated OleT$_{SA}$. (C) Activity comparison of OleT and SDS treated OleT$_{SA}$. SDS treated OleT$_{SA}$ or free OleT$_{SA}$ (5 μM), eicosanoic acid (1 mM), GOx (5 μM), mannose (7 mM) were incubated at room temperature for 60 minutes. (D) Zeta potential test of OleT solution and SDS treated OleT solution with two different buffers. For 'low salt' sample: 100 mM K$_2$HPO$_4$, 50 mM NaCl, pH 7.4 was used for SDS/OleT$_{SA}$ incubation. For 'high salt' sample: 100 mM K$_2$HPO$_4$, 50 mM NaCl, pH 7.4 was used for SDS/OleT$_{SA}$ incubation. For all SDS treated samples, SDS (0.3 mM) and OleT (5 μM) was incubated at room temperature for 10 minutes.
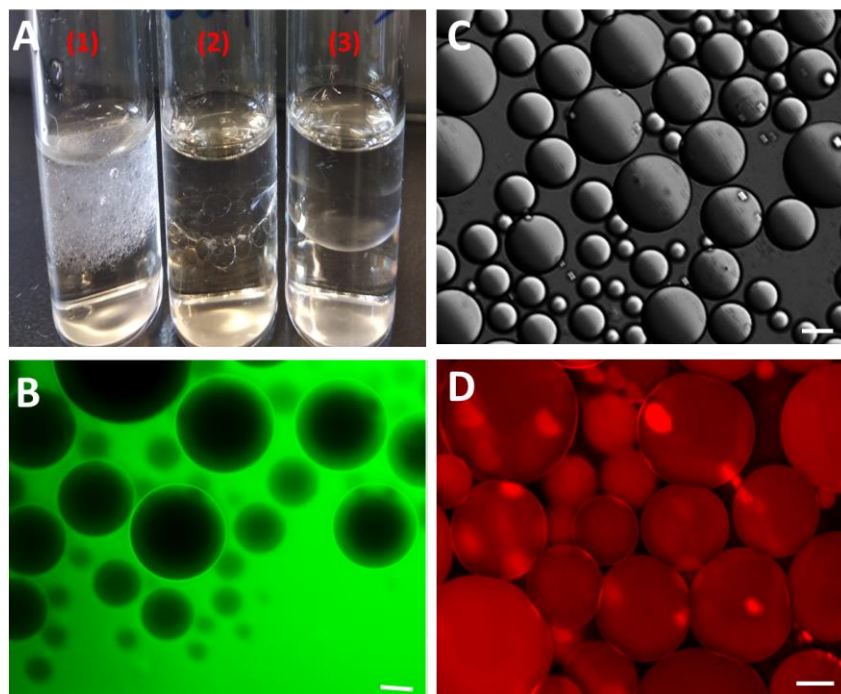
**Figure 5.3** (A) Photographs of hexane/water Pickering emulsions. Shaking of SDS solution and hexane (1) or protein solution and hexane (3) do not form emulsions, while shaking of SDS/protein solution and hexane form emulsions easily. (B) Fluorescence microscopy images of EGFP/SDS stabilized Pickering emulsion with emission of 488 nm. (C) optical microscopy of OleT$_{SA}$/SDS. (D) Fluorescence microscopy images of OleT$_{SA}$/SDS stabilized Pickering emulsion with oil-soluble Nile red. Scale bars: 100 μm.

### 5.3.3. BIPHASIC CATALYSIS USING OLET-SDS/HEXANE OIL-IN-WATER EMULSIONS

OleT enzyme-based catalysis is hampered by the poor solubility of substrates (i.e. fatty acids) and products (i.e. terminal alkene). Furthermore, the inefficient product purification step (for example extraction) is also a major obstacle for its real synthetic application. Fortunately, both the fatty acids and terminal alkene products have high solubility in hexane and other organic solvents. Herein, we propose to use the emulsion based biphasic approach to optimize the OleT catalysis. In Chapter 2, we described a H$_2$O$_2$ in situ generation method to improve OleT catalysis with coupling to GOx enzyme. Based on a similar process showing in Scheme 1, a multienzyme based oil-in-water emulsion process was carried out.

In this study, 4 mM eicosanoic acid (C20 FA) was dissolved in hexane as organic phase. An OleT-SDS and GOx-SDS enzyme mixture was used as aqueous phase. With following a gentle shaking by hand, the GOx-SDS/OleT-SDS droplets were formed (**Figure 5.4A**). D-mannose (7 mM) as GOx substrate was added to initiate the tandem catalysis. Nonadecene product was calculated in both oil and aqueous phase after the reaction. As shown in **Figure 5.4B** and **5.4C**, we found that the produced alkene in the biphasic reaction was comparable to that in conventional one-phase enzymatic reactions, while above 96% of the product was enriched in organic phase showing unparalleled advantages. It is noteworthy that though the alkene production obtained in the biphasic reaction was similar to that in conventional enzymatic reaction, the enzyme at the water/oil interface displayed higher activity than that in control samples, because only the portion of enzymes absorbed at the interface contributed the fatty acids conversion, and the free enzymes could not catalyze the conversion due to the separation of substrate in oil phase and the free enzymes in aqueous phase.

136
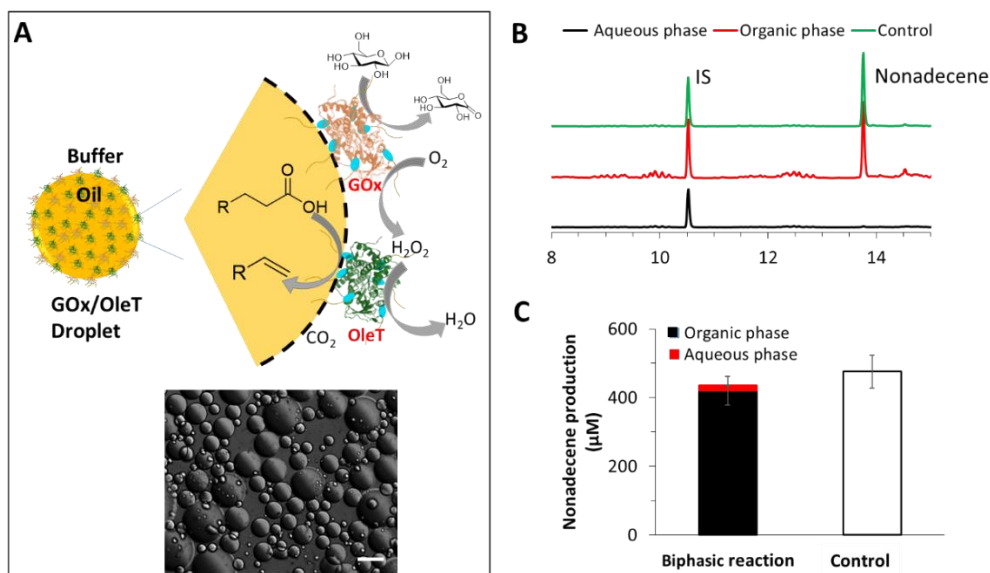
**Figure 5.4** (A) Scheme of OleT$_{SA}$-SDS/GO$_X$-SDS stabilized oil drops and the biphasic catalysis (top) and optical microscopy of OleT$_{SA}$-SDS/GO$_X$-SDS hexane droplet (bottom). Scale bar: 100 μm. (B) GC spectrum of nonadecene product distributed in organic and aqueous phase of the biphasic reaction. A conversional one-phase reaction was used as control. (C) Nonadecene product distribution calculation in the biphasic reactions and the control reaction. Reaction condition: for biphasic reaction, 5 μM of SDS treated OleT and 5 μM SDS treated GOx, 4 mM eicosanoic acid dissolved in hexane, 7 mM mannose, incubation at room temperature for 60 minutes. For control reaction, the same condition as in the biphasic reaction above was used without hexane.

## 5.4 CONCLUSION

In summary, we have demonstrated a surfactant assisted enzyme based interfacial assembly system, in which the modified enzymes serving as 'surface active' particles were utilized to form oil-in-water emulsions. With this model, an efficient biphasic catalysis was carried out. The excellent catalytic efficiency of the emulsions was primarily attributed to the improved interfacial area compared to conventional biphasic reactions. More importantly, more than 96% of terminal alkene product was enriched in the organic phase during the catalysis showing unparalleled advance compared to the conventional enzymatic reactions.

## 5.5 REFERENCES

(1)     Pera-Titus, M.; Leclercq, L.; Clacens, J.-M.; De Campo, F.; Nardello-Rataj, V. Pickering Interfacial Catalysis for Biphasic Systems: From Emulsion Design to Green Reactions. *Angew. Chem. Int.* **2015**, *54* (7), 2006–2021.

(2)     Wachsen, O.; Himmler, K.; Cornils, B. Aqueous Biphasic Catalysis: Where the Reaction Takes Place. *Catal. Today* **1998**, *42* (4), 373–379.

(3)     Cheetham, P. S. J. What Makes a Good Biocatalyst? *J. Biotechnol.* **1998**, *66* (1), 3–10.

(4)     Emulsifiers 101: Who Says Oil and Water Don't Mix?: Full Text Finder Results.

(5)     Binks, B. P. Particles as Surfactants—Similarities and Differences. *Curr. Opin. Colloid Interface Sci.* **2002**, *7* (1), 21–41.

(6)     Gröger, H.; May, O.; Hüsken, H.; Georgeon, S.; Drauz, K.; Landfester, K. Enantioselective Enzymatic Reactions in Miniemulsions as Efficient "Nanoreactors." *Angew. Chem. Int* **2006**, *45* (10), 1645–1648.

(7)     Luethi, P.; Luisi, P. L. Enzymic Synthesis of Hydrocarbon-Soluble Peptides with Reverse Micelles. *J. Am. Chem. Soc.* **1984**, *106* (23), 7285–7286.

(8)     Zhao, Q.; Ansorge-Schumacher, M. B.; Haag, R.; Wu, C. Compartmentalized Aqueous–Organic Emulsion for Efficient Biocatalysis. *Chem. Eur* **2018**, *24* (43), 10966–10970.

(9)     Barros, D. P. de; Pinto, F.; Pfluck, A. C.; Dias, A. S.; Fernandes, P.; Fonseca, L. P. Improvement of Enzyme Stability for Alkyl Esters Synthesis in Miniemulsion Systems by Using Media Engineering. *J. Chem. Technol.* **2018**, *93* (5), 1338–1346.

(10)    Ramsden, W. Separation of Solids in the Surface-Layers of Solutions and "Suspensions" (Observations on Surface-Membranes, Bubbles, Emulsions, and Mechanical Coagulation). Preliminary Account. *Proc. R. Soc. London* **1903**, *72* (479), 156–164.

(11)    Niu, Z.; He, J.; Russell, T. P.; Wang, Q. Synthesis of Nano/Microstructures at Fluid Interfaces. *Angew. Chem. Int* **2010**, *49* (52), 10052–10066.

(12)    Chevalier, Y.; Bolzinger, M.-A. Emulsions Stabilized with Solid Nanoparticles: Pickering Emulsions. *Colloid surface A* **2013**, *439*, 23–34.

(13)     Wei, L.; Zhang, M.; Zhang, X.; Xin, H.; Yang, H. Pickering Emulsion as an Efficient Platform for Enzymatic Reactions without Stirring. *ACS Sustainable Chem. Eng.* **2016**, *4* (12), 6838–6843.

(14)     Yu, S.; Zhang, D.; Jiang, J.; Cui, Z.; Xia, W.; Binks, B. P.; Yang, H. Biphasic Biocatalysis Using a CO2-Switchable Pickering Emulsion. *Green Chem.* **2019**, *21* (15), 4062–4068.

(15)     Pan, Y.; Qiu, W.; Li, Q.; Zhu, S.; Lin, C.; Zeng, W.; Xiong, X.; Liu, X. Y.; Lin, Y. Assembling Two-Phase Enzymatic Cascade Pathways in Pickering Emulsion. *ChemCatChem* **2019**, *11* (7), 1878–1883. https://doi.org/10.1002/cctc.201900098.

(16)     Wang, Z.; van Oers, M. C. M.; Rutjes, F. P. J. T.; van Hest, J. C. M. Polymersome Colloidosomes for Enzyme Catalysis in a Biphasic System. *Angew. Chem. Int* **2012**, *51* (43), 10746–10750.

(17)     Kaur, G.; He, J.; Xu, J.; Pingali, S.; Jutz, G.; Böker, A.; Niu, Z.; Li, T.; Rawlinson, D.; Emrick, T.; Lee, B.; Thiyagarajan, P.; Russell, T. P.; Wang, Q. Interfacial Assembly of Turnip Yellow Mosaic Virus Nanoparticles. *Langmuir* **2009**, *25* (9), 5168–5176.

(18)     Li, T.; Niu, Z.; Emrick, T.; Russell, T. P.; Wang, Q. Core/Shell Biocomposites from the Hierarchical Assembly of Bionanoparticles and Polymer. *Small* **2008**, *4* (10), 1624–1629.

(19)     McClements, D. J. Protein-Stabilized Emulsions. *Curr. Opin. Colloid Interface Sci.* **2004**, *9* (5), 305–313.

(20)     Zhai, J. li; Day, L.; Aguilar, M.-I.; Wooster, T. J. Protein Folding at Emulsion Oil/Water Interfaces. *Curr. Opin. Colloid Interface Sci.* **2013**, *18* (4), 257–271.

(21)     Ortiz, C.; Luján Ferreira, M.; Barbosa, O.; Santos, J. C. S. dos; C. Rodrigues, R.; Berenguer-Murcia, Á.; E. Briand, L.; Fernandez-Lafuente, R. Novozym 435: The "Perfect" Lipase Immobilized Biocatalyst? *Catal. Sci.* **2019**, *9* (10), 2380–2420.

(22)     Suthiwangcharoen, N.; Li, T.; Wu, L.; Reno, H. B.; Thompson, P.; Wang, Q. Facile Co-Assembly Process to Generate Core–Shell Nanoparticles with Functional Protein Corona. *Biomacromolecules* **2014**, *15* (3), 948–956.

(23)     Zhang, L.; Xu, Y.; Makris, T. M.; Wang, Q. Enhanced Arylamine N-Oxygenase Activity of Polymer–Enzyme Assemblies by Facilitating Electron-Transferring Efficiency. *Biomacromolecules* **2018**, *19* (3), 918–925.

139

(24)     Sun, Z.; Glebe, U.; Charan, H.; Böker, A.; Wu, C. Enzyme–Polymer Conjugates as Robust Pickering Interfacial Biocatalysts for Efficient Biotransformations and One-Pot Cascade Reactions. *Angew. Chem. Int* **2018**, *57* (42), 13810–13814.

(25)     Zhu, G.; Wang, P. Polymer−Enzyme Conjugates Can Self-Assemble at Oil/Water Interfaces and Effect Interfacial Biotransformations. *J. Am. Chem. Soc.* **2004**, *126* (36), 11132–11133.

(26)     Amaya, J. Mechanisms of Decarboxylation In The CYP152 Family Of Cytochrome P450S. *Theses and Dissertations* **2018**.

(27)     Kung, Y.; Runguphan, W.; Keasling, J. D. From Fields to Fuels: Recent Advances in the Microbial Production of Biofuels. *ACS Synth. Biol.* **2012**, *1* (11), 498–513.

(28)     Rude, M. A.; Baron, T. S.; Brubaker, S.; Alibhai, M.; Cardayre, S. B. D.; Schirmer, A. Terminal Olefin (1-Alkene) Biosynthesis by a Novel P450 Fatty Acid Decarboxylase from Jeotgalicoccus Species. *Appl. Environ. Microbiol.* **2011**, *77* (5), 1718–1727.

(29)     Wise, C. E.; Hsieh, C. H.; Poplin, N. L.; Makris, T. M. Dioxygen Activation by the Biofuel-Generating Cytochrome P450 OleT. *ACS Catal.* **2018**, 9342–9352.

(30)     Munro, A. W.; McLean, K. J.; Grant, J. L.; Makris, T. M. Structure and Function of the Cytochrome P450 Peroxygenase Enzymes. *Biochem. Soc.* **2018**, BST20170218.

(31)     Surfactants and Interfacial Phenomena, 4th Edition | Wiley (accessed Feb 24, 2020).

(32)     Maestro, A.; Deshmukh, O. S.; Mugele, F.; Langevin, D. Interfacial Assembly of Surfactant-Decorated Nanoparticles: On the Rheological Description of a Colloidal 2D Glass. *Langmuir* **2015**, *31* (23), 6289–6297.

(33)     Tucker, I. M.; Petkov, J. T.; Penfold, J.; Thomas, R. K.; Li, P.; Cox, A. R.; Hedges, N.; Webster, J. R. P. Spontaneous Surface Self-Assembly in Protein–Surfactant Mixtures: Interactions between Hydrophobin and Ethoxylated Polysorbate Surfactants. *J. Phys. Chem. B* **2014**, *118* (18), 4867–4875.

(34)     Yan, X.; Wang, T.; Yao, D.; Xu, J.; Luo, Q.; Liu, J. Interfacial Assembly of Signal Amplified Multienzymes and Biorecognized Antibody into Proteinosome for an Ultrasensitive Immunoassay. *Small* **2019**, *15* (15), 1900350.

(35)     Svasti, J.; Panijpan, B. SDS-Polyacrylamide Gel Electrophoresis. A Simple Explanation of Why It Works. *J. Chem. Educ.* **1977**, *54* (9), 560. https://doi.org/10.1021/ed054p560.

(36)    Shah, S. K.; Chatterjee, S. K.; Bhattarai, A. Micellization of Cationic Surfactants in Alcohol — Water Mixed Solvent Media. *J. Mol. Liq.* **2016**, *222*, 906–914.

(37)    Sharma, R.; Shaheen, A.; Mahajan, R. K. Cyclic Voltammetry and Viscosity Measurements of Aggregated Assemblies of Anionic Surfactants with Nonionic Surfactants and Triblock Copolymers. *Colloid Polym Sci* **2011**, *289* (1), 43–51.

141

CHAPTER 6

FUTURE PERSPECTIVES

In this dissertation, we demonstrate that protein(s) co-assembly can be a viable approach to manipulate and improve the multistep and multienzyme based catalysis via different mechanisms. More study to further understand the co-assembly process and its effects on enzyme catalysis will be beneficial to expand such strategy in enzyme engineering. In this chapter, we provide some perspectives on future works.

In Chapter 1, we report that the products with different oxidation state can be enriched depending on the side groups of the substrates in CmlI catalyzed reactions, which makes this enzyme and polymer-enzyme NPs very useful in synthetic applications. Further investigations on a broad range of substrates of CmlI will be worth to try. In addition, co-localization of CmlI with some non-natural protein redox partners via the polymer protein co-assembly will be an interesting direction to expand the polymer-multienzyme assembly's applications in CmlI catalysis.

For Chapter 2, the varied kinetics of GOx with different sugars provide useful tools to control $H_2O_2$ releasing process, which can be used to leverage the downstream $OleT_{SA}$ or other peroxygenases/peroxidase catalysis. $OleT_{SA}$ displays a relative broad $H_2O_2$-responsive window and varied kinetics on different acids making it a unique model for GOx coupled tandem catalysis study. More detailed kinetics studies of both enzymes will provide useful information to understand the process and further optimize the enzyme

cascade catalysis. This information can also be used for simulation study to illustrate the proposed 'channel-like' effect on the polymer-multienzyme complexes.

Also in this part of work, we clearly demonstrate that, with GOx coupling, heme bleaching of OleT$_{SA}$ can be mostly avoided during the catalysis. It will be promising to explore different recycling systems to maximize the reusability of these enzymes. Immobilization enzymes on inorganic nanoparticles or flow reactors can be used for such applications. In these processes, the substrate/O$_2$ consumption, product inhibition and pH changing problems limiting the enzyme activity can be addressed. Importantly, the polymer-GOx/OleTSA NPs generated by co-assembly can be readily adapted in the flow reaction systems, providing excellent platform for biofuel production applications.

Notably glucose is much cheaper than mannose and more accessible (e.g. from different bio-processes) in the practical synthesis, so it is worth to optimize the reaction conditions with glucose as the substrate (for example, by adjusting the ratio of GOx and OleT to co-assembly with different polymers).

In Chapter 3, the pyridine-containing polymer protein co-assembly used here represents a unique multistep/multicomponent-involved assembly system. We demonstrated that the fast mixing imparted effects on the co-assembly process and increased the homogeneity of the resultant NPs, which is consistent with our hypothesis that the adsorption of proteins on polymer colloids (i.e. aggregation step) is the rate-limiting step. More detailed descriptions about the process (e.g. aggregation timescale) are needed to further understand the co-assembly process. With this EK-based microfluidic system, the mixing process can be adjusted by electric field and flow rates. High-resolution

imaging system can be easily integrated. So it provides an excellent platform to further study and improve the polymer-protein(s) co-assembly process.

In Chapter 4, we reported a novel phenomenon that small molecules could strikingly enhance $OleT_{SA}$ catalysis with changed kinetics. Structure data will be helpful to understand the origins of the enhancement. In addition, we found that the small molecules showed very different effects on different substrates including fatty acids and non-natural substrates. We observed less enhanced effect in the reactions with high turnover rate further supporting the $H_2O_2$ oxidative stress related mechanism. We speculate that some non-natural substrates (e.g. 3-(4-methoxyyphennyl) propionic acid) themselves can serve as OleT activators based on their unparalleled turnover rates and the structure similarity to the small molecules we reported. Further study to illustrate these observations will be helpful to understand the enhanced effects.

In Chapter 5, the preliminary data showed a promising GOx/OleT based biphasic catalytic system. Some important parameters and processes need to be characterized for further optimization in the future include:

(1) The loading efficiency of OleT and GOx on the microemulsions. The different surface charge distribution of the two enzymes makes the interactions between enzymes and surfactants varied, which will cause different enzyme loading efficiency of the microemulsions.

(2) The activity of OleT on the interface of microemulsions. As analyzed in Chapter 5, we speculate that OleT enzyme activity can be greatly increased after the interfacial

assembly than that in aqueous solution. More direct evidence is needed to identify this possibility.

(3) The activity of GOx on the microemulsions. We assume that GOx enzyme activity is not affected in the working concentration of surfactants used in this work, which need to be confirmed.

(4) The interfacial assembly process. Different surfactants showed different effects on the microemulsions' formation, stability and enzymatic activity suggesting complex interfacial assembly behaviors in the system. More in-depth investigations are needed to understand the assembly process.

(5) Other microstructures formed in the multiphase system. While emulsions were observed in the enzyme/surfactants/hexane system, more study is needed to identify if any other micro- or nanostructures (e.g. micelles) were generated and contributed to the enzymatic activity.

(6) Surfactant structures. Based on the further study, some rational designed surfactants can be developed to generate microemulsions with having desired property (e.g. reversibility, recyclability).

# APPENDIX A

## PERMISSION TO REPRINT FOR CHAPTER 1 AND 3

## Microfluidic-assisted polymer-protein assembly to fabricate homogeneous functionalnanoparticles

**Author:**
Libo Zhang,Andrew Beatty,Lin Lu,Akrm Abdalrahman,Thomas M. Makris,Guiren Wang,Qian Wang

**Publication:** Materials Science and Engineering: C

**Publisher:** Elsevier

**Date:** June 2020

BACK                                                CLOSE WINDOW